

# The 1st JUACEP Workshop at UCLA & University of Michigan

~March 7th - 17th, 2012~



Japan-US Advanced Collaborative Education Program

Nagoya University

Copyright © JUACEP 2012 All Rights Reserved.

Published in November, 2012

Leaders of JUACEP

Prof. Noritsugu Umehara

Prof. Yang Ju

Japan-US Advanced Collaborative Education Program

Graduate School of Engineering

Nagoya University 

Furo-cho, Chikusa-ku, Nagoya, 464-8603, JAPAN

[juacep@engg.nagoya-u.ac.jp](mailto:juacep@engg.nagoya-u.ac.jp)

<http://www.juacep.engg.nagoya-u.ac.jp/>

<http://www.juacep.engg.nagoya-u.ac.jp/en/>

## Table of Contents

<1> Participants	...2
<2> Leaflets	...4
<3> Summaries and Posters	...9
<4> Appendix	
a) Travel Schedule	...87
b) Pictures	...88

## <1> Participants from Nagoya University

### • Students

Name		Advisor
<b>ASABA Masakazu</b>	M1	Prof. E. Shamoto, Dept. Mechanical Science and Engineering
<b>AZUCHI Kosuke</b>	M1	Prof. Y. Ju, Dept. Mechanical Science and Engineering
<b>BAI Mingrui</b>	M1	Prof. H. Yamashita, Dept. Mechanical Science and Engineering
<b>BANNO Miyako</b>	B4	Prof. Obinata, Dept. Mechanical Science and Engineering
<b>EMMEI Risa</b>	M1	Prof. E. Shamoto, Dept. Mechanical Science and Engineering
<b>HIRUTA Kosuke</b>	M1	Prof. Y. Sakai, Dept. Mechanical Science and Engineering
<b>HOSHINO Koichi</b>	M1	Prof. Y. Sakai, Dept. Mechanical Science and Engineering
<b>ISHIGURO Atsushi</b>	M1	Prof. Y. Ju, Dept. Mechanical Science and Engineering
<b>ISHIKAWA Yuta</b>	B4	Prof. N. Umehara, Dept. Mechanical Science and Engineering
<b>ITAKURA Takuya</b>	M1	Prof. E. Tanaka, Dept. Mechanical Science and Engineering
<b>ITO Keitaro</b>	B4	Prof. F. Arai, Dept. Micro-Nano Systems Engineering
<b>ITO Soichiro</b>	M1	Prof. Y. Yamada, Dept. Mechanical Science and Engineering
<b>KAWACHI Masaki</b>	M2	Prof. N. Ohno, Dept. Mechanical Science and Engineering
<b>KISHI Tomoya</b>	M1	Prof. Y. Ju, Dept. Mechanical Science and Engineering
<b>KITAZUME Kazutaka</b>	B4	Prof. N. Umehara, Dept. Mechanical Science and Engineering
<b>KOJIMA Naoki</b>	B4	Prof. Y. Ju, Dept. Mechanical Science and Engineering
<b>LEE Jaeryoung</b>	M2	Prof. Obinata, Dept. Mechanical Science and Engineering
<b>MAEDA Yu</b>	M1	Prof. T. Fukuda, Dept. Mechanical Science and Engineering
<b>MAKINO Takanori</b>	M1	Prof. Y. Ju, Dept. Mechanical Science and Engineering
<b>NAGANO Hikaru</b>	M2	Prof. Y. Yamada, Dept. Mechanical Science and Engineering
<b>NAKANISHI Naoya</b>	B4	Prof. N. Umehara, Dept. Mechanical Science and Engineering
<b>NAKASHIMA Takahiro</b>	B4	Prof. Y. Ju, Dept. Mechanical Science and Engineering
<b>NISHIMURA Hidenori</b>	B4	Prof. N. Umehara, Dept. Mechanical Science and Engineering
<b>OHARA Kenji</b>	M1	Prof. N. Umehara, Dept. Mechanical Science and Engineering
<b>SANO Ryohei</b>	B4	Prof. Obinata, Dept. Mechanical Science and Engineering
<b>SUMIGAMA Miho</b>	B4	Prof. N. Umehara, Dept. Mechanical Science and Engineering
<b>SUNADA Koji</b>	M1	Prof. Y. Yamada, Dept. Mechanical Science and Engineering
<b>SUZUKI Satoshi</b>	M1	Prof. Y. Ju, Dept. Mechanical Science and Engineering
<b>TANASE Toshikatsu</b>	B4	Prof. Obinata, Dept. Mechanical Science and Engineering
<b>TESHIMA Hiromasa</b>	M1	Prof. Y. Ju, Dept. Mechanical Science and Engineering
<b>UCHIYAMA Yoshiho</b>	B4	Prof. Obinata, Dept. Mechanical Science and Engineering

<b>WATANABE Tomoaki</b>	M1	Prof. Y. Sakai, Dept. Mechanical Science and Engineering
<b>YAGI Yuji</b>	B4	Prof. N. Umehara, Dept. Mechanical Science and Engineering
<b>YAMAGUCHI Akichika</b>	M1	Prof. T. Niimi, Dept. Micro-Nano Systems Engineering
<b>YAMAGUCHI Yuhei</b>	B4	Prof. Y. Ju, Dept. Mechanical Science and Engineering
<b>YAMAZAKI Yudai</b>	M1	Prof. K. Sato, Dept. Micro-Nano Systems Engineering
<b>YOSHIDA Takahiro</b>	M1	Prof. Y. Ju, Dept. Mechanical Science and Engineering

• Faculty

--- Workshop in UCLA on March 8 ---

**Prof. OBINATA Goro**

**Prof. JU Yang**

**Assoc. Prof. SUZUKI Norikazu**

**Assoc. Prof. MORITA Yasuyuki**

**Assist. Prof. TOKOROYAMA Takayuki**

**Lecturer ITO Yasumasa**

**Assist. Prof. TOKUDA Satoru**

**Lecturer OOE Katsutoshi**

--- Workshop in Univ. Michigan on March 12 ---

**Prof. UMEHARA Noritsugu**

**Prof. JU Yang**

**Assoc. Prof. KOUSAKA Hiroyuki**

**Lecturer ITO Yasumasa**

**Assist. Prof. TOKUDA Satoru**

• Research Associates of Micro-Nano Global COE – for Workshop in UCLA on March 8

<b>DI Pei</b>	D1	Dept. Micro-Nano Systems Engineering
<b>INOUE Hiroshi</b>	D1	Dept. Mechanical Science and Engineering
<b>JUNG Jaehoon</b>	D1	Dept. Micro-Nano Systems Engineering
<b>KAMADA Shoichiro</b>	D2	Dept. Mechanical Science and Engineering
<b>KAMEYA Tomohiro</b>	D2	Dept. Micro-Nano Systems Engineering
<b>KOJIMA Masahiro</b>	D2	Dept. Micro-Nano Systems Engineering
<b>SHEN Yajing</b>	D3	Dept. Micro-Nano Systems Engineering
<b>XIANG Jingyu</b>	D2	Dept. Mechanical Science and Engineering
<b>YANG Zhan</b>	D2	Dept. Micro-Nano Systems Engineering

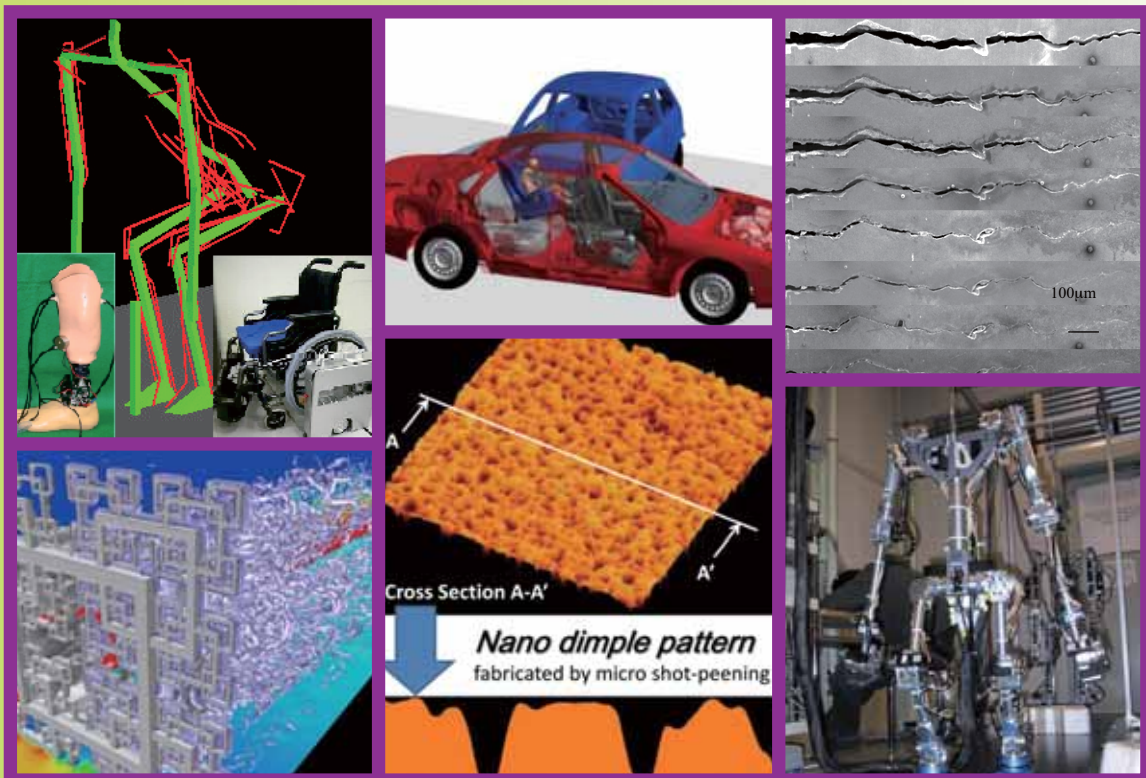
# The 1<sup>st</sup> Nagoya University - UCLA JUACEP Student Workshop on Mechanical Engineering and Science

March 8 - 9, 2012, at UCLA, Los Angeles, CA

## Program

March 8 11:00 – 15:00 Poster presentation  
(De Neve Plaza (Rooms A & B))

March 9 13:00 – 16:00 Lab tours



Organizers: Profs. N. Umehara, Y. Ju (Nagoya U)  
Profs. C. M. Ho, T. C. Tsao (UCLA)



Japan-US Advanced Collaborative Education Program (JUACEP)  
Graduate School of Engineering, Nagoya University  
Furo-cho, Chikusa-ku, Nagoya, 464-8603, JAPAN  
Phone: +81-52-789-3113 Fax: +81-52-789-3111  
Email: yito@mech.nagoya-u.ac.jp, tokuda@esi.nagoya-u.ac.jp



No.	Poster title	Presenter
1	Wear particle analysis of DLC thin films focusing on structural changes and characteristics under oil lubrication	Kenji Ohara
2	Fudamental research for the development of cooling radio knife tip to prevent blood coagulation on the tip	Yuta Ishikawa
3	The improvement of the properties of Si-CN <sub>x</sub> Hy coating with Plasma CVD	Kazutaka Kitazume
4	Fundamental research for high friction and small wear brake pad	Miho Sumigama
5	The effect of inner blade speed for cutting sharpness of electric shaver	Naoya Nakanishi
6	The clarification of the relationship between transfer layer and friction coefficient of carbonaceous coating	Hidenori Nishimura
7	The development of droplet free CN <sub>x</sub> coating with Ion Beam Assited Deposition	Yuji Yagi
8	Numerical Study on Combustion Characteristics of Ultra-micro Combustor with Porous Chamber Wall	Bai Mingrui
9	Application of molecular tagging velocimetry to rarefied gas flow	Akichika Yamaguchi
10	A study on Human Avoidance Motion for Human-Robot coexistence system	Koji Sunada
11	Basic Eye Part Collision Experiments against Sharp Mechanical Hazards for Severity Investigation	Soichiro Ito
12	What appeals to human touch? Comprehensive Study of Textures that Give an Incentive for Haptic Exploration	Hikaru Nagano
13	Noncontact nanometric positioning of probe tip for measurement of mechanical parameters of cell	Keitaro Ito
14	Occupant response in vehicle frontal crash	Takuya Itakura
15	Mechanical properties of carbon nanotubes with one-dimensional intramolecular junction	Masaki Kawachi
16	Road detection system outdoors –Image recognition with improved Flood Fill–	Yu Maeda
17	Parylene based catheter type flow sensor for detecting breathing characteristics	Yudai Yamazaki
18	EHL Analysis of CMP Process by Using ALE Finite Element Method	Masakazu Asaba
19	Study on Tool Damage in High-speed Ceramic Milling of Superalloys	Risa Emmei
20	On statistical properties of a turbulent boundary layer affected by the cylinder wake in a freestream	Kosuke Hiruta
21	Measurements of High-Schmidt-Number Scalar Mixing Layers in Grid Turbulence by means of PIV and PLIF	Koichi Hoshino
22	Turbulent Mixing in a Planar Liquid Jet with a Second-Order Chemical Reaction	Tomoaki Watanabe
23	Improvement of light detection of photodiode with local surface plasmon resonance	Atsushi Ishiguro
24	Effect of cyclic mechanical stretching on stem cell-to-tenocyte differentiation: Assessment by extracellular matrix expression levels and structure	Satoshi Suzuki
25	Fabrication of high density Au nanowires by template method	Hiromasa Teshima
26	Measurement of electrical properties of cell surface by Microwave Atomic Force Microscopy	Takanori Makino
27	Nondestructive measurement and high-precision evaluation of the electrical conductivity of doped GaAs wafers using microwaves	Takahiro Yoshida
28	Evaluation of mechanical property of thin films using ultrasonic waves induced by femtosecond pulse laser	Kosuke Azuchi
29	Development of fatigue crack-healing technique for metals	Tomoya Kishi
30	Study of copper oxide nanowires generated by stressmigration at the selectivity metal deposits	Naoki Kojima
31	Development of evaluation technique for electric property using Microwave AFM	Takahiro Nakashima
32	Study on detection of delamination in unidirectional CFRP by microwave reflectometry	Yuhei Yamaguchi
33	What Is the Adequate Feature of a Robot for Children with Autism in Robot-Assisted Therapy?	Jaeryoung Lee
34	Sensory Perception by Electrical Stimulation	Miyako Banno
35	Simulation of Human Walking with Orthosis for Keeping Balance Upper Body	Yoshiho Uchiyama
36	Study of Operability Movement Steering System Using Lever Steering	Ryohei Sano
37	Analysis on Hand Motions in Activity of Daily Living	Toshikatsu Tanase

## Poster presentations by GCOE Program

No.	Poster title	Presenter
38	A Method to Study the Single Cell's Adhesion Strength via Nano Manipulation inside ESEM	Yajing Shen
39	Platinum Nanowire Growth via Field Emission Controlled by Nanorobtic Manipulator	Zhan Yang
40	A Fall Prevention Scheme for Intelligent Cane Robot by Using a Motor Driven Universal Joint	Pei Di
41	Measurement of Body Volume of Live C. elegans by Microchip	Jaehoon Jung
42	The effect of Mesh Design for Developing Flow Controllable Stent: Computational Fluid Dynamics Study	Masahiro Kojima
43	Variable-resolution Roadmaps Considering Safety of Robots	Jingyu Xiang
44	Pressure-Sensitive Paint measurement on a rotating disk	Tomohiro Kameya
45	Task Based Design Method for Multi-joint Prosthetic Hands Using Motion Analysis	Shoichiro Kamada
46	TEM Observation of Super low friction's extram surface of carbon nitride hardcoating	Hiroshi Inoue

# The 1<sup>st</sup> Nagoya U – U Michigan JUACEP Student Workshop on Mechanical Engineering and Science

March 12-13, 2012, at Univ. Michigan, Ann Arbor, MI

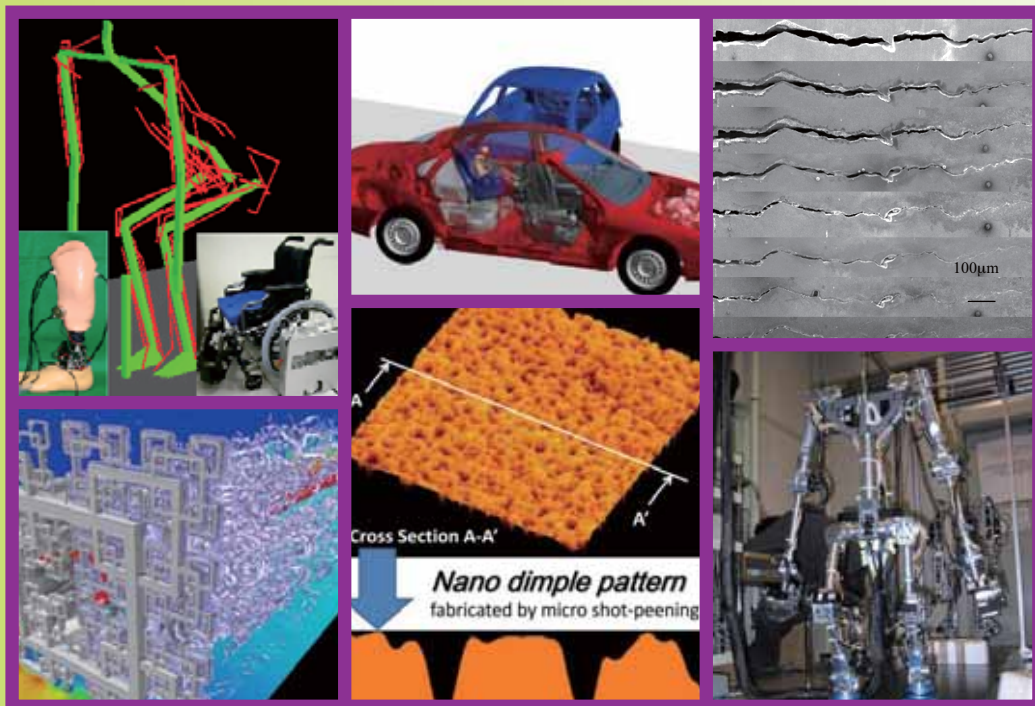
## Program

### Monday, March 12, 2012

9:00am-9:30am	Welcome reception (Chrysler Lobby)
9:30am-11:30am	Lab tours
1:00pm-3:00pm	Lab tours
3:00pm-5:30pm	Poster session (Tishman Hall, CSE Building)
6:00pm	Banquet

### Tuesday, March 13, 2012

9:00am-11:00am	Toyota Tech Center visit
1:30am- 5:00pm	Lab tours, Tour of North Campus



Organizers: Profs. N. Umehara, Y. Ju (Nagoya U)  
Prof. V. Sick (U Michigan)



Japan-US Advanced Collaborative Education Program (JUACEP)  
Graduate School of Engineering, Nagoya University  
Furo-cho, Chikusa-ku, Nagoya, 464-8603, JAPAN  
Phone: +81-52-789-3113 Fax: +81-52-789-3111  
Email: yito@mech.nagoya-u.ac.jp, tokuda@esi.nagoya-u.ac.jp



No.	Poster title	Presenter
1	Wear particle analysis of DLC thin films focusing on structural changes and characteristics under oil lubrication	Kenji Ohara
2	Fudamental research for the development of cooling radio knife tip to prevent blood coagulation on the tip	Yuta Ishikawa
3	The improvement of the properties of Si-CN <sub>x</sub> Hy coating with Plasma CVD	Kazutaka Kitazume
4	Fundamental research for high friction and small wear brake pad	Miho Sumigama
5	The effect of inner blade speed for cutting sharpness of electric shaver	Naoya Naknishi
6	The clarification of the relationship between transfer layer and friction coefficient of carbonaceous coating	Hidenori Nishimura
7	The development of droplet free CN <sub>x</sub> coating with Ion Beam Assited Deposition	Yuji Yagi
8	Numerical Study on Combustion Characteristics of Ultra-micro Combustor with Porous Chamber Wall	Bai Mingrui
9	Application of molecular tagging velocimetry to rarefied gas flow	Yamaguchi Akichika
10	A study on Human Avoidance Motion for Human-Robot coexistence system	Sunada Koji
11	Basic Eye Part Collision Experiments against Sharp Mechanical Hazards for Severity Investigation	Ito Soichiro
12	What appeals to human touch? Comprehensive Study of Textures that Give an Incentive for Haptic Exploration	Nagano Hikaru
13	Noncontact nanometric positioning of probe tip for measurement of mechanical parameters of cell	Ito Keitaro
14	Occupant response in vehicle frontal crash	Itakura Takuya
15	Mechanical properties of carbon nanotubes with one-dimensional intramolecular junction	Kawachi Masaki
16	Road detection system outdoors –Image recognition with improved Flood Fill–	Maeda Yu
17	Parylene based catheter type flow sensor for detecting breathing characteristics	Yamazaki Yudai
18	EHL Analysis of CMP Process by Using ALE Finite Element Method	Asaba Masakazu
19	Study on Tool Damage in High-speed Ceramic Milling of Superalloys	Emmei Risa
20	On statistical properties of a turbulent boundary layer affected by the cylinder wake in a freestream	Hiruta Kosuke
21	Measurements of High-Schmidt-Number Scalar Mixing Layers in Grid Turbulence by means of PIV and PLIF	Hoshino Koichi
22	Turbulent Mixing in a Planar Liquid Jet with a Second-Order Chemical Reaction	Watanabe Tomoaki
23	Improvement of light detection of photodiode with local surface plasmon resonance	Ishiguro Atsushi
24	Effect of cyclic mechanical stretching on stem cell-to-tenocyte differentiation: Assessment by extracellular matrix expression levels and structure	Suzuki Satoshi
25	Fabrication of high density Au nanowires by template method	Ieshima Hiromasa
26	Measurement of electrical properties of cell surface by Microwave Atomic Force Microscopy	Makino Takanori
27	Nondestructive measurement and high-precision evaluation of the electrical conductivity of doped GaAs wafers using microwaves	Yoshida Takahiro
28	Evaluation of mechanical property of thin films using ultrasonic waves induced by femtosecond pulse laser	Azuchi Kosuke
29	Development of fatigue crack-healing technique for metals	Kishi Tomoya
30	Study of copper oxide nanowires generated by stressmigration at the selectivity metal deposits	Kojima Naoki
31	Development of evaluation technique for electric property using Microwave AFM	Nakashima Takahiro
32	Study on detection of delamination in unidirectional CFRP by microwave reflectometry	Yamaguchi Yuhei
33	What Is the Adequate Feature of a Robot for Children with Autism in Robot-Assisted Therapy?	Jaeryoung Lee
34	Sensory Perception by Electrical Stimulation	Miyako Banno
35	Simulation of Human Walking with Orthosis for Keeping Balance Upper Body	Yoshiho Uchiyama
36	Study of Operability Movement Steering System Using Lever Steering	Ryohei Sano
37	Analysis on Hand Motions in Activity of Daily Living	Toshikatsu Tanase



INTERNATIONAL PROGRAMS  
IN ENGINEERING

Nagoya University Visit  
March 12-14, 2012

---

Guests:	Professor Ju, Professor Umehara, Prof. Obinata, Associate Professor Kousaka, Dr. Ito, Dr. Tokuda, Dr. Ooe Nagoya University
Host:	Professor Volker Sick Faculty Advisor, International Programs in Engineering (734) 647-7129

**Monday, March 12, 2012**

9:00am-9:30am	Welcome Reception Chrysler Lobby
9:30am-11:30am	Lab tours – including <i>Wilson Student Tam Project Center</i>
11:30am-1:00pm	Lunch – purchase own lunch and dine in the (reserved) Boulevard Room in Pierpont Commons
1:00pm-3:00pm	Lab tours
3:00pm-5:30pm	Poster Session Tishman Hall, Computer Science & Engineering Building (CSE)
6:00pm	Banquet – Holiday Inn Ann Arbor

**Tuesday, March 13, 2012**

9:00am – 11:30am	Lab Tours
11:30am-12:30pm	Break for lunch
1:00pm-2:00pm	Tour of North Campus David Betts: 647-7132
3:00pm-5:00pm	<i>Tentative:</i> Toyota Tech Center Visit 1555 Woodridge Avenue, Ann Arbor, MI Map: <a href="http://www.manta.com/cmap/mm432pg/toyota-technical-center">http://www.manta.com/cmap/mm432pg/toyota-technical-center</a>

**Wednesday, March 14, 2012**

Free time while in the Detroit/Ann Arbor area:

Henry Ford Museum: <http://www.thehenryford.org/museum/index.aspx>  
 Briarwood Mall (shopping): <http://www.simon.com/mall/MallDirectory.aspx?id=1231>  
 UM Museum of Art: <http://www.umma.umich.edu/>  
 UM Museum of Natural History: <http://www.lsa.umich.edu/ummnh/>

**<3> Summaries and Posters**  
(in order of presentations)

# Analysis of DLC wear particles on oil lubrication



Kenji Ohara

ohara@ume.mech.nagoya-u.ac.jp

Noritsugu Umehara

ume@mech.nagoya-u.ac.jp

Takayuki Tokoroyama

tokoyama@ume.mech.nagoya-u.ac.jp

Nagoya University, Department of Mechanical Science and Engineering  
Furo-cho, Chikusa-ku, Nagoya, 464-8603 Japan

## Abstract

In this study, the diagnosis of the wear on the DLC (diamond-like carbon) film was enabled by analyzing  $I_D/I_G$  ratio of DLC wear particles. DLC film is expected as low friction and high wear resistance material. And, it is reported that the crystallographic structure on the surface is changed by the tribo-chemical reaction when the friction occurs. Then, authors established the technique for catching the structural change of the wear particles on the friction surface. This technique enabled the method of machine maintenance as well as ‘Oil analysis’.

In this report, authors firstly characterized shape and color of DLC wear particles by scanning electron microscopy and optical microscope. (Fig.1)

Secondly, they evaluated average thickness of DLC wear particles by specific wear rate and area of wear particles on membrane filter (2).

As a result, increasing average thickness of DLC wear particles caused structural change of DLC wear particle (Fig3).

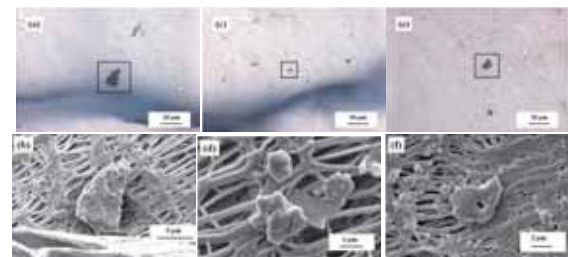


Fig. 1 (a) DLC wear particle obtained at 25 °C frictional test by OM (Optical Microscope), (b) Enlargement image of (a) by SEM, (c) DLC wear particles obtained at 80 °C, (d) Enlargement of (c), (e) DLC wear particles obtained 120 °C and (f) Enlargement of (e)

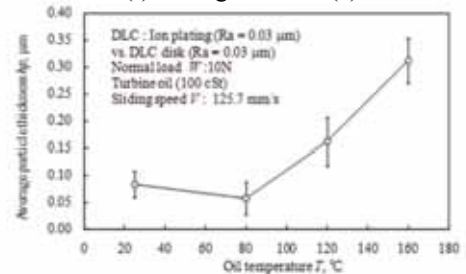


Fig. 2 The relationship between average particle thickness and temperature

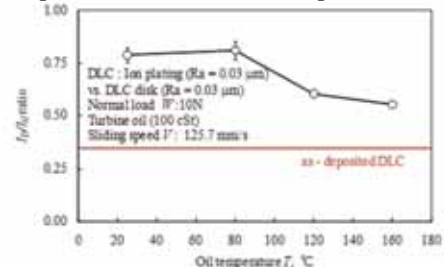


Fig. 3 The relationship between  $I_D/I_G$  ratio and temperature

## Biography

Kenji Ohara received the Bachelor degree in Mechanical engineer from Nagoya University in 2011. He belongs to master's course of Nagoya University, focusing on the studies of DLC for engine bearing.

# Analysis of DLC wear particles on oil lubrication

Kenji Ohara<sup>(1)</sup> Umehara Noritsugu<sup>(1)</sup>  
Takayuki Tokoroyama<sup>(1)</sup>

(1) Nagoya University

## Purpose

Lubricating oil diagnostic technology, such as the ferrography method, is mentioned as the mechanical preservation method. And it is used for wear state prediction. So, in this research, the wear particles which occurred from the DLC film were separated out of lubricating oil, and the parameter which can detect unusual wear of a DLC film was proposed from analysis of DLC wear particles.

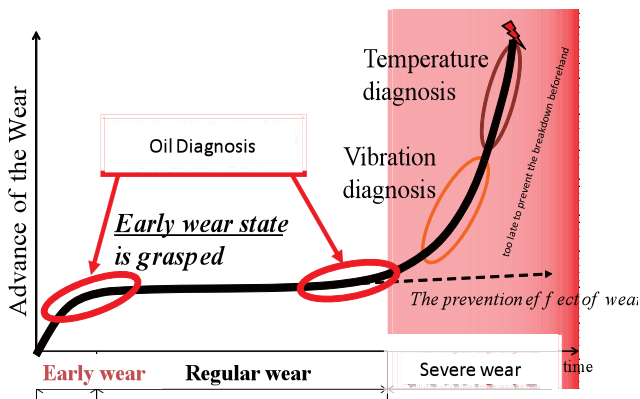
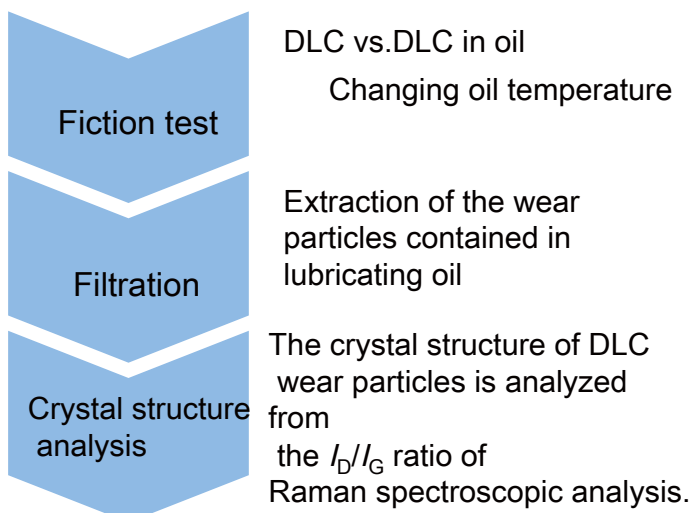


Fig. 1 Model of wear

## Experiment



## Results

Fig.2 DLC wear particles are collected  
Fig.3 Fig.4  $I_D/I_G$  of DLC wear particles decrease with translating sever wear from mild wear

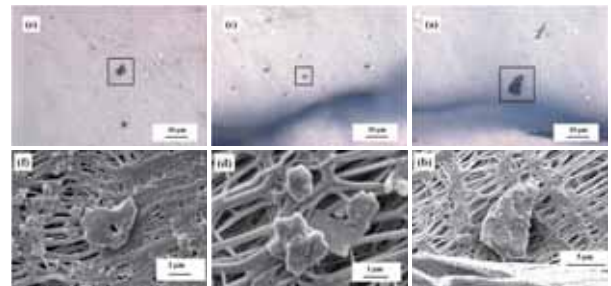


Fig. 2 (a) DLC wear particle obtained at 25 °C frictional test by OM (Optical Microscope), (b) Enlargement image of (a) by SEM, (c) DLC wear particles obtained at 80 °C, (d) Enlargement of (c), (e) DLC wear particles obtained 120 °C and (f) Enlargement of (e)

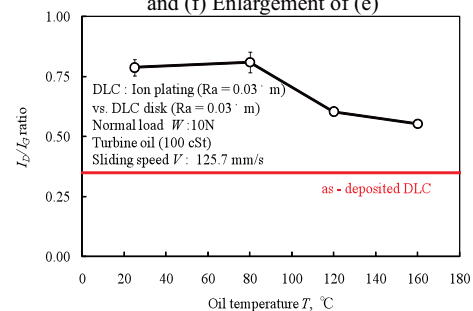


Fig. 3 The relationship between  $I_D/I_G$  ratio and temperature

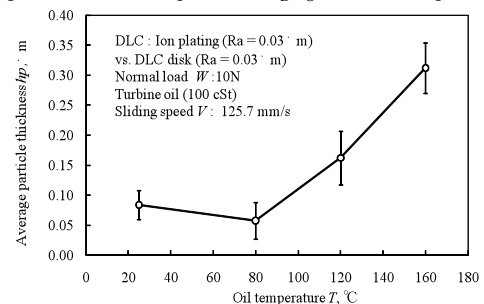


Fig. 4 The relationship between average particle thickness and temperature

## Conclusion

By analyzing DLC wear particles, the phenomenon similar to changes of the wear form of a metal called the changes to the mechanical wear of a bulk layer from wear by the removal of a structural change layer which was not clarified became clear in the analysis only by the side of a DLC film conventionally.

# Basic Research of a Chip Cooling System Required for a Blood Coagulation Adhesion Control Radio Knife



Yuta ISHIKAWA  
ishikawa@ume.mech.nagoya-u.ac.jp  
Noritsugu UMEHARA  
ume@mech.nagoya-u.ac.jp  
Hiroyuki KOUSAKA  
kousaka@mech.nagoya-u.ac.jp  
Takayuki TOKOROYAMA  
tokoroyama@mech.nagoya-u.ac.jp  
School of Engineering, Nagoya University  
Furo-cho, Chikusa-ku, Nagoya 464-8603, JAPAN

## Abstract

There is a problem of the protein in blood carrying out heat denaturation at the tip of a radio knife, solidifying at it, and stopping discharging at it in a surgical operation, and since it is used shaving the blood which carried out solidification adhesion at the tip of a radio knife, a remedy is desired at the operation spot.

It was reported that blood coagulation adhesion can be controlled by cooling a radio knife tip, and it aims at the development and utilization of a radio knife tip which controlled protein solidification adhesion in this research. However, the former cooling system used cooling water circuit system which prevents the operator's action at the surgical scene. That's why, it is necessary to apply other cooling system.

Then, we tried to develop a cooled type radio knife using the Peltier device as the technique of newly cooling knife tip. Figure 1 shows the schematic image of newly radio knife using Peltier device. It makes possible to not use cooling water circuit. The ability of this newly radio knife was assured by coagulation tests.

The Fig. 2 shows the relationship between applying voltage for Peltier device to cool the tip and temperature of the tip surface.

It was clear that if the applying voltage was larger than 0.7 V, the tip surface was not covered by blood coagulation. The minimum temperature was generated by applying voltage at about 2 V. This result indicated that cooling system by Peltier device makes possible to prevent coagulation on it.

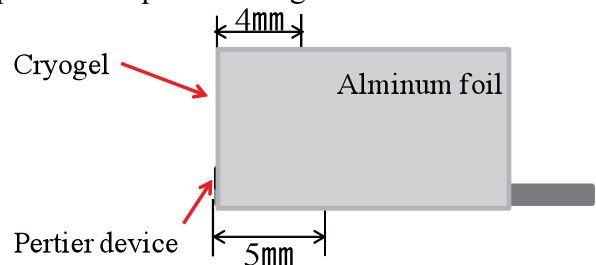


Fig. 1 The schematic image of newly radio knife tip with Peltier device

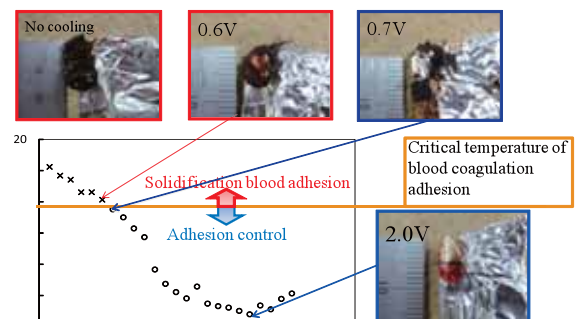


Fig. 2 The relationship between inner blade and average pulling force

## Biography

Yuta Ishikawa entered in Nagoya University in 2008 and will graduate in 2012.

# Basic research of a chip cooling system required for a blood coagulation adhesion control radio knife

Yuta Ishikawa Noritsugu Umehara Takayuki Tokoroyama, Nagoya University March, 2012

## Background

The radio knife is one of a operating tool for surgical scene. It can prevent bleeding when operator cut human body and etc. Generally, this radio knife has coaguration problem which involves no discharge and finally the knife can not cut (see Fig.1). In a previous research, we investigated that coaguration of blood did not take place when the inside of radio knife tip cooled by circulation water. However, the technique of using circulation water has disadvantages such as uncomfortable usage by connecting water circuit and radio knife tip should have water flow port at the inside. Therefore, it is necessary to develop new cooling system without water circuit.

Discharge current concentrate on tiny area  
 Incision and coagulation by Joule heat

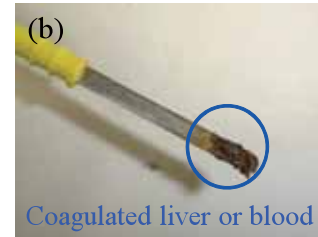
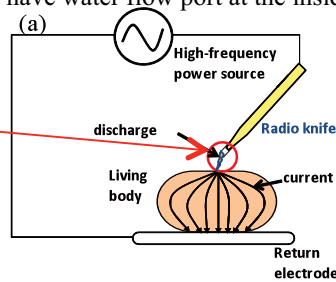


Fig. 1 (a) principal of radio knife operation and (b) coaguration on knife tip

## Purpose

The trial production of the cooled type radio knife which introduced the Peltier device simplified by a cooling system without water-circuit

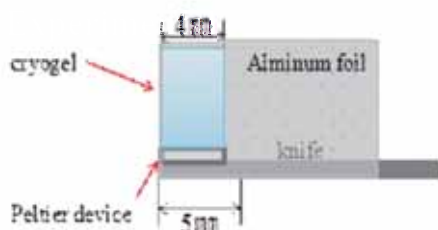


Fig. 2 The mimetic diagram of the cooled type radio knife using a Peltier device

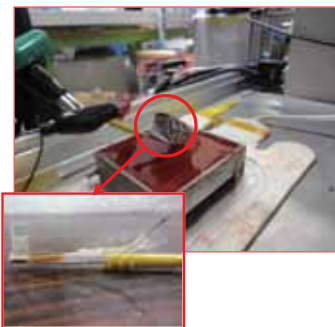


Fig. 3 The cooling side at the tip of a radio knife is inserted into blood

## Experimental condition

- Electric discharge time : 20 s
- Radio knife power supply output : 50 W
- Cooling gel Size : 4 mm×4 mm×3.5 mm  
Temperature: 23 °C
- Peltier device The maximum amount of adsorption: 2.0 W  
Size: 3.8 mm×3.8 mm×1.1 mm
- Cow blood : 30 ml
- After cooling the radio knife for 10 seconds in a Peltier device beforehand, then tip is inserted into blood in 5 mm from the tip.

## Results

The cooling side top at the tip of a knife is lightly traced twice in parallel with a swab

Blood coagulation adhesion on radio knife tip tip 5mm inserted into blood is shown, and the existence of a chilling effect is judged

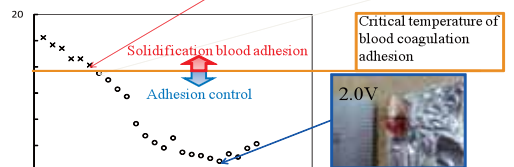
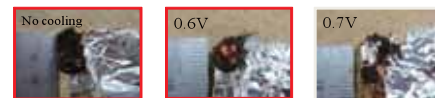
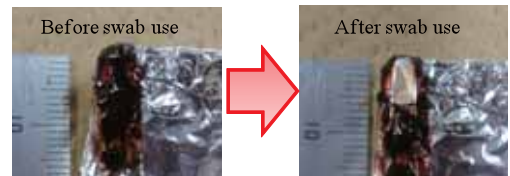


Fig. 4 The difference in the blood coagulation adhesion in different impressed electromotive force

## Discussion

The cooling side of a Peltier device must be kept at 10 °C or less, it was clear that, when the impressed electromotive force to a Peltier device was higher than 0.7V, very low adhesion was generated.

## Conclusion

The radio knife tip with peltier device generated very low adhesion between coaguration blood and tip surface when applied voltage was higher than 0.7V.

# The improvement of the properties of Si-CN<sub>x</sub>H<sub>y</sub> coating with Plasma CVD



Kazutaka KITAZUME

[i.kitadume@ume.mech.nagoya-u.ac.jp](mailto:i.kitadume@ume.mech.nagoya-u.ac.jp)

Hiroyuki KOUSAKA

[kousaka@mech.nagoya-u.ac.jp](mailto:kousaka@mech.nagoya-u.ac.jp)

Noritugu UMEHARA

[ume@mech.nagoya-u.ac.jp](mailto:ume@mech.nagoya-u.ac.jp)

Takayuki TOKOROYAMA

[tokoroyama@mech.nagoya-u.ac.jp](mailto:tokoroyama@mech.nagoya-u.ac.jp)

School of Engineering, Nagoya University  
Furo-cho, Chikusa-ku, Nagoya 464-8603, JAPAN

## Abstract

CN<sub>x</sub> (Carbon nitride) coating is one of the attractive materials that satisfy both relatively high hardness and low friction. It was reported that if CN<sub>x</sub> coating slid against Si<sub>3</sub>N<sub>4</sub> ball, friction coefficient reduces down to lower than 0.01[1].

Carbonaceous coatings including CN<sub>x</sub> coating can be synthesized by PECVD (Plasma Enhanced Chemical Vapor Deposition) method. PECVD is more suitable for 3 dimensional substrate rather than PVD (Physical Vapor Deposition) method because this coating method use precursor gas and generating plasma makes possible to coat for 3 dimensions. In this research, we synthesize Si-CN<sub>x</sub>H<sub>y</sub> coating by using a PECVD apparatus as shown in Fig.1 with

Ar, CH<sub>4</sub>, N<sub>2</sub> and TMS (Tetramethylsilane) employed as precursor gases. In this chamber, high density plasma is generated along the quartz tube by 2.45 GHz microwaves injected through the bottom of the chamber[2].

Si-CN<sub>x</sub>H<sub>y</sub> coatings were deposited on stainless-steel (SUS304, JIS) substrates for 20 min at a gas pressure of 40 Pa, the microwave peak power was 900 W, and gas flow rates of 10, 2, 15, 0.6 sccm in Ar, TMS, CH<sub>4</sub>, N<sub>2</sub> respectively. The microwave was applied pulsed manner where the duty ratio was controlled in 40 %. The different 4 Si-CN<sub>x</sub>H<sub>y</sub> were synthesized at substrate bias voltages of -300 V, -400 V, -500 V, and -600 V. The temperature of substrate at deposit was 270 °C.

The relationship between bias voltage applied to substrate and nano indentation hardness is shown in Fig. 2. The hardness of Si-CN<sub>x</sub>H<sub>y</sub> coating was around 20 GPa when the bias voltage was higher than -300 V. Suggesting that ion enhanced ion bombardment by increasing bias voltage caused higher hardness of Si-CN<sub>x</sub>H<sub>y</sub>.

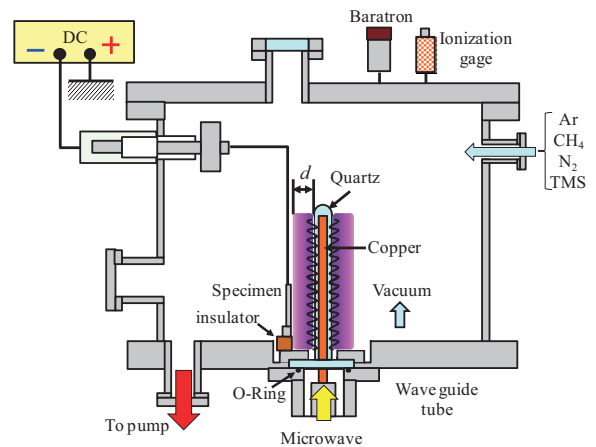


Fig.1 Schematic of PECVD apparatus

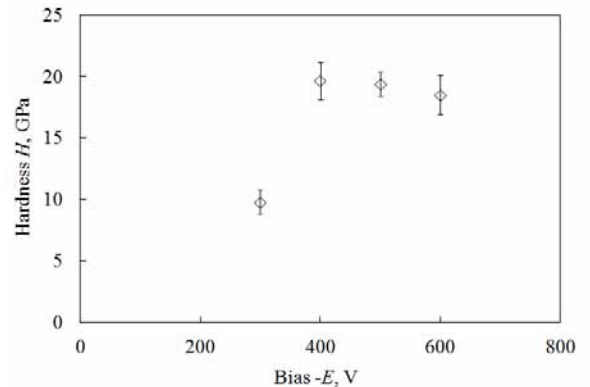


Fig.2 The relationship between bias voltage and nano indentation hardness of Si-CN<sub>x</sub>H<sub>y</sub> coating

## References

- [1] Umehara, N., Kato, K., Sato, T., Proceedings of the International Conference on Metallurgical Coatings and Thin Films, (1998), p.151.
- [2] H. Kousaka, S. Kishine, N. Umehara, IEEE Conf. Proc. Micro-NanoMechatronics and Human Science,(2007),490-493

## Biography

Kazutaka Kitazume entered school of Engineering, Nagoya University in 2008, and will graduate in 2012

# The improvement of the properties of Si-CN<sub>x</sub>H<sub>y</sub> coating with Plasma CVD

K.Kitazume, H.Kousaka, N.Umehara, T.Tokoroyama

Nagoya University March 2012

## PURPOSE

Carbon nitride (CN<sub>x</sub>) coating is an attractive material that satisfy both relatively high hardness and ultra-low friction coefficient against Si<sub>3</sub>N<sub>4</sub> ball in dry nitrogen (<0.01)[1]. In this work, investigating the effect of substrate bias increase on the hardness and friction property of Si-CN<sub>x</sub>H<sub>y</sub> coating (Fig.1) by plasma -enhanced chemical vapor deposition (PECVD).

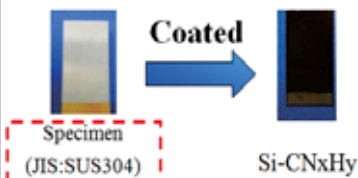


Fig.1 Substrate and coated Si-CN<sub>x</sub>H<sub>y</sub> film

## EXPERIMENT

The schematic view of PECVD apparatus is shown in Fig. 2 Film deposition conditions are shown in Table 1.

In order to clarify the friction characteristic in the oil of a Si-CN<sub>x</sub>H<sub>y</sub> coating, the friction test was done against bearing-steel balls (SUJ2, JIS) in poly- $\alpha$ -olefin (PAO). The schematic view of the friction tester used by this research is shown in Fig. 3 The weight of 102.2 g was used for vertical, and it examined by applying 1.0 N load. In friction, the substrate side rotates at the rate of 200 rpm (sliding speed 42 mm/s).

Table.1 Experimental conditions for depositions

Total pressure (Pa)		40
Substrate distance <i>d</i> (mm)		23
Substrate temperature(° C)		250-300
DC bias voltage (V)		300 - 600
(Pulse 10 kHz)		
Ar-cleaning time (min)		15
Coating time (min)		20
Gas flow ration (sccm)	CH <sub>4</sub>	15
	N <sub>2</sub>	0.6
	Ar	10
	TMS[Si(CH <sub>3</sub> ) <sub>4</sub> ]	2
Microwave power (W)	Average power	300
(Pulse 500 Hz)	Max power	900

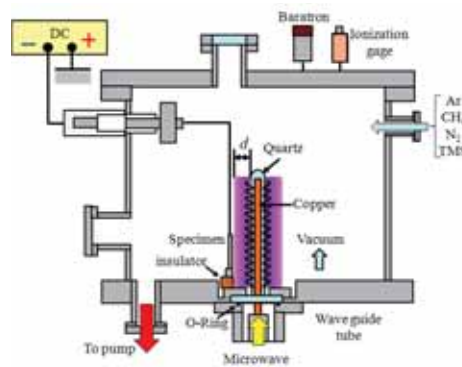


Fig.2 Schematic of PECVD apparatus[2]

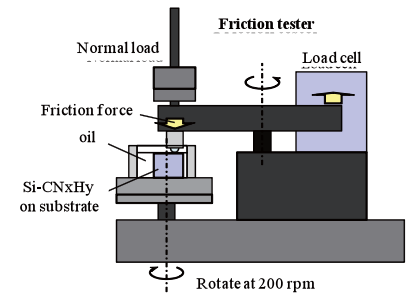


Fig.3 Schematic of pin-on-disk type friction tester

## RESULTS

A result of Si-CN<sub>x</sub>H<sub>y</sub> film indentation hardness when substrate bias increase at deposition is shown Fig.4. Si-CN<sub>x</sub>H<sub>y</sub> hardness was set to 19GPa by raising bias to -400V, and even if raised after it, there was no rise of film hardness. Fig.5, Fig.6 show the friction coefficient of the hard Si-CN<sub>x</sub>H<sub>y</sub> (bias -600V) and softer Si-CN<sub>x</sub>H<sub>y</sub> (bias -300V).

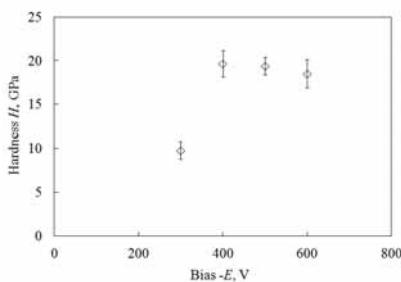


Fig.4 The relationship between bias voltage and nano indentation hardness of Si-CN<sub>x</sub>H<sub>y</sub> coating

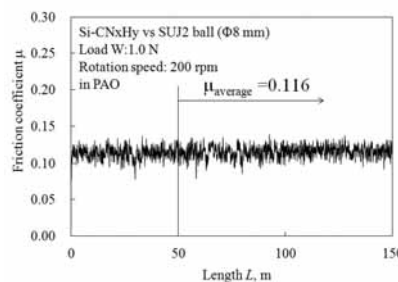


Fig.5 Friction coefficient between Si-CN<sub>x</sub>H<sub>y</sub> deposited at -300V and SUJ2

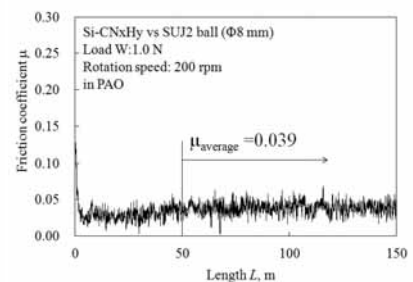


Fig.6 Friction coefficient between Si-CN<sub>x</sub>H<sub>y</sub> deposited at -600V and SUJ2

## DISCUSSION

The result of Raman spectroscopic analysis is shown Fig.7. It is said that more inclination sudden, the more hydrogen contents[3]. That is, Si-CN<sub>x</sub>H<sub>y</sub> hardness rises because the hydrogen content was less, and it is thought that it led to reduction of the coefficient of friction in the oil[4].

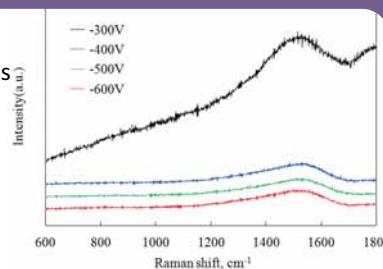


Fig.7 Raman spectra of Si-CN<sub>x</sub>H<sub>y</sub> coating deposition at -300, 400, -500, and -600 V

## CONCLUSION

- The hardness of Si-CN<sub>x</sub>H<sub>y</sub> was increased from 10GPa at a substrate bias voltage of -300V to more than 19GPa at a substrate bias voltage of -600V.
- The friction coefficient between Si-CN<sub>x</sub>H<sub>y</sub> deposited at -600V and SUJ2 in oil lower than substrate bias -300V.

### References

[1] Umehara, N., Kato, K., Sato, T., *Proceedings of the International Conference on Metallurgical Coatings and Thin Films*, (1998), p.151. Human Science, (2007) 490-493

[3] C. Casiraghi, F. Piazza, A.C. Ferrari, D. Grambole, J. Robertson, *Diamond & Related Materials* 14 (2005) 1098–1102

[2] H. Kousaka, S. Kishine, N. Umehara, *IEEE Conf. Proc. Micro-NanoMechatronics and*

[4] Y.Yasuda, M.Kano, T.Mabuchi and S.Abou, *SAE Paper*, 2003-01-1101(2003)

# Development of high friction and low aggression brake pad for next-generation automobile



Miho Sumigama

[sumigama@ume.mech.nagoya-u.ac.jp](mailto:sumigama@ume.mech.nagoya-u.ac.jp)

Noritugu Umehara

[ume@mech.nagoya-u.ac.jp](mailto:ume@mech.nagoya-u.ac.jp)

Hiroyuki Kousaka

[kousaka@mech.nagoya-u.ac.jp](mailto:kousaka@mech.nagoya-u.ac.jp)

Takayuki Tokoroyama

[tokoroyama@mech.nagoya-u.ac.jp](mailto:tokoroyama@mech.nagoya-u.ac.jp)

Faculty of Engineering, Nagoya University  
Furo-cho, Chikusa-ku, Nagoya, 464-8603, Japan

## Abstract

These days the low wear and high friction brake pad is needed from the viewpoint of environmental problems. Containing much kind of materials such as resin, abrasive, fiber, solid lubricant and so on, the brake pad is so complicated that we cannot design it theoretically. So, we simulated the brake pad model using only resin and abrasive, and suggested the way to design the low wear and high friction brake pad theoretically.

First of all, we investigated the relationship between the property of abrasive in the brake pad model: shape (ball, circular cone, pyramid), size, density and apex cone angle of the abrasive, and friction coefficient and wear volume using the abrasive theory. For example Fig. 1 shows the relationship between the apex cone angle of the abrasive and friction coefficient.

Next, in order to validate the brake pad model we carried out the scratch test with a diamond indenter (Shape: ball + circular cone). Fig. 2 shows the result of the scratch test and the theoretical value by the model.

From the scratch test we obtained the result that the model we made was almost correct. So we can use this model and will find the optimum abrasive condition.

## Biography

Miho Sumigama entranced Faculty of Engineering of Nagoya University in 2008, and will graduate in 2012, and will entrance Graduated School of Faculty of Engineering of Nagoya University.

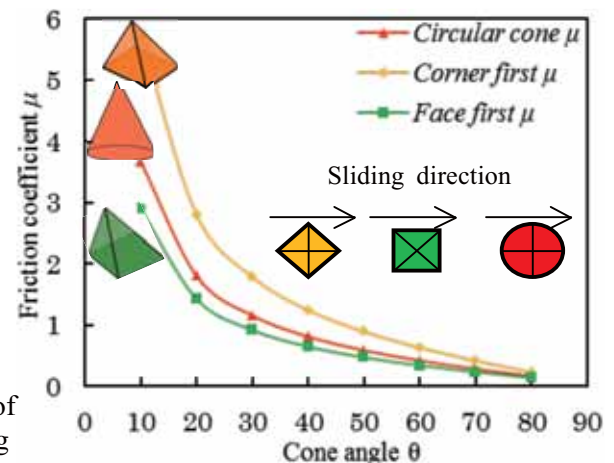


Fig. 1 The relationship between cone angle  $\theta$  and friction coefficient

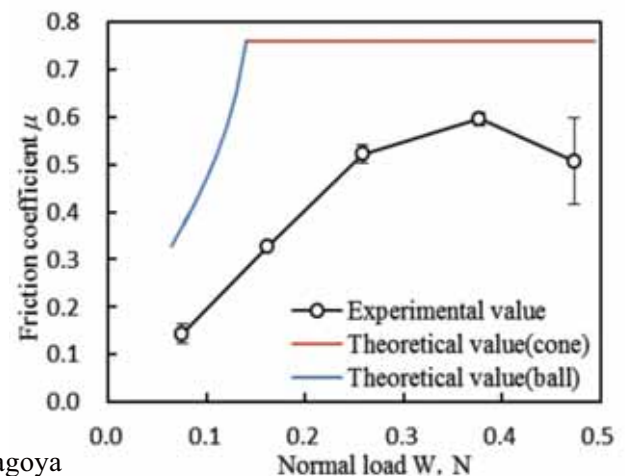


Fig. 2 The result of the scratch test and theoretical value

# Development of high friction and low aggression brake pad for next-generation automobile

Miho Sumigama Noritugu Umehara Hiroyuki Kousaka Takayuki Tokoroyama  
Nagoya University

## About the disk brake pad

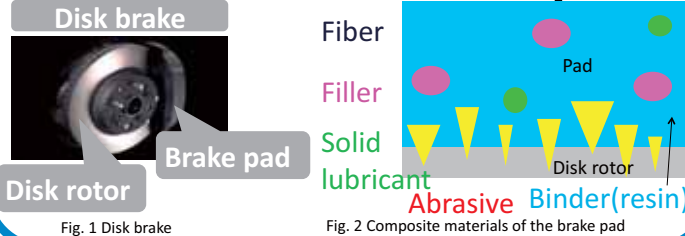


Fig. 1 Disk brake

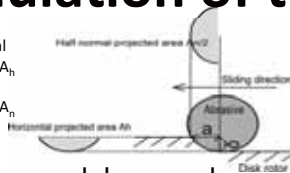
Fig. 2 Composite materials of the brake pad

## Problem and purpose

Containing much kind of materials (see Fig. 2), the brake pad is so complicated that we cannot design it theoretically. So, we simulated the brake pad model using only resin and abrasive, and **suggested the way to design the low wear and high friction brake pad theoretically.**

## Simulation of the brake pad model

Fig. 3 Horizontal projected area  $A_h$  and normal projected area  $A_n$



This is the model we made.

Friction coefficient  $\mu$

$$\mu = \alpha \mu_p + (1 - \alpha) \mu_a$$

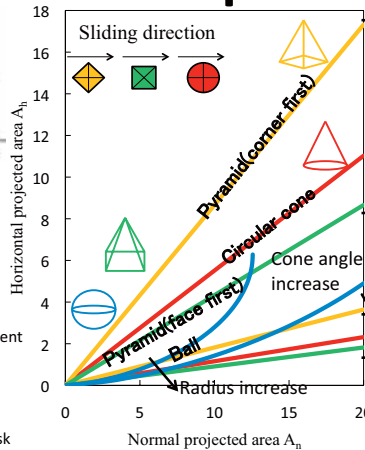
Ploughing component of friction coefficient  $\mu_p$

$$\mu_p = \frac{2}{\alpha} \cdot \frac{A_h}{A_n}$$

Wear volume  $V$

$$V = l f_{ab} \frac{W}{H} \mu_p$$

$\mu_a$ : Adhesion component of friction coef.  
 $l$ : Sliding distance  
 $f_{ab}$ : Wear rate  
 $W$ : Normal load  
 $H$ : Hardness of the disk



Ref.) J.Halling, PRINCIPLES OF TRIBOLOGY.  
S.Jacobson, Fundamental Aspects of Abrasive Wear Studied by a New Numerical Simulation Model, Wear 123 (1988).

Table 1 The relationship between the property of the abrasive and friction coefficient and wear volume

Property	Direction of Change	Result
Friction coef.	→	high
Wear vol.	→	much
Radius	←	●
Density	→	●
Cone angle	→	▼

We made the brake pad model and investigated the relationship between the property of the abrasive in it: shape, radius, density, cone angle and friction coefficient and wear volume.

Fig. 4 The relationship between the shape of the abrasive and the projected area

## Scratch test to demonstrate the brake pad model

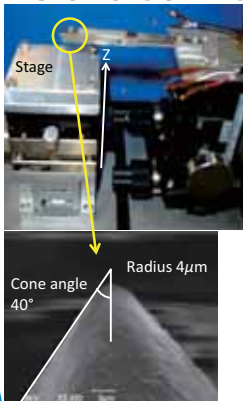


Fig. 5 Scratching apparatus  
Fig. 6 SEM image of diamond indenter

We carried out the scratch test with a diamond indenter (see Fig. 6). Fig. 7 and Fig. 8 shows the result of the scratch test and the theoretical value obtained by the brake pad model (with an abrasive). The experimental is along the theoretical.

Stage Z position $\mu\text{m}$ (Normal load $W$ )	+50, +100, +150, +200, +250
Sliding distance $l$ , mm	3
Disk rotor	Material: SUS304 Hardness $H$ , GPa: 6.06

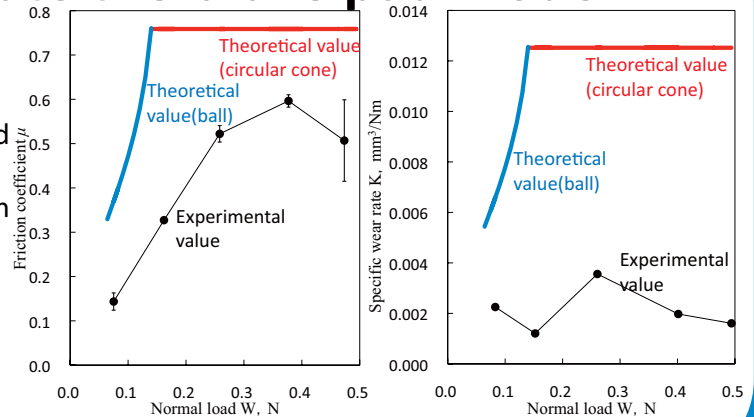


Fig. 7 and Fig. 8 The result of the scratch test and theoretical value(Fig. 7 Friction coefficient, Fig. 8 Wear volume)

## Conclusion and future plan

From the scratch test we obtained the result that the brake pad model was almost correct. So we can use this model and will find the optimum abrasive condition. For example we think the abrasive whose  $A_n$ - $A_h$  relationship is not linear for candidate, because wear volume was proportional to friction coefficient.

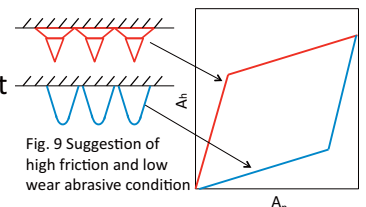


Fig. 9 Suggestion of high friction and low wear abrasive condition

# Relationship between Speed of Blade and Sharpness of Shaver



Naoya NAKANISHI

[nakanishi@mech.nagoya-u.ac.jp](mailto:nakanishi@mech.nagoya-u.ac.jp)

Noritsugu UMEHARA

[ume@mech.nagoya-u.ac.jp](mailto:ume@mech.nagoya-u.ac.jp)

Hiroyuki KOUSAKA

[kousaka@mech.nagoya-u.ac.jp](mailto:kousaka@mech.nagoya-u.ac.jp)

Takayuki TOKOROYAMA

[tokoroyama@mech.nagoya-u.ac.jp](mailto:tokoroyama@mech.nagoya-u.ac.jp)

School of Engineering, Nagoya University  
Furo-cho, Chikusa-ku, Nagoya 464-8603, JAPAN

## Abstract

Electric shaver is roughly divided into rotary and round trip type. The speed of the round trip type inner blades is not constant; it changes from 0 to the highest speed of 1.8 m/s. On the other hand, the speed of rotary type's inner blades is always constant such as 1.2 m/s. The aim of this research is to clarify the effect of inner blade speed for cutting sharpness of electric shaver.

The schematic image of apparatus to measure pulling force is shown in Fig. 1. The electric shaver was set on the fix arm and it is against the load-cell with an artificial hair glued on the tip. The cutting sharpness was evaluated by the pulling force when inner blade cut a hair. The hair is caught between the inner and outer blades and sheared in a scissor action. The force of this sharing action is thought to be the pulling force.

The relationship between inner blade speed and average pulling force is shown in Fig. 2. It was clear that the pulling force decreased with increasing inner blade speed.

Cross sectional SEM image of after cutting an artificial hair is shown in Fig. 3. The inner blade cut the hair toward one direction. The cutting process is assumed that inner blade penetrated into artificial hair with plastic deformation, then, it cut the hair by scissor action. This scissor action generated pulling force.

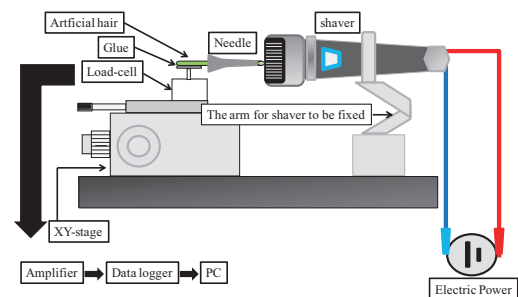


Fig.1 The schematic image of pulling force measuring apparatus

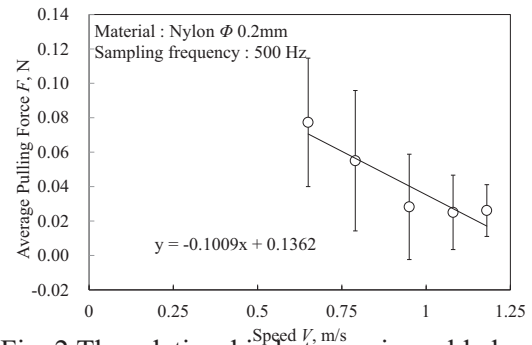


Fig. 2 The relationship between inner blade and average pulling force

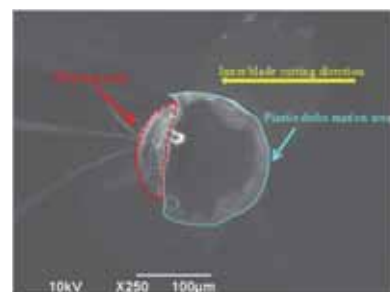


Fig. 3 Cross-sectional SEM image of the artificial hair cut by rotary type shaver

## Biography

Naoya Nakanishi will graduate Nagoya University in 2012

# Relationship between Speed of Blade and Sharpness of Shaver

N. Nakanishi N. Umehara T. Tokoroyama and H. kousaka Nagoya University March, 2012

## PURPOSE

Electric shaver is roughly divided into rotary (Fig. 1) and round trip type (Fig. 2), depending on the form of the inner blade of the electric shaver. The speed of the round trip type inner blades is not constant; it changes from 0 to the highest speed of 1.8 m/s. On the other hand, the speed of rotary type's inner blades is always constant such as 1.2 m/s.(Fig.3) The aim of this research is to clarify the effect of inner blade speed for cutting sharpness of electric shaver.



Fig.1 Rotary type shaver



Fig.2 Round trip type shaver

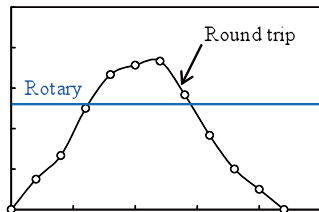


Fig. 3 Shaver's speed

## EXPERIMENT

The schematic image of apparatus to measure pulling force is shown in Fig. 4 and 5. The electric shaver was set on the fix arm and it is against the load-cell with an artificial hair glued on the tip.

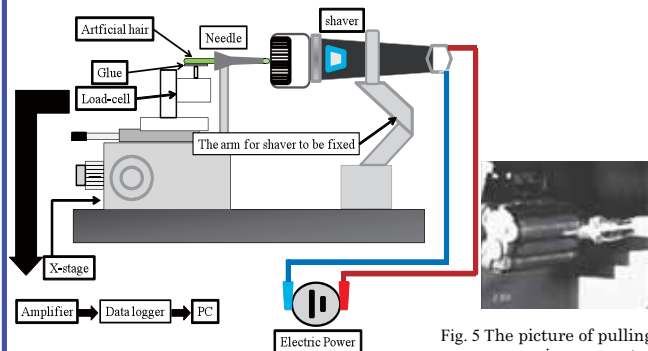


Fig. 4 The schematic image of pulling force measuring apparatus

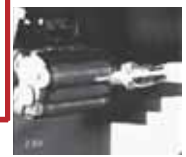


Fig. 5 The picture of pulling force measuring apparatus

## RESULTS

The relationship between inner blade speed and average pulling force is shown in Fig. 6. It was clear that the pulling force decreased with increasing inner blade speed. Cross sectional SEM image of after cutting an artificial hair is shown in Fig. 7 and microscopic image is done in Fig 8. The inner blade cut the hair toward one direction. The cutting process is assumed that inner blade penetrated into artificial hair with plastic deformation, then, it cut the hair by scissor action. This scissor action generated pulling force. Figure 9 shows the capture of high speed camera's video and pulling force with measuring time when shaver cut a hair.

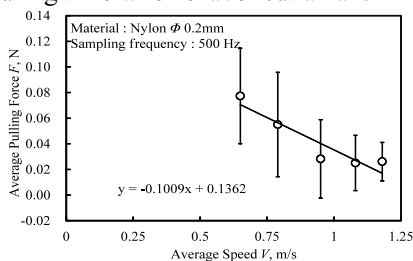


Fig.6 The relationship between inner blade speed and average pulling force

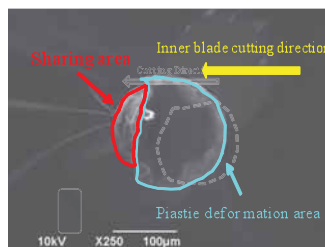


Fig. 7 Cross-sectional SEM image of the artificial hair cut by rotary type shaver



Fig. 8 Cross-sectional microscopic image of the artificial hair cut by rotary type shaver

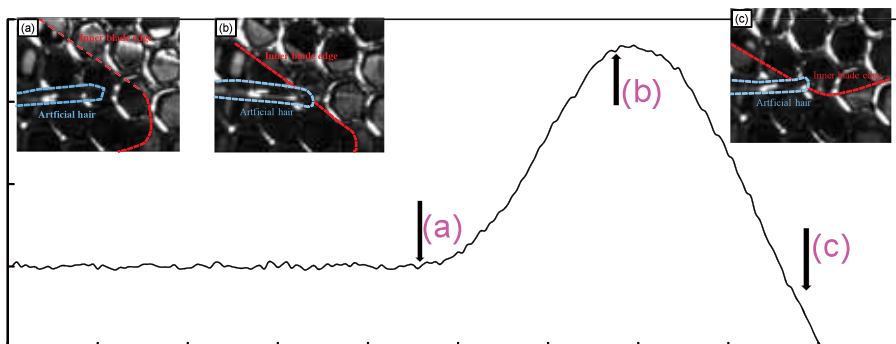


Fig. 9 The pulling force and the picture of high speed of camera

## CONCLUSION

It was clear that the pulling force decreased with increasing inner blade speed. Measuring pulling force of artificial hair is a simple and effective method to evaluate the cutting ability of an electric shaver.

# The clarification of the relationship between transfer layer and friction coefficient of carbonaceous coating



Hidenori NISHIMURA

[nishimura@ume.mech.nagoya-u.ac.jp](mailto:nishimura@ume.mech.nagoya-u.ac.jp)

Noritsugu UMEHARA

[ume@mech.nagoya-u.ac.jp](mailto:ume@mech.nagoya-u.ac.jp)

Hiroyuki KOUSAKA

[kousaka@mech.nagoya-u.ac.jp](mailto:kousaka@mech.nagoya-u.ac.jp)

Takayuki TOKOROYAMA

[tokoroyama@mech.nagoya-u.ac.jp](mailto:tokoroyama@mech.nagoya-u.ac.jp)

School of Engineering, Nagoya University

Furo-cho, Chikusa-ku, Nagoya, Aichi, 464-8603, JAPAN

## Abstract

The transfer layer built on an in front of the sapphire hemisphere which was mating material of carbonaceous coating such as DLC and CNx during friction (Fig. 1). It is one of the necessary conditions to appear an ultra-low friction coefficient ( $\mu < 0.01$ ). We revealed a structure and mechanical properties of transfer layer which showed ultra-low friction coefficient.

We measured the transfer layer thickness and the contact area. For the contact area, we suggested a new measurement method. We binarized the friction surface image taking by optical microscope through the sapphire hemisphere (including transfer layer), and we defined contact area (Fig. 2). Also, we measured the transfer layer nano-indentation hardness and Raman spectroscopy analysis as the mechanical properties of transfer layer.

The Fig. 3 shows the friction coefficient reduced despite the contact area increased, it was assumed that the shear strength of transfer layer was decreased. Since left of the blue area of Fig. 3 shows initial friction zone, we considered that graphitization of the transfer layer had been taking place at the period of right zone of the blue area, and reduced friction coefficient.

Also, in the red area of Fig. 3, the friction coefficient and the contact area increased. In this area, we suggested to stop decreasing the shear strength by finishing the graphitization of the transfer layer. So the friction coefficient was restricted by the contact area and the transfer layer thickness in the red area.

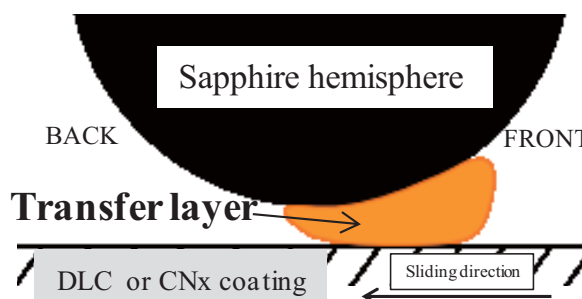


Fig. 1 Schematic image of transfer layer built on an in front of the sapphire hemisphere

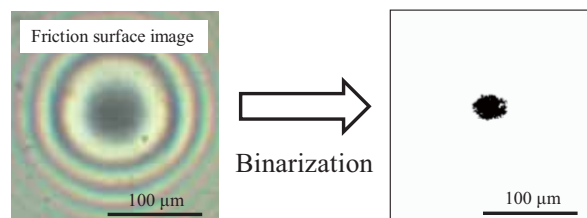


Fig. 2 The optical microscope image and picture of contact area by binarization

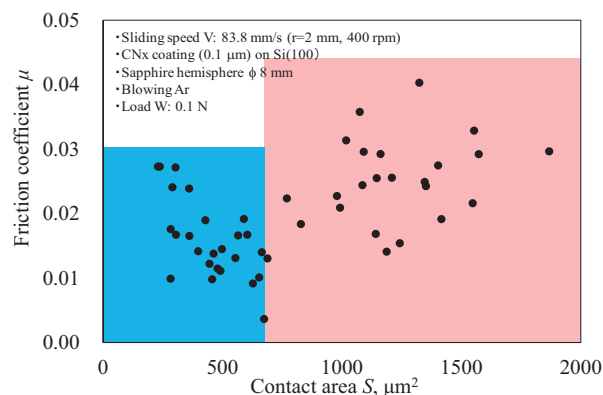


Fig. 3 The relationship between the contact area and the friction coefficient

## Biography

Hidenori Nishimura entered School of Engineering of Nagoya University in 2008, and will graduate in 2012.

# The clarification of the relationship between transfer layer and friction coefficient of carbonaceous coating

Hidehori Nishimura Noritsugu Umehara Hiroyuki Kousaka Takayuki Tokoroyama Nagoya University March, 2012

## Background and purpose

The transfer layer is one of the necessary conditions to appear an ultra-low friction coefficient ( $\mu < 0.01$ ) on carbonaceous coating (Diamond-Like Carbon or Carbon Nitride). Transfer layer was peeling material from carbonaceous coating, and it built on an in front of the sapphire hemisphere (Fig. 1).

However, the detail of transfer layer showed ultra-low friction coefficient was not reported enough. So, we revealed a structure and mechanical properties of it.

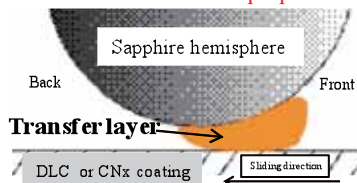


Fig. 1 Schematic image of transfer layer built on an in front of the sapphire hemisphere

## Experiment

### Pin-on disk friction tester

We used pin-on disk friction tester which can observe friction surface through the sapphire hemisphere (Fig. 2). Friction surface images was transferred to the computer from optical microscope via CCD.  $N_2$  or Ar gas was blew forward friction direction.

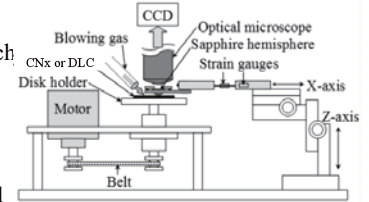


Fig. 2 Pin-on disk friction tester

### Measurement method of contact area

Binarizing a friction surface image, we calculated the number of black dots of a binary image. And we defined multiplication of the number of black dots and area per one dot as the contact area.

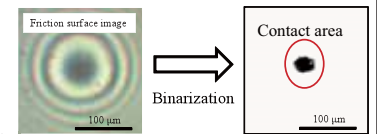


Fig. 3 The optical microscope image and picture of contact area by binarization

## Results

The relationship between the contact area and the friction coefficient is shown in Fig. 4 through 9. Each point of graphs was plotted every 30 seconds for the friction test. Also the relationship between the average nano-indentation hardness and the friction coefficient is shown in Fig. 10, and between change rate of  $I_D/I_G$  ratio from Raman analysis and the friction coefficient is shown in Fig. 11. Each point of graphs was plotted every friction test. We defined as change rate of  $I_D/I_G$  ratio = ( $I_D/I_G$  ratio of transfer layer) / ( $I_D/I_G$  ratio of carbonaceous film). The larger change rate of  $I_D/I_G$  ratio indicated the transfer layer changed to a graphite-like structure.

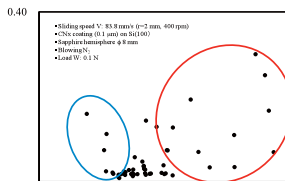


Fig. 4 CNx in blowing  $N_2$  test

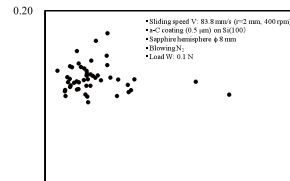


Fig. 6 a-C in blowing  $N_2$  test

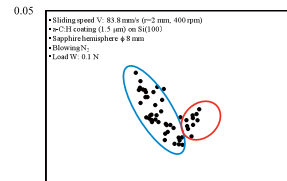


Fig. 8 a-C:H in blowing  $N_2$  test

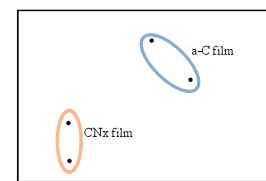


Fig. 10 transfer layer hardness

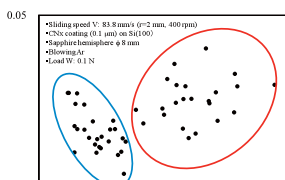


Fig. 5 CNx in blowing Ar test

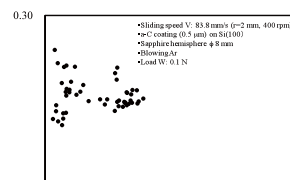


Fig. 7 a-C in blowing Ar test

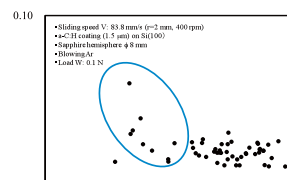


Fig. 9 a-C:H in blowing Ar test

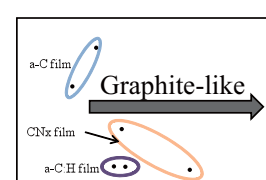


Fig. 11  $I_D/I_G$  ratio

## Discussion

There was optimum contact area that the friction coefficient was the smallest in some figures.

Graphitization of transfer layer (Fig. 10 and 11)  
→ decreasing shearing strength,  
so the friction coefficient decreased

Contact area increased and transfer layer thickness changed (Fig. 12)  
→ the friction coefficient increased

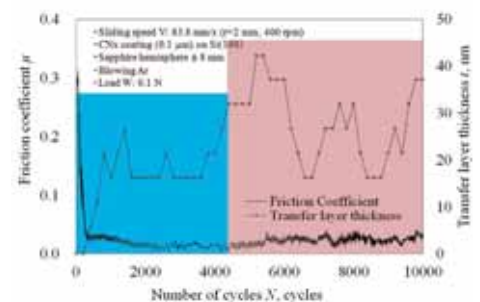
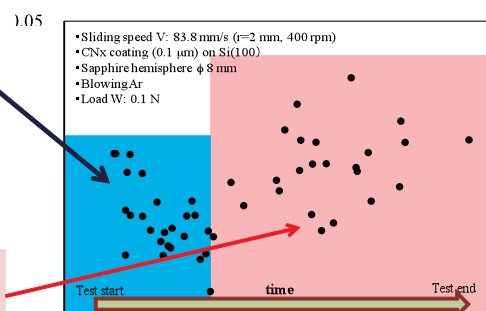


Fig. 12 The relationship between transfer layer thickness and friction coefficient

## Conclusion

- We suggested the new method to measure the contact area.
- There was the optimum value of the contact area that the friction coefficient was the smallest. And we proposed the friction mechanism before and after showed ultra-low friction coefficient at that time.

# Clarification of mechanism and Control techniques about droplets of the CN<sub>x</sub> coating by ion beam assisted deposition



Yuji Yagi

[yagi@ume.mech.nagoya-u.ac.jp](mailto:yagi@ume.mech.nagoya-u.ac.jp)

Noritsugu UMEHARA

[ume@mech.nagoya-u.ac.jp](mailto:ume@mech.nagoya-u.ac.jp)

Hiroyuki KOUSAKA

[kousaka@mech.nagoya-u.ac.jp](mailto:kousaka@mech.nagoya-u.ac.jp)

Takayuki TOKOROYAMA

[tokoroyama@mech.nagoya-u.ac.jp](mailto:tokoroyama@mech.nagoya-u.ac.jp)

School of Engineering, Nagoya University

Furo-cho, Chikusa-ku, Nagoya 464-8603, JAPAN

## Abstract

It has been reported that the carbon nitride (CN<sub>x</sub>) coating was the super-low friction in which friction coefficient was less than 0.01, and it attracts attention as a wear resistance and low friction material. When forming a CN<sub>x</sub> coating with Ion Beam Assisted Deposition (IBAD) method as shown in Fig. 1, it turns out that the small asperities called droplets to the CN<sub>x</sub> coating surface with thick-film-izing is generated, and it generates high friction, but neither the control method of droplets nor the generation mechanism is clear. So, in this research, the optimal coating conditions for controlling droplets are clarified by paying attention to the energy of an electron beam and the form of a carbon target.

The value of the filament current which adjusts electron beam intensity was formed as a coating to 300 nm thickness as five level which were different to 0.4~0.6 A. The relation of the average height of droplets and the filament current density are shown in Fig. 2. As a result, It was clear that the average height of the droplet became low when filament current density was made small.

The carbon target was processed like the form which evaporates by an electron beam. Although it was usually the filament current 0.4~0.6 A in CN<sub>x</sub> coating of thickness 1000 nm, it was able to be carried out in the filament current value 0.25~0.30 A by carbon target processing. The AFM image of these two CN<sub>x</sub> coating is shown in Fig. 4. As a result, usual droplets average height was  $H = 0.92 \mu\text{m}$  in the thick film, but it was able to control by processing a carbon target to droplets average height  $H = 0.52 \mu\text{m}$ .

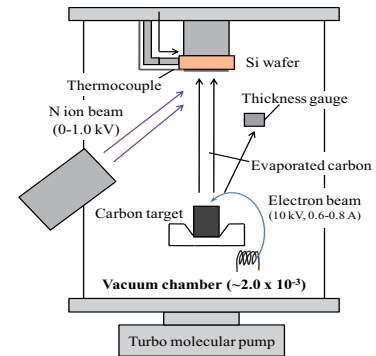


Fig. 1 Ion beam assisted deposition device

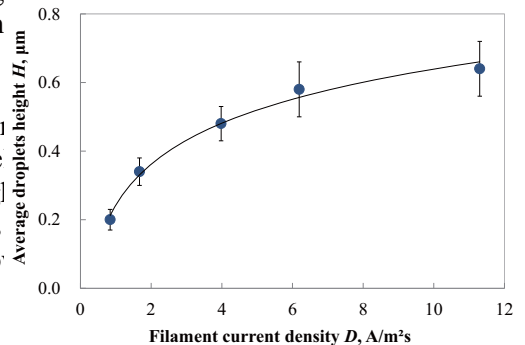


Fig. 2 The relation of the average height of droplets and the filament current density

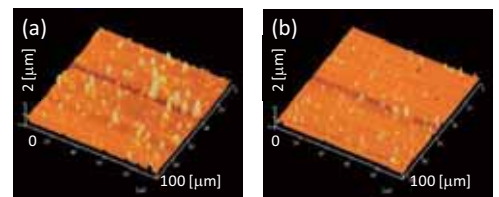


Fig3. AFM images (a) Usually and (b) Target processing

## Biography

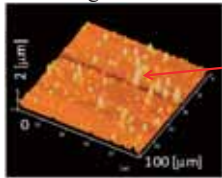
Yuji Yagi entered School of Engineering of Nagoya University in 2008, and will graduate in 2012.

# Clarification of mechanism and Control techniques about droplets of the CN<sub>x</sub> coating by Ion Beam Assisted Deposition

Y. Yagi, N. Umehara, T. Tkoroyama and H. kousaka Nagoya University March 2012

## PURPOSE

The Carbon Nitride (CN<sub>x</sub>) coating attracts attention as a high wear resistance and low friction material. But, when synthesizing a CN<sub>x</sub> coating with Ion Beam Assisted Deposition (IBAD) method, the small asperities called droplets to the CN<sub>x</sub> coating surface with increasing coating thickness were generated high friction. So, in this research, the optimal coating synthesizing conditions for controlling droplets are clarified by paying attention to the energy of an electron beam and the form of a carbon target.



Droplets

Fig.1 AFM image of CN<sub>x</sub> coating

## EXPERIMENT

Five CN<sub>x</sub> coatings of 300 nm were formed for every filament current.

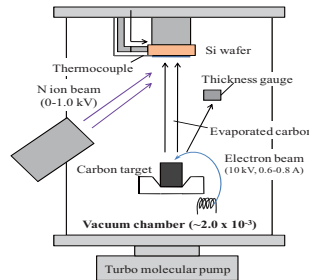


Fig.2 Schematic image of IBAD device

### (1) Experimental conditions

Substrate	Si(100) wafer
Thickness of CN <sub>x</sub> coating	300 nm
Power of electron beam (Filament current)	10 kV, 0.4, 0.45, 0.5, 0.55, 0.6 A
Coating time	26, 15, 7, 5, 3 minutes
Back pressure	2.0~4.0 × 10 <sup>-3</sup> Pa
N <sub>2</sub> sputter cleaning time	5 minutes
N <sub>2</sub> gas inflow	10 sccm
Accelerating voltage of N <sub>2</sub> ion beam	Accelerating : 1.0 kV A/D source : 1.0 kV
Temperature of cooling water	-20°C

CN<sub>x</sub> coatings of 1000 nm were formed in carbon target or processed it

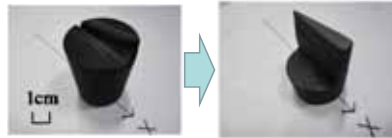


Fig.3 The picture of carbon target processing

### (2) Experimental conditions

Thickness of CN <sub>x</sub> coating	1000 nm	
Power of electron beam (Filament current)	Normal target 0.4~0.6 A	Processed target 0.25~0.3 A
Coating time	60 minutes	60 minutes

## RESULT

The relation of the average height of droplets and the filament current density is shown Fig.4. It turned out that the average height of droplets decreased with decreasing current density.

The surfaces of each coating was observed by AFM and SEM which were shown Fig.5. As a result, the droplets decreased and the average coefficient of friction was  $\mu=0.045$  by processing a carbon target.

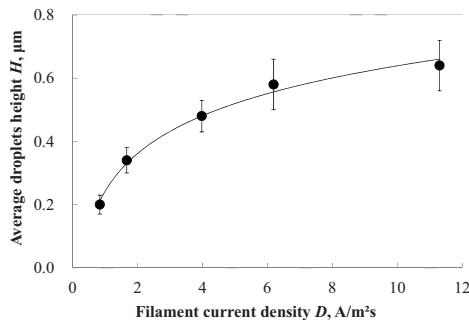


Fig.4 The relation of the average height of droplets and the filament current density

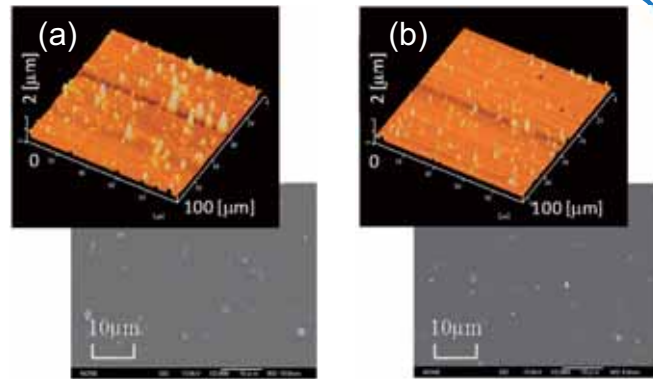


Fig.5 AFM and SEM images of CN<sub>x</sub> coating  
(a) Usually and (b) Target processing

Table1. Droplets height, area ratio and friction coefficient

	Normal target	Processed target
Average droplets height H (μm)	0.92	0.52
Droplets area ratio R (%)	2.4~3.2	1.6~1.9
Average friction coefficient	0.075	0.045

## CONCLUSION

It turned out that the average height of droplets decreased with decreasing current density. In CN<sub>x</sub> coating of 1000nm thickness, the droplets decreased and the average friction coefficient was  $\mu=0.045$  by processing a carbon target.

# Numerical Study on Combustion Characteristics of Ultra-micro Combustor with Porous Chamber Wall

Mingrui BAI

[bai@eess.mech.nagoya-u.ac.jp](mailto:bai@eess.mech.nagoya-u.ac.jp)

Hiroshi Yamashita

[yamashita@mech.nagoya-u.ac.jp](mailto:yamashita@mech.nagoya-u.ac.jp)

Graduate School of Engineering, Nagoya University

Furo-cho, Chikusa-ku, Nagoya 464-8603, JAPAN

Daiqing ZHAO

[zhaodq@ms.giec.ac.cn](mailto:zhaodq@ms.giec.ac.cn)

GuangZhou Institute of Energy Conversion, CAS

No.2 Wushan Nengyuan Street, Tianhe District, Guangzhou City 510620, China



## Abstract

In recent years, lots of micro power systems have been studied because of their high energy density. However, as small as their size will be, the heat loss from chamber wall becomes very remarkable. Aimed at that problem, the porous wall has been used as combustor inlet to recirculate combustion heat with inflow premixed gas.

In our study, we have investigated such an ultra-micro combustor with porous chamber wall by using our numerical calculation code (Fig.1). Furthermore, through altering computational conditions, which are preheating temperature  $T_0$ , inlet velocity  $U_0$  and equivalence ratio  $\Phi_0$ , we've elucidated internal combustion characteristics which could not obtain from experiments.

As a result, four types of combustion, which are steady-state, blowing-off, pulsating and extinction, have been observed (Fig.2). The combustible region becomes narrower when we decrease the preheating temperature. Moreover, combustion load becomes higher when we increase the inlet velocity and fuel equivalence ratio, and combustion efficiency becomes higher, reaches a maximum, and then decreases, when we increase the inlet velocity.

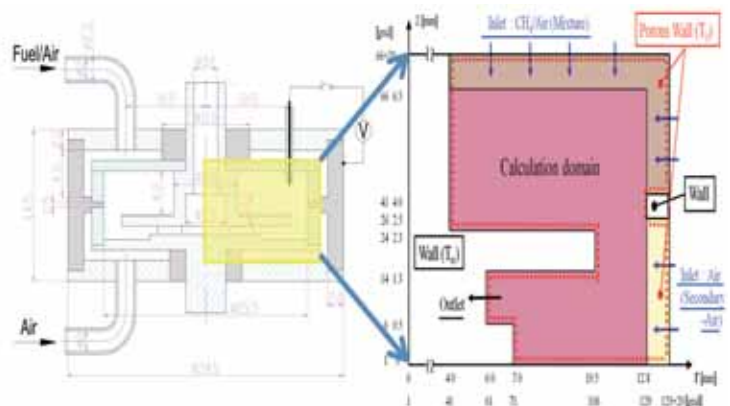


Fig.1 Schematic of analytical model

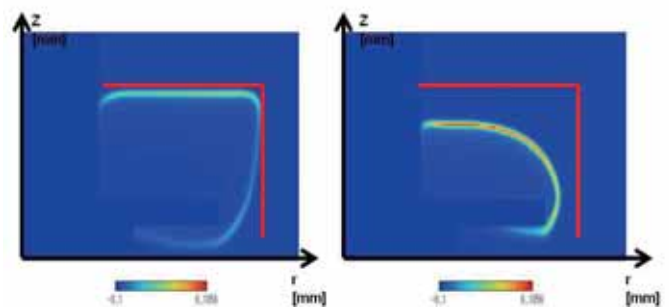


Fig.2 Combustion Aspect ( $T_0=700$  K)  
(Left: steady-state; Right: blowing-off)

## Biography

Mingrui BAI is a first-year student of master course in Graduate School of Engineering, Nagoya University. She is preparing to make a presentation of her study at the Japan Society of Mechanical Engineers, Tokai Branch in March, 2012.

# Numerical Study on Combustion Characteristics of Ultra-micro Combustor with Porous Chamber Wall

Mingrui BAI, Hiroshi YAMASHITA Nagoya University  
 Daiqing ZHAO Guangzhou Institute of Energy Conversion of CAS

## Objectives

With the advantage of high energy density, lots of micro power systems have been studied in recent years. However, as small as their size will be, the heat loss from chamber wall becomes very remarkable. Aimed at that problem, we used the porous wall as combustor inlet to recirculate combustion heat with inflow premixed gas. And, with altering the computational conditions, we examined internal combustion characteristics which could not obtain from experiments.

## Computational Conditions

- The flow rate boundary condition of Premixed gas and Secondary air  
 $Q_M : Q_S = 1 : 0.75$  (fixed)  
 $U_0 : 0.112 \text{ m/s} \sim 2.77 \text{ m/s}$  (premixed gas)
- The temperature and equivalence ratio of premixed gas  
 Equivalence ratio  $\Phi_0 : 0.6 \sim 1.0$   
 Preheating temperature  $T_0 : 400 \text{ K} \sim 700 \text{ K}$
- The temperature of chamber wall  
 Restricted temperature  $T_W : 1000 \text{ K}$

## Analytical Model

- Governing equations
  - Continuity equation
  - Conservation equation of momentum
  - Species mass conservation equations
  - Energy conservation equation
  - Equation of state
- Reaction mechanism
  - Skeletal elementary reaction of  $\text{CH}_4/\text{Air}$  with 16 chemical species and 25 pairs of elementary reactions.
- Transport coefficients
  - Simplified transport model

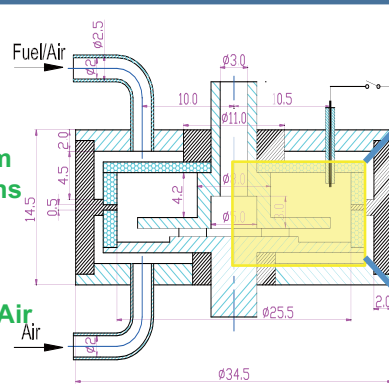


Fig.1 Ultra-micro combustor

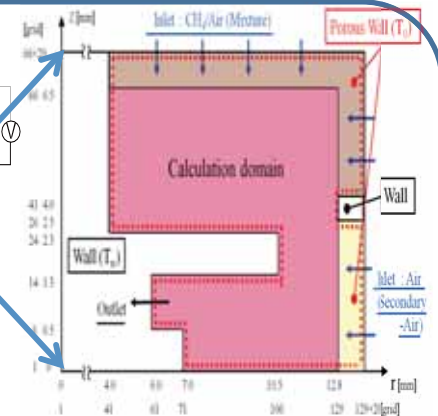


Fig.2 Schematic of analytical model

## Results

### 1. Combustion aspect

Through altering the  $T_0$ ,  $U_0$  and  $\Phi_0$ , we confirmed four types of combustion, which are steady-state (St), blowing-off (Bl), pulsating (Pu) and extinction (Ex) (Fig.3). We can only observe the pulsating combustion in slow inlet velocity for the reason of heat loss in chamber wall and burning velocity.

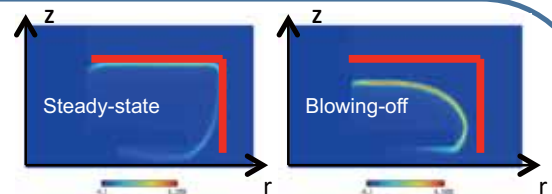


Fig.3 Combustion aspect ( $T_0 = 700\text{K}$ )

Table 1 Flammable regions

$\Phi_0/U_0$ [m/s]	0.112	0.225	0.692	1.394	1.94	2.77
(a) 0.6	Pu	St	St	St	St	St
0.7	Pu	St	St	St	St	St
0.8	Pu	St	St	St	St	St
0.9	Pu	St	St	St	St	St
1	Pu	St	St	St	St	St
(b) 0.6	Ex	Pu	St	St	St	St
0.7	Pu	St	St	St	St	St
0.8	Pu	St	St	St	St	St
0.9	Pu	St	St	St	St	St
1	Pu	St	St	St	St	St
(c) 0.6	Ex	St	Bl	Bl	Bl	Bl
0.7	Pu	St	St	St	St	St
0.8	Pu	St	St	St	St	St
0.9	Pu	St	St	St	St	St
1	Pu	St	St	St	St	St
(d) 0.6	Ex	Pu	Bl	Bl	Bl	Bl
0.7	Pu	St	St	St	St	St
0.8	Pu	St	St	St	St	St
0.9	Pu	St	St	St	St	St
1	Pu	St	St	St	St	St

(a)  $T_0 = 700\text{K}$   
 (b)  $T_0 = 600\text{K}$   
 (c)  $T_0 = 500\text{K}$   
 (d)  $T_0 = 400\text{K}$

### 2. Flammable regions

With decreasing the preheating temperature  $T_0$ , we found that flammable limits is becoming smaller and smaller (Table 1). This can be explained by that preheated premixed gas can promote combustion.

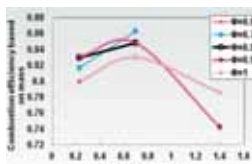


Fig.4 Combustion efficiency

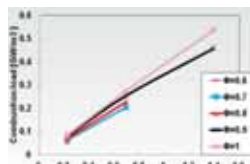


Fig.5 Combustion load

### 3. Combustion efficiency and Combustion load

From the calculation data, it is cleared that when we increase the inlet velocity, combustion load becomes higher, and combustion efficiency firstly becomes higher, reaches a maximum, and then decreases at each preheating temperature (Figs.4 and 5).

## Conclusions

- With changing  $T_0$ ,  $U_0$  and  $\Phi_0$ , four types of combustion, steady-state, blowing-off, pulsating and extinction have been observed. Moreover, when we decrease preheating temperature, the flammable regions become narrower.
- The combustion load is becoming higher when we increase the inlet velocity. However, combustion efficiency is firstly becoming higher, reaches a maximum, and then decrease at each preheating temperature.

# Application of molecular tagging velocimetry to rarefied gas flow



Akichika Yamaguchi

yamaguchi.akichika@b.mbox.nagoya-u.ac.jp

Hiroki Yamaguchi

hiroki@nagoya-u.jp

Tomohide Niimi

niimi@mech.nagoya-u.ac.jp

Graduate School of Engineering

Furo-cho, Chikusa-ku, Nagoya 464-8603, JAPAN

## Abstract

Knudsen number ( $Kn = \lambda/L$ ) is a non-dimensional parameter representing the rarefied degree of gas flows, where  $\lambda$  is the mean free path and  $L$  is the characteristic length of a flow field. The flow whose Knudsen number is beyond 0.01 is called “high Knudsen number flow”: for instance, rarefied gas flows ( $\lambda$ : large) and micro-/nano-flows ( $L$ : small). Recently, not only for detailed investigation but also for verifying numerical simulations on high Knudsen number flows, the development of new techniques for velocity field measurement is required.

There are many velocimetry techniques by visualization of a flow field: such as, PIV (Particle Image Velocimetry), PSV (Particle Streak Velocimetry) and MTV (Molecular Tagging Velocimetry). PIV and PSV are very common and widely used in liquid flows, which needs seeding of particles into the flow. Therefore, especially in gaseous flows, these techniques have the problems of speed separation from flow and damage or adhesion to walls. In contrast, MTV is molecular based technique, where molecules in the flow are tagged and tagged molecules are visualized, and the displacement of the visualized molecules during a small time duration leads to the flow velocity. This technique is free from the above mentioned problems. Therefore, MTV is best suited to analyze velocity field in high Knudsen number flow.

A supersonic free jet was employed as a typical rarefied gas flow to demonstrate MTV technique in high Knudsen number flow. For the visualization of tagged molecules, the laser induced fluorescence (LIF) was employed. As a result, velocity on the central axis of a super sonic free jet with pressure ratio of 2000 was calculated as  $767 \pm 21$  m/s. Compared with the theoretical value of 751.0 m/s – 754.7 m/s, experimental result indicated good agreement.

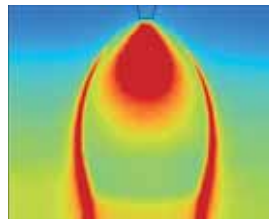


Fig.1 Pseudo color LIF image of super sonic free jet

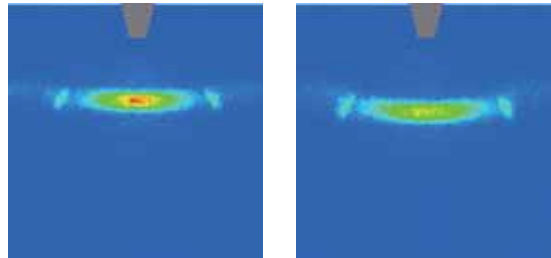


Fig.2 Typical example of visualized super sonic free jet with certain time duration

## Biography

Akichika Yamaguchi received the Bachelor’s degree in Engineering from Nagoya University. He is currently a graduate school student in Nagoya University, focusing on the studies of analyzing high Knudsen number flows.

# Application of molecular tagging velocimetry to rarefied gas flow



Akichika Yamaguchi, Hiroki Yamaguchi, Kojiro Kawabe,  
Yuki Nakashima, Yu Matsuda, Tomohide Niimi



## Background

**Knudsen number** : represents the rarefied gas flow

$$Kn = \frac{\lambda}{L} \quad \begin{cases} \lambda : \text{mean free pass} \\ L : \text{characteristic length} \end{cases}$$

### Rarefied gas flow

high Knudsen number flow ( $\lambda$  : large)

- It cannot be dealt with as continuum flow
- Precise experimental data are required



<http://www.rochesterastronomy.org/node/942>

## Target

Not only for detailed investigation but also for verifying numerical simulations on high Knudsen number flows, the development of new techniques for velocity field measurement is required.



**We aim to develop a technique to measure velocity in rarefied gas flow field**

## Technique

### Optical measurements

**LDV** (Laser Doppler Velocimetry)

Limited to 1-D measurement

**PIV** (Particle Image Velocimetry)

**PSV** (Particle Streak Velocimetry)

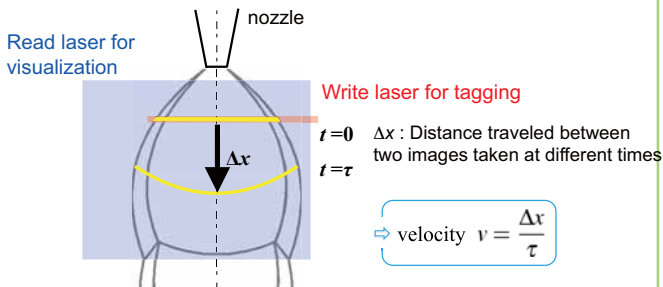
In gaseous flows, have the problems of

- speed separation from flow
- damage or adhesion to walls

### MTV (Molecular Tagging Velocimetry)

After tagging molecules in a flow field, velocity is measured by tracking the tagged molecules

- Non-invasive method
- Molecular scale information
- Free from speed separation



### Tagging techniques

**Write : Tagging : photodissociation of NO<sub>2</sub>**

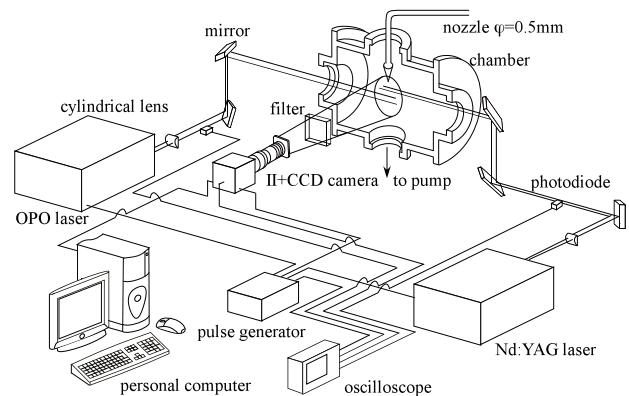
Dissociation by laser having wavelength below 398nm  
 $\text{NO}_2 + h\nu \rightarrow \text{NO} + \text{O}$  ⇒ 3rd harmonics of Nd:YAG laser

- Molecular weight of NO is close to that of air. → no effect of speed separation
- It is easy to trace NO ← Fluorescence intensity of NO is comparatively large

**Visualizing detection : NO-LIF**

Excitation by laser, leading to fluorescence of NO ⇒ OPO laser

## Equipment



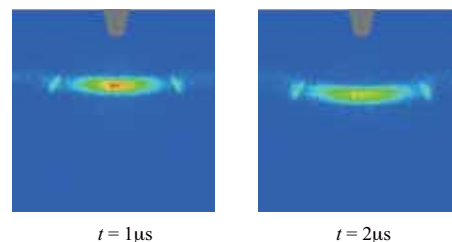
Nozzle diameter	0.5mm
Pressure ratio	2000
Source pressure	$1.0 \times 10^5 \text{ Pa}$
Back pressure	50Pa
NO <sub>2</sub> density	1%

Wavelength of OPO laser	226nm
Power of OPO laser	1.40mJ/pulse
Wavelength of YAG laser	355nm
Power of YAG laser	20.0mJ/pulse

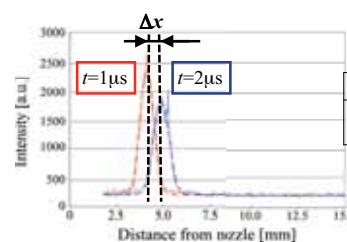
frequency	10Hz
Gate range	200ns
Cumulated number of image	100

## Result

Time delayed images in a supersonic free jet



Displacement is calculated by fitting luminescent intensity distributions by Gaussian functions



Result	767 ±21 m/s
Theoretical value Ashkenas & Sherman	752.9± 1.9m/s

\* error is deduced by a pixel

# A Study on Human Avoidance Motion for Human-Robot Coexistence Systems



Koji SUNADA

sunada.koji@e.mbox.nagoya-u.ac.jp

Yoji YAMADA

yamada-yoji@mech.nagoya-u.ac.jp

Graduate School of Engineering, Nagoya University  
Furo-cho, Chikusa-ku, Nagoya 464-8603, JAPAN

## Abstract

At production site, a human-robot coexistence system is desired due to its flexibility and efficiency. To realize such system, the worker's risk needs to be estimated exactly with taking human avoidance motion into consideration. We have investigated human avoidability of harm to eyes in a typical human-robot coexistence system. The result will contribute to reasonably estimating avoidability, which currently tends to be estimated intuitively by assessors.

We have conducted psychological experiments for investigating human avoidance action characteristics. Fig.1 shows the situation of the psychological experiments. As the result, it was suggested that the shorter the initial distance between the eyes of a participant and the end-effector tip of the robot was, the shorter avoidance reaction time was. The end-effector motions were set not to touch the participants for securing safety.

To assess that human avoidance motion contributed human avoidability, we extrapolated simulation experiments in hazardous situations from the experimental data as shown in Fig.2, and termed such simulation "extrapolating simulation". We supposed that the modification of end effector motions did not affect human avoidance motion significantly. In the simulation, a human model's motion is same as participant's motion observed in the psychological experiment whole time. On the other hand, an end effector accelerates to the human model in the same motion as that in the psychological experiments, and then moves in hazardous modified motion. In this study, we assumed that the end effector moved straight to a human model's eye at uniform speed.

Eye-end effector collision simulations were carried out with various speeds of the end effectors in uniform motion. As the result, the motion range of the end effectors for securing safety was determined in each of the speeds (Fig.3). For example, when the initial distance between a human eye and an end-effector tip was about 495 mm and the uniform speed of the end effector was 950 mm/s, the human's avoidance distance was about 25 mm according to the simulations. This difference of 25 [mm] would contribute the increase of the possibility of avoiding or limiting harm. This result indicates quantitatively human avoidability of harm to eyes in the typical human-robot coexistence system.

## Biography

Koji Sunada got an engineering degree from Nagoya University in 2011. He joins Academy for Safety Intelligence, which proposes a new interdisciplinary research field schematized as "Safety Intelligence". He is working on constructing innovative human-support machines for sustainable society.



Fig.1 Psychological experiment

Fig.2 Extrapolating simulation

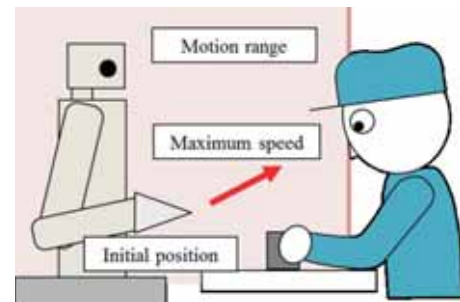


Fig.3 Human-robot coexistence conditions determined by the simulation



# A Study on Human Avoidance Motion for Human-Robot Coexistence Systems

in March, 2012

Koji SUNADA Yoji YAMADA

## Objective

The risk of a robot is estimated without taking human avoidance motion into consideration. This study investigates **human avoidability** of harm to **eyes** in a typical **human-robot coexistence system**. The result will contribute to estimating avoidability, which currently tends to be estimated intuitively by assessors.

## Psychological Experiment

Experiments in safety situations



## Supposition

An end-effector tip of a robot at a production site suddenly approaches the eyes of a worker sitting in front of the robot.

## Note

The end-effector motions were set **not** to touch the participants for securing safety.

**How much does the human avoidance motion contribute human avoidability?**

## Extrapolating Simulation

Experiments in hazardous situations

## Assumption

Modification of end-effector motions does not affect human avoidance motions significantly.

**Human model** Observed motion whole time

**End-effector model**

【During acceleration】 Observed motion

【After】 Modified hazardous motion

We assumed that an end effector moved straight to human model's eye at uniform speed (Fig.1).

## Result

Consideration of human avoidance motion makes a few centimeter margin (Fig.2).

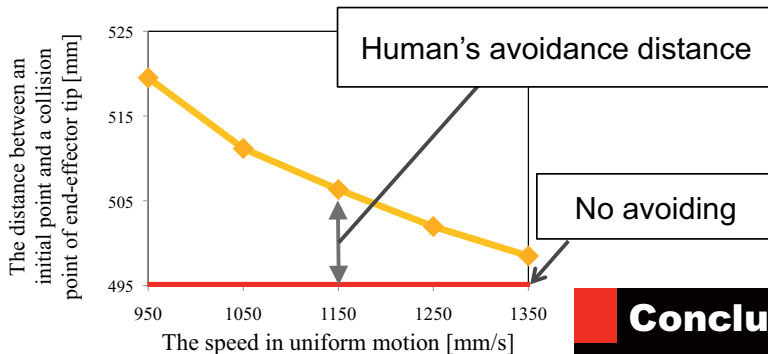


Fig.2 Distance at which an end effector moved until colliding with the human model in the worst trial

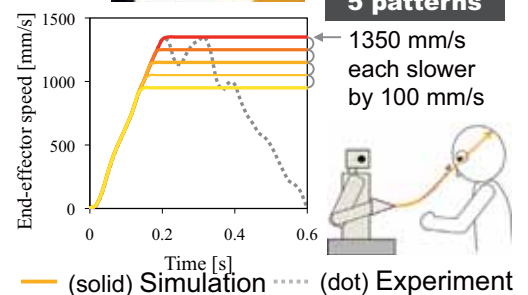


Fig.1 Speed patterns of an end effector in simulation and experiment

## Discussion

- ◆ The motion range of the end effectors for securing safety could be determined based on Fig.2.
- ◆ Human avoidance motion would contribute the increase of the possibility of avoiding or limiting harm to eyes.

## Conclusion

We showed quantitatively human avoidability taking human avoidance motion into consideration in the typical human-robot coexistence system.

# Basic Eye Part Collision Experiments against Sharp Mechanical Hazards for Severity Investigation



Soichiro ITO

ito.soichiro@a.mbox.nagoya-u.ac.jp

Yoji YAMADA

yamada-yoji@mech.nagoya-u.ac.jp

Graduate School of Engineering, Nagoya University  
Furo-cho, Chikusa-ku, Nagoya 464-8603, JAPAN

## Abstract

At production sites, a human-robot cooperative working system is desired. To realize such system, the worker's risk needs to be estimated exactly.

We assume that a sharp end effector of a robot approaches the eye of a human in a human-robot coexistence system. The human will perform avoidance/mitigation action against the approaching end effector. The aim of this study is to investigate how change of collision condition due to human avoidance/mitigation action influences the severity.

We have conducted basic eye part collision experiments taking human avoidance/mitigation actions into consideration (Fig.1). In the experiments, three conditions (open/close eyelid, collision positions, and collision angles) were changed. As the result, it was confirmed that each of the conditions to brings differences to severity (Fig. 2). For example, the severity was estimated low by closing eyelid.

Change of collision condition due to human avoidance/mitigation action will enable the human to avoid serious injury. Although possibility of avoidance/mitigation was not taken into consideration in past eye part collision experiments, we consider that it is indispensable to risk estimation.

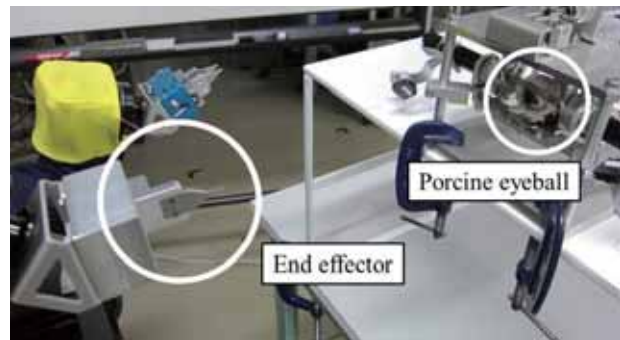


Fig.1 Eye part collision experiments

	0 [deg]	30 [deg]	45 [deg]
Open eyelid	×	△	△
Close eyelid	×	△	○

(a) Collision with cornea

	0 [deg]	30 [deg]	45 [deg]
Open eyelid	△	○	○
Close eyelid	○	○	○

(b) Collision with sclera

- : No injury could be confirmed
- △ : Eyeball surface got injured
- × : End effector punched eyeball, and vitreous got out

Fig.2 Result of collision experiment

## Biography

Soichiro Ito received the bachelor degree in engineering from Nagoya University in 2011. He is currently in the first year of the master's program in Nagoya University, focusing on the studies of risk estimation in a human-robot coexistence system.

# Basic Eye Part Collision Experiments against Sharp Mechanical Hazards for Severity Investigation

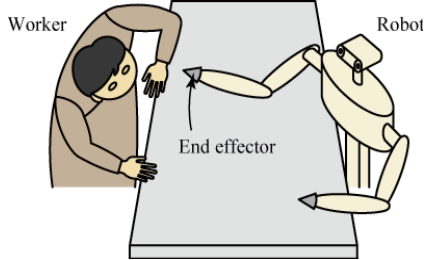
Soichiro Ito Yoji Yamada Nagoya Univ., Japan

## Background

Human-robot cooperative working system

### Assumed situation

A sharp end-effector tip of a robot suddenly attacks the eyes of a worker.



Originating Accident	Avoidance of body/head	Collision at eye (Collision conditions)	Severity	Accident chain
	SA		-	EA·SA
EA	FA	LC	Low	EA·FA·LC
		SC	High	EA·AB·SC

EA : End effector attacks

SA : Succeed in avoiding, FA : Fail in avoiding

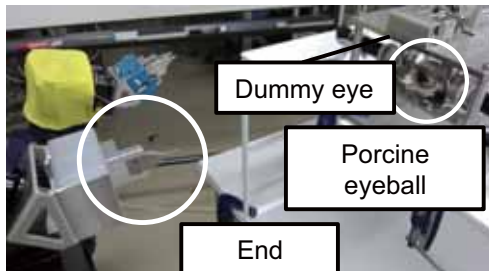
LC : Loose condition, SC : Severe condition

### Study Objective

- Human avoidance/mitigation action will change collision conditions.
- Doesn't it necessarily result in serious injury depending on collision conditions?

The aim of this study is to investigate how change of collision conditions due to human avoidance/mitigation action influences the severity.

## Experiment



- End effector collided with dummy eye.
- Collision conditions (collision angle, collision position, open/close eyelid) were changed.

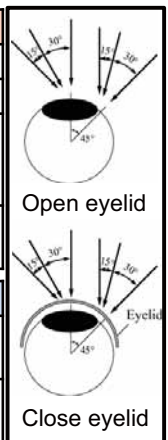


The severity of eyeball was investigated.

### Collision conditions

Impactor : End-effector tip	
Operation method	Robot's right arm was operated in a straight line
Collision speed	About 280 mm/s
Collision angle	① Normal direction (0 [deg]) ② 30 [deg] from normal direction ③ 45 [deg] from normal direction
Collision position	① Cornea ② Sclera

Collision target : Dummy eye	
Eyelid	① Open eyelid ② Close eyelid (Artificial eyelid)
Soft tissue	• 1 DOF in the direction of optical axis • Compression springs (Spring constant : 19.9 N/mm)



## Result

### Collision position

The severity of collision with sclera was estimated lower than that of cornea.

### Injury conditions

○ : No injury could be confirmed

△ : Eyeball surface got injured

× : Effector punched eyeball, and vitreous got out

### Collision with cornea

	0 [deg]	30 [deg]	45 [deg]
Open eyelid	×	△	△
Close eyelid	×	△	○

### Collision with sclera

	0 [deg]	30 [deg]	45 [deg]
Open eyelid	△	○	○
Close eyelid	○	○	○

Punched cornea



### Open/close eyelid

The severity was estimated low by closing eyelid.

### Collision angle

If the human can avoid collision from normal direction, the severity is estimated low.

## Conclusion

Change of collision conditions due to human avoidance/mitigation action will enable the human to avoid serious injury.

# What Appeals to Human Touch?

## - Comprehensive Study of Textures that Give an Incentive for Haptic Exploration -



Hikaru NAGANO

nagano.hikaru@h.mbox.nagoya-u.ac.jp

Shogo OKAMOTO

okamoto-shogo@mech.nagoya-u.ac.jp

Yoji YAMADA

yamada-yoji@mech.nagoya-u.ac.jp

Graduate School of Engineering, Nagoya University  
Furo-cho, Chikusa-ku, Nagoya 464-8603, JAPAN

### Abstract

**Background:** Some textures and materials appeal to our touch in daily life. What makes us intuitively feel like touching them? Haptic invitation for such textures has rarely been investigated.

**Objective:** The present report specifies the relationships between the physical and sensory properties of textures and the degrees of haptic invitation.

**Method:** We used 24 artificial clay textures that were varied along four physical factors as shown in Fig.1. We specified the sensory factors of textures through a sensory evaluation and a factor analysis and then quantified the degrees of affinity for these textures using a normalized-rank approach. Multiple regression analyses were performed to investigate the relationships between the degrees of affinity for textures and texture factors.

**Results:** The surface glossiness and shape patterns of textures strongly affected degrees of affinity and that surface colors had little impact. A sensory evaluation of the clay textures using factor analysis yielded four sensory factors. Dry and simple factors strongly affected the degrees of affinity. Furthermore, we found that apparent comfort is intimately related to the attractiveness of textures. The physical and sensory factors effectively captured 68% and 75% of the variance respectively (Fig.2.)

**Conclusion:** We revealed the factors of textures that appeal to human touch and specified the linear connection of the factors of textures could describe the affinity effectively.

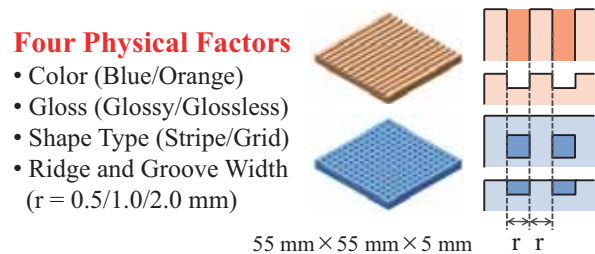


Fig.1 Clay-made molded textures

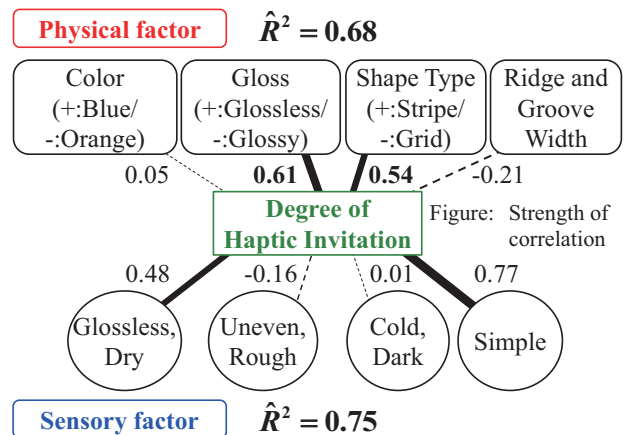


Fig.2 Relationships between physical, sensory factors and degrees of haptic invitation

### Biography

Hikaru NAGANO received a B.S, degree in engineering from Nagoya University, Japan in 2010. Currently, he is a Ph.D. candidate in the Department of Mechanical Science and Engineering, Nagoya University. His research interests include human perception.

# What Appeals to Human Touch?

Comprehensive Study of Textures that Give an Incentive for Haptic Exploration

Hikaru NAGANO Shogo OKAMOTO

Yoji YAMADA Nagoya Univ.

## Motivation

Some textures invite human touch motions in daily life

Measurement and design methodology of textures' haptic invitation have rarely been developed

- **Measurement:** To establish a statistical index representing the degree of haptic invitation
- **Design:** To investigate how to design textures that invite human touch motions



## Measurement

To quantify the degree of haptic invitation for textures

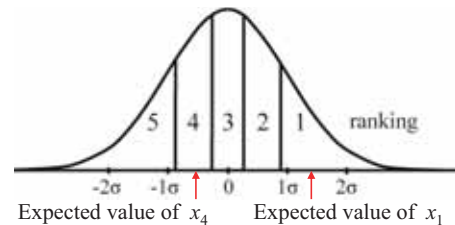
- ✗ **Difficult:** To quantify degrees directly. Ex. visual analog scales, magnitude estimation methods
- **Easy:** To judge which of textures are attractive to participants.
- ➔ **Ranking textures** Explicit criteria

To convert ranks (Ordinal scale) to degrees (Interval scale)

**Degree of Haptic Invitation**

: Expected values of textures from a normal distribution

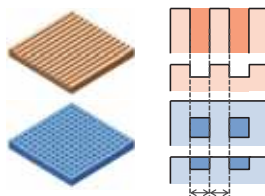
- ➔ **Normalized rank approach** Reasonable and Robust



## Design

How and to what extent physical and sensory factors of textures describe degrees of haptic invitation ?

### Stimulus



Clay-made molded textures (55 mm × 55 mm × 5 mm)

### Four Physical Factors

- Color (Blue/Orange)
- Gloss (Glossy/Glossless)
- Shape Type (Stripe/Grid)
- Ridge and Groove Width (r = 0.5/1.0/2.0 mm)

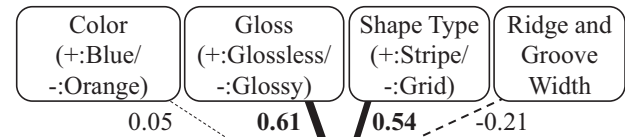
### Experiments

- Task1: Sensory evaluation + Factor analysis ➔ **Four Sensory Factors**
  - Factor1: Glossless, Dry
  - Factor2: Uneven, Rough
  - Factor3: Cold, Dark
  - Factor4: Simple
- Task2: Ranking method + Normalized rank approach

**Degree of Haptic Invitation**

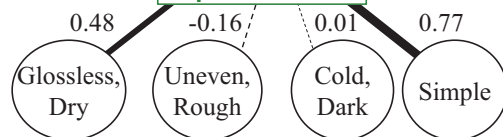
### Multi Regression Analysis

**Physical factor**  $\hat{R}^2 = 0.68$



**Degree of Haptic Invitation**

Figure: Strength of correlation



**Sensory factor**  $\hat{R}^2 = 0.75$

The methodology for determining the best combinations of factors in terms of haptic invitation was established

## Conclusion

- The degrees of haptic invitation were measured by a ranking system and the normalized-rank approach.
- The physical and sensory factors effectively described the degrees of haptic invitation with accuracies of 68% and 75%, respectively.

# Noncontact Nanometric Positioning of Probe Tip for Measurement of Mechanical Parameters of Cell



Keitaro Ito

ito.keitaro@biorobotics.mech.nagoya-u.ac.jp

Shinya Sakuma

sakuma@biorobotics.mech.nagoya-u.ac.jp

Fumihito Arai

arai@mech.nagoya-u.ac.jp

Department of Mechanical and Aerospace Engineering  
Nagoya University  
Furo-cho, Chikusa, Nagoya, Japan 464-8603

## Abstract

In the bioengineering field, it is important to apply the mechanical stimulation to the cell for the purpose of measuring the mechanical parameter of the cell and analyzing the response of the cell. Recently, many researchers give a great attention to the quality of the cells by measuring the mechanical parameters of the cells. In the on-chip cell manipulation field, the important features of the actuation method are the power and the resolution of manipulation. In order to obtain the nanometric order resolution with high power, we proposed the reduction mechanism. This mechanism utilizes the serially-connected springs with different stiffness, and is driven by magnetic force. (Fig. 1). Probe features are shown as follows: (1) probe is actuated in a microfluidic chip, (2) high power and high resolution in positioning, (3) robust from disturbance by employing parallel plate structure, and (4) chip part is disposable. In this paper we developed on-chip nanometric probe with reduction mechanism. The performance of the probe was examined. We succeeded in nanometric order non-contact actuation of on-chip probe tip by using reduction mechanism.

Fig.2 shows the evaluation of the repetitive positioning accuracy. The performance of the probe was examined, and the result shows that the standard deviation of displacement of probe tip was under  $0.18 \mu\text{m}$  (Tab.1). The manipulation power was estimated to several  $100 \mu\text{N}$ . Consequently we succeeded in nanometric order non-contact actuation of on-chip probe with a relatively high power.

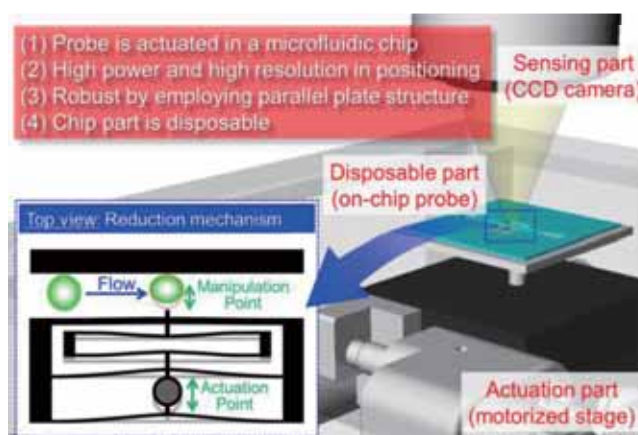


Fig.1 Concept of on-chip probe with nanometric resolution in positioning by using reduction mechanism

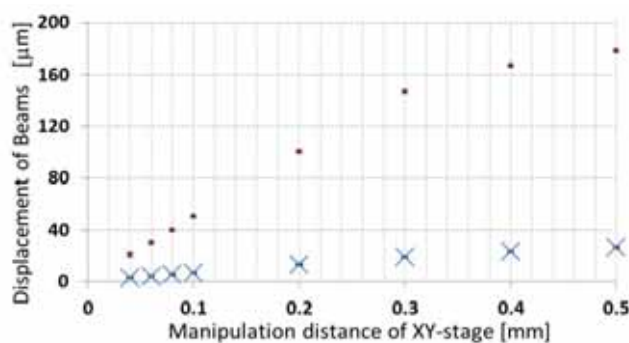


Fig.2 Evaluation of repeatability of developed probe

Tab.1 Experimental result of repetitive accuracy

Stage [ $\mu\text{m}$ ]		40	60	80	100	200	300	400	500
Manipulation point [ $\mu\text{m}$ ]	AVE	2.68	3.89	5.23	6.56	13.24	19.03	23.21	26.22
	STD	0.18	0.14	0.12	0.10	0.10	0.10	0.10	0.12
Actuation point [ $\mu\text{m}$ ]	AVE	20.8	30.0	39.8	50.8	100.3	147.0	166.9	178.1
	STD	1.96	1.19	1.09	1.14	1.32	1.47	1.12	1.23
Reduction rate		7.76	7.72	7.61	7.74	7.58	7.73	7.19	6.79

## Biography

Keitaro Ito is a Bachelor student in the Mechanical and Aerospace Engineering, Nagoya University.

# Noncontact Nanometric Positioning of Probe Tip for Measurement of Mechanical Parameters of Cell



Keitaro Ito<sup>1</sup>, Shinya Sakuma<sup>1</sup>, and Fumihito Arai<sup>1,2</sup>  
<sup>1</sup>Nagoya University, JAPAN, and <sup>2</sup>Seoul National University, KOREA

For the high speed and continues measurement of mechanical properties of the cell

## 1. Background : Mechanical parameter sensing of specific cells

Sasata et al. 100 μm  
Wang et al. 40 μm

**AFM**  
 Power : nN order  
 Resolution : Å order  
 Target : Adhered cell

**Optical tweezers**  
 Power : pN order  
 Resolution : nm order  
 Target : Floating cell

**Magnetic actuator**  
 Power : mN order  
 Resolution : μm order  
 Target : Floating cell

**Actuation Manipulation Point**

(a) Previous: Displacement of Manipulation Point vs Displacement of Actuation Point shows a large step.

(b) Proposed: Displacement of Manipulation Point vs Displacement of Actuation Point shows a much smaller step, indicating **Improvement of positioning accuracy** from μm order to nm order.

**Reduction** of the manipulation band.

The important features of the actuation method are the **power** and the **resolution** of manipulation.

**Young's modulus** scale: kPa → μN ~ mN order → Required force  $F = AE\epsilon$  → mN order → GPa

## 2. Concept : Deformation of cell in a flow

**Disposable part**: Force sensor, Cell, On-chip probe

**Sensing part**: Microscope

**Actuation part**: Motorized stage

Mechanical Properties Measurement

- (1) Measurement in a microfluidic chip
- (2) High power and High resolution
- (3) Chip part is disposable

## 3. Analysis of Reduction Mechanism

$l_A = 8.5 \text{ mm}$   
 $l_B = 8.5 \text{ mm}$   
 $l_C = 7.3 \text{ mm}$   
 $b_A = 50 \mu\text{m}$   
 $b_B = 25 \mu\text{m}$   
 $b_C = 25 \mu\text{m}$   
 $R_D = 1/6$

The on-chip probe was designed to 100 μm order cell.

## 4. Fabrication : Layer fabrication

1. Sputtering of Cr and OFPR Spin coating
2. Cr patterning
3. Patterning of SU-8 (1st layer)
4. Patterning of SU-8 (2nd layer)
5. SU-8 Spin coating
6. SU-8 Patterning
7. DRIE
8. Assembling magnet
9. Assembling

Process flow of on-chip probe

Photos of fabricated on-chip probe

Thickness: 10 μm

## 6. Conclusions

We succeeded in non-contact actuation of probe in the microchannel. The performance of the positioning accuracy was examined, we applied this system for on-chip deformation of the cell.

In the future research, the on-chip force sensor will be developed in order to measure the cellular mechanical parameters.

The proposed method will be one of the promising methods to realize high throughput sensing of mechanical parameter of cell. Since the chip part is disposable, our concept is suitable for biomedical application.

## 5. Experiments

Probe tip: Si wall, 40 μm

Oocyte: Displacement : 30 μm

Overall view of experimental setup: Microscope (sensing part), Sample stage, Motorized stage, On-chip probe (disposable part)

Magnetic flux density placed on the motorized stage: 176 mT assembled to the on-chip probe: 140 mT

Deformation of oocyte

Overall view of experimental setup

Displacement of Beams [μm] vs Manipulation distance of XY-stage [mm]

Actuation point

Manipulation point

Repetitive accuracy of the probe tip: STD < 0.18 μm

Repetitive positioning accuracy

Measured cellular force: 10.0 μN

On-chip cellular force measurement

**Acknowledgment:**  
 This work is partially supported by Scientific Research from Ministry of Education, Culture, Sports, Science and Technology (23106002) and the Nagoya University Global COE program for Education and Research of Micro-Nano Mechatronics.



Contact address : Shinya Sakuma (sakuma@biorobotics.mech.nagoya-u.ac.jp)  
 URL: <http://www.biorobotics.mech.nagoya-u.ac.jp/>, TEL: 052-789-5026, FAX : 052-789-5027  
 Department of Micro-Nano Systems Engineering, Graduate School of Engineering  
 Furo-cho, Chikusa-ku, Nagoya 464-8603, JAPAN



# Occupant response in vehicle frontal crash



Takuya ITAKURA

itakura.takuya@e.mbox.nagoya-u.ac.jp

Koji Mizuno

kmizuno@mech.nagoya-u.ac.jp

Graduate School of Engineering, Nagoya University  
Furo-cho, Chikusa-ku, Nagoya 464-8603, JAPAN

## Abstract

In vehicle crashes, a high level of acceleration is applied to the passenger compartment according to car deformation. The high acceleration can induce injuries to occupants. It has been indicated that a shape of crash pulse affects the occupant kinematics. I research the crashworthiness of vehicles with respect to the crash pulse and injury risks to the occupant.

Computer simulations are conducted using LS-DYNA and MADYMO. Vehicle structure, crash dummy, and human finite element (FE) model are used (Fig. 1). The occupant kinematic behavior is examined in the acceleration field. I investigate how the vehicle acceleration shape was generated by the crush of vehicle structures or components. I also compared the crash dummy and the human FE models, and found that the human FE model shows more flexible behavior compared to the crash dummies.

Assuming that the occupant responses as input/output system, a finite impulse response (FIR) was applied (Fig. 2). It was demonstrated that the occupant acceleration can be predicted by the FIR method when vehicle acceleration is provided (Fig. 3). In various conditions of impacts, the FIR was examined. It was shown when the intrusion into the passenger compartment is large or the interaction between the airbag and the occupant body changes due to high severity of impact, it was difficult to predict the occupant response.

The crash pulse was optimized using steepest descent method to minimize the chest acceleration of the crash dummy model. The optimized crash pulse was the high acceleration in the initial phase, small acceleration in the middle phase and again high acceleration in the final phase. The optimized crash pulse was effective for the human FE model (Especially, the chest deflection was very small). This crash pulse can be useful for hyper-minicars that the acceleration level is severe in a crash. I have started to investigate the vehicle structures that can generate the optimum crash pulse for these small cars.



Fig. 1 Finite element model

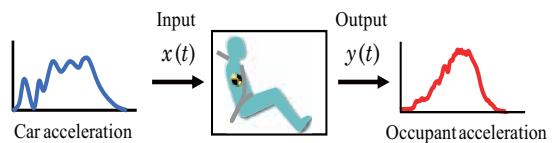


Fig. 2 Occupant response system

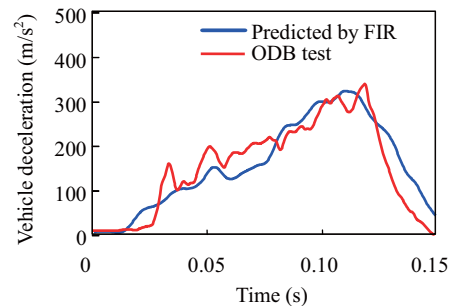


Fig.3 Predicted vehicle acceleration

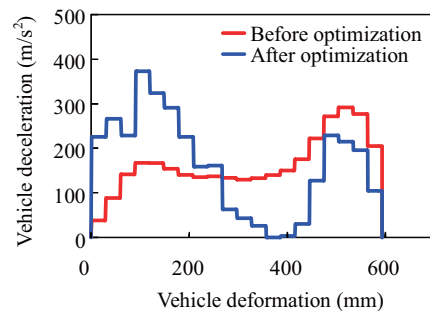


Fig.4 Optimized crash pulse

# Occupant response in vehicle frontal crash

Takuya Itakura Koji Mizuno Nagoya University

## Background

In vehicle crashes, a high level of acceleration is applied to the passenger compartment according to car deformation. I research the crashworthiness of vehicles with respect to the crash pulse and injury risks to the occupant.

Computer simulations are conducted using LS-DYNA and MADYMO. Vehicle structure, crash dummy, and human finite element (FE) models were used (Fig. 1). The occupant kinematic behavior was examined in the acceleration field.



Fig. 1 Finite element model

## Prediction with FIR

Assuming that the occupant responses as input/output system (Fig. 2), a finite impulse response (FIR) method was applied (Fig. 3). The occupant acceleration could be predicted by the FIR (Fig. 4). When the interaction between the airbag and the occupant body changes, the occupant response was difficult to be predicted (Fig. 5).



Fig. 2 Occupant response system

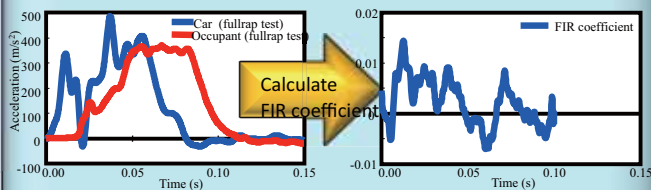


Fig. 3 Calculation of FIR coefficient

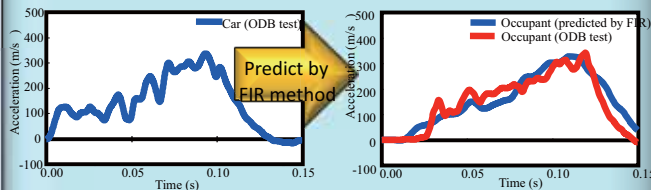


Fig. 4 Prediction of vehicle acceleration



Fig. 5 Cases that FIR cannot predict occupant response

## Vehicle acceleration mechanism

It was investigated that how the vehicle acceleration shape was generated by the crush of vehicle structures or components (Fig. 6).

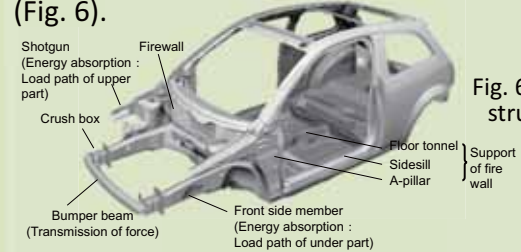


Fig. 6 Vehicle structures

In phase 1 of crash, a force is transmitted by front side members. In phase 2, engine contact force is added, and it is transmitted to the lower part of a firewall (Fig. 7). These forces generate vehicles acceleration.

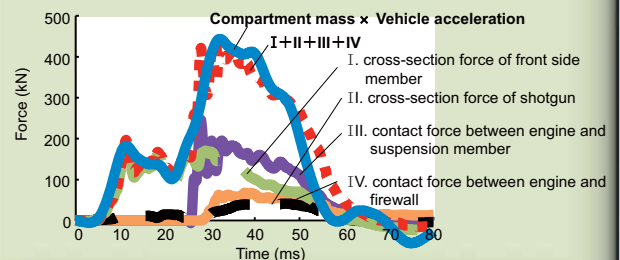


Fig. 7 Vehicle acceleration

## Optimization of crash pulse

The crash pulse was optimized using a steepest descent method (Fig. 8) to minimize the chest acceleration. The optimized crash pulse was the high acceleration in the initial phase, small acceleration in the middle phase and again high acceleration in the final phase (Fig. 9).

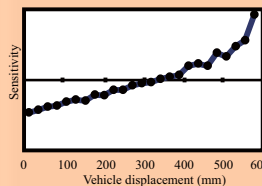


Fig. 8 Sensitivity

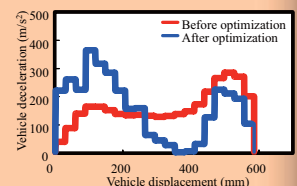


Fig. 9 Optimized crash pulse



Fig. 10 Optimization with dummy model

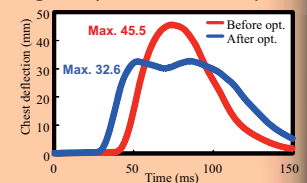
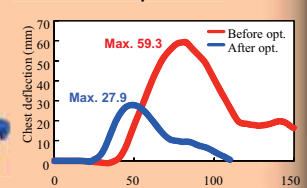


Fig. 11 Optimization with human FE model



# Mechanical properties of carbon nanotubes with one-dimensional intramolecular junction



Yusuke KINOSHITA\*, Motoyuki MURASHIMA\*\*,  
Masaki KAWACHI\*\*\*, Nobutada Ohno\*\*\*\*

\*kinoshita@mech.nagoya-u.ac.jp, \*\*murashima@mml.mech.nagoya-u.ac.jp,  
\*\*\*kawachi@mml.mech.nagoya-u.ac.jp, \*\*\*\*ohno@mech.nagoya-u.ac.jp

Graduate School of Engineering, Nagoya University  
Furo-cho, Chikusa-ku, Nagoya 464-8603, JAPAN

## Abstract

Mechanical properties of single-walled carbon nanotubes with one-dimensional intramolecular junctions (CNT-IMJs) are investigated using first-principles density functional theory calculations (Fig. 1). The influence of Stone-Wales (SW) defects (a pair of five- and seven-membered rings) at a junction on the Young's modulus, tensile strength and breaking strain of the CNT-IMJs are discussed from the charge density and interatomic distance.

Our calculations reveal that deformation concentration on a seven-membered ring causes the decrease in the strength and elongation of the CNT-IMJs (Fig. 2). It is found that the tensile strength and breaking strain of the CNT-IMJs depend on the position of SW defects (Fig. 3), while the number of SW defects hardly affects them. The applicability of AIREBO classical interatomic potential to simulate tensile deformation in the CNT-IMJs is also discussed.

## Biography

Masaki Kawachi received the bachelor degree in mechanical engineering from Nagoya University, in 2010.

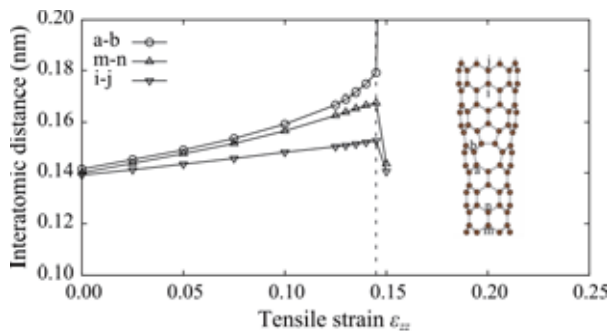


Fig. 2 Interatomic distance of CNT-IMJ-1.

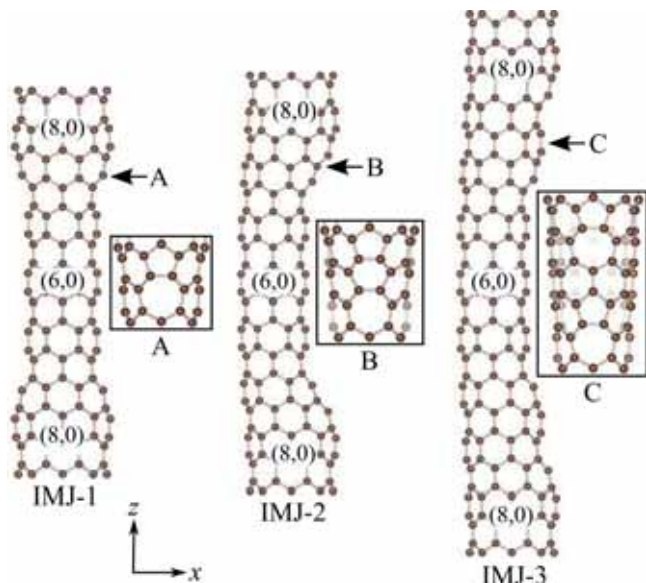


Fig. 1 Simulation models of SWCNT with one-dimensional intramolecular junction (CNT-IMJs).

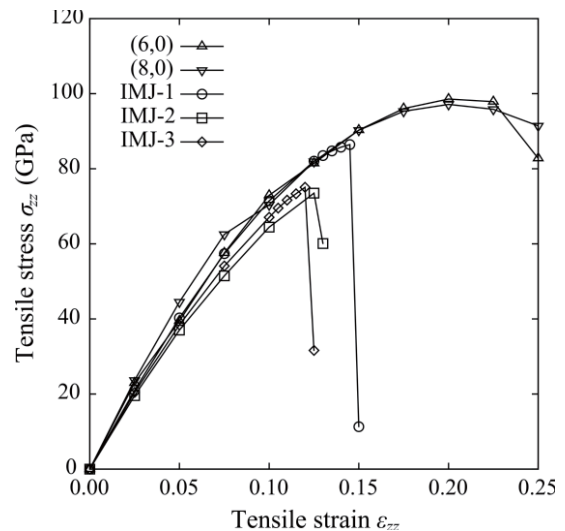


Fig. 3 Tensile stress-strain curves calculated from first-principles.

# Mechanical properties of carbon nanotubes with one-dimensional intramolecular junction

Yusuke KINOSHITA, Motoyuki MURASHIMA, Masaki KAWACHI, Nobutada Ohno

March, 2012

## Introduction

Mechanical properties of single-walled carbon nanotubes with **one-dimensional intramolecular junctions (CNT-IMJs)** are investigated using **first-principles density functional theory calculations**. The influence of Stone-Wales (SW) defects (a pair of five- and seven-membered rings) at a junction on the Young's modulus, tensile strength and breaking strain of the **CNT-IMJs** are discussed from the **charge density** and interatomic distance.

The applicability of **AIREBO classical interatomic potential** to simulate tensile deformation in the **CNT-IMJs** is also discussed.

## Analysis

### Models

- \* Pristine CNT | (6,0), (8,0)
- \* CNT-IMJs | IMJ-1, IMJ-2, IMJ-3 (Fig. 1)

### Analyzed properties

- \* Young's modulus |  $E$
- \* Tensile strength |  $\sigma_B$
- \* Breaking strain |  $\varepsilon_B$
- \* Formation energy |  $E_F$

$$E_F = [E^{IMJ} - (e^{(6,0)} \times N^{(6,0)} + e^{(8,0)} \times N^{(8,0)})] / N^{IMJ}$$

$N^{IMJ}$ ,  $E^{IMJ}$  | The number of atoms and energy of CNT-IMJ  
 $e^{(6,0)}$ ,  $e^{(8,0)}$  | Energy per atom of each pristine CNT  
 $N^{(6,0)}$ ,  $N^{(8,0)}$  | The number of atoms of each pristine CNT

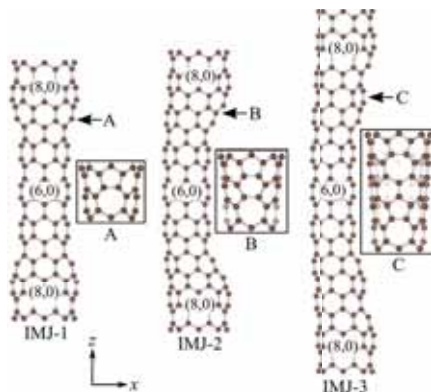


Fig. 1 Simulation models of SWCNT with one-dimensional intramolecular junction (CNT-IMJs).

## Conclusion

Our calculations revealed that deformation concentration on a seven-membered ring **causes the decrease in the strength and elongation of the CNT-IMJs**.

It was found that the tensile strength and breaking strain of the **CNT-IMJs depend on the position of SW defects**, while the **number of SW defects hardly affects them**.

## Results

### First principle calculation

Table 1 Formation energy  $E_F$ , Young's modulus  $E$ , tensile strength  $\sigma_B$  and breaking strain  $\varepsilon_B$  of (6,0) and (8,0) pristine CNTs and CNT-IMJs calculated from first-principles.

	$E_F$ (eV/atom)	$E$ (GPa)	$\sigma_B$ (GPa)	$\varepsilon_B$
(6,0)		1046	98.6	0.200
(8,0)		1004	97.2	0.200
IMJ-1	0.033	874	86.4	0.145
IMJ-2	0.022	825	73.5	0.125
IMJ-3	0.021	865	75.1	0.120

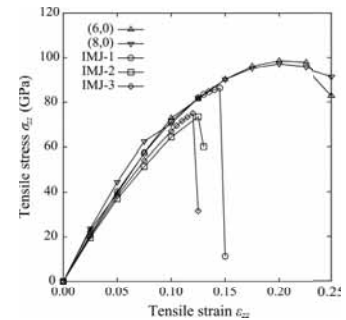


Fig. 2 Tensile stress-strain curves calculated from first-principles.

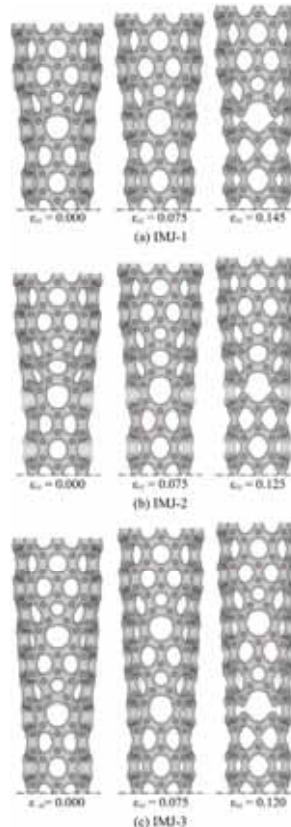
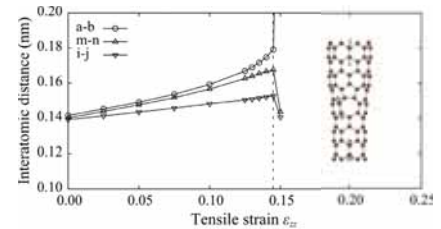
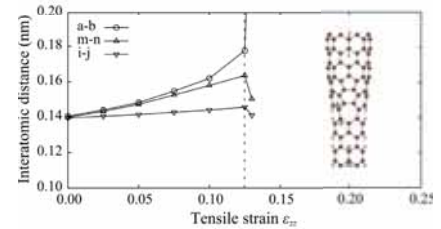


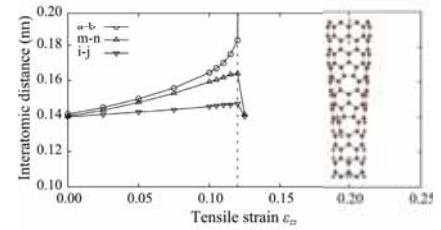
Fig. 3 Charge density of CNT-IMJs.



(a) IMJ-1



(b) IMJ-2



(c) IMJ-3

Fig. 4 Interatomic distance of CNT-IMJs

### Molecular dynamics (AIREBO)

Table 2 Formation energy  $E_F$  and Young's modulus  $E$  of (6,0) and (8,0) pristine CNTs and CNT-IMJs calculated from AIREBO potential.

	$E_F$ (eV/atom)	$E$ (GPa)
(6,0)		1048
(8,0)		1066
IMJ-1	0.042	988
IMJ-2	0.025	974
IMJ-3	0.027	1011

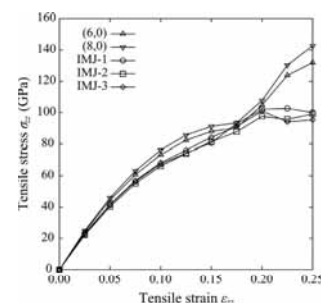


Fig. 5 Tensile stress-strain curves calculated from AIREBO potential.

# Road detection system outdoor -Image recognition with Improved Flood Fill-



Yu MAEDA

maeda@robo.mein.nagoya-u.ac.jp

Kosuke Sekiyama

sekiyama@robo.mein.nagoya-u.ac.jp

Toshio Fukuda

fukuda@robo.mein.nagoya-u.ac.jp

Graduate School of Engineering, Nagoya University  
Furo-cho, Chikusa-ku, Nagoya 464-8603, JAPAN

## Abstract

In order for cars to safely run in an unpaved environment, such as paddy field, mountain with steep slopes and many objects on the ground, we propose an image recognition method for movable region on unpaved roads. It is based on Flood Fill method integrated with color information.

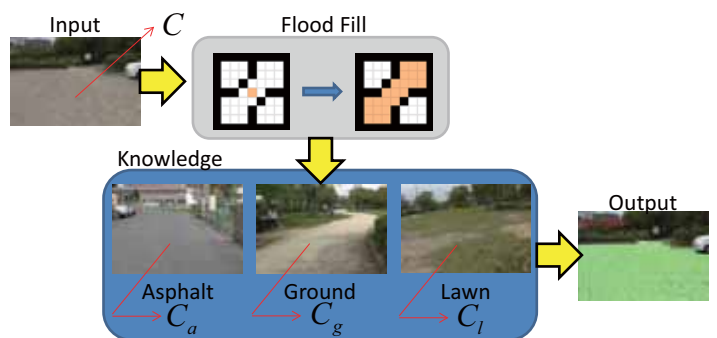
Flood Fill is a segmentation method to paint connected seed points like a bucket fill tool of bit map paint. We applied Flood Fill to video input images. During the process, it gets the mean colors of each region, and selects all the regions which are similar to the biggest region's color in the bottom quarter of the input image. Then, it calculates the color distances of the input and three types and selects a type of the minimum distance. It enables the vehicle to find which road type it is on. Furthermore, we use hysteresis of previous frames to recognize those roads more precisely.

We have already achieved a high degree of accuracy for recognition of paved and unpaved roads. It is efficient in comparison to other road detection methods which have ever been done.

In the future, we will focus on expecting the slippery probability of roads from road type and movability of the differences in level and slopes.

## Biography

Yu Maeda received the Bachelor degree in Mechanical Engineering from Nagoya University in 2011, and a master course student in Mechanical Science & Engineering of graduate school of Nagoya University. He is focusing on the studies of road detection.



Color distance

$$d_m = \sqrt{(C_R - C_{m_r})^2 + (C_G - C_{m_g})^2 + (C_B - C_{m_b})^2}$$

$m = a, g, l$

Asphalt  
 $C_a = (C_{a_r}, C_{a_g}, C_{a_b})$   
 $d_a$

Ground  
 $C_g = (C_{g_r}, C_{g_g}, C_{g_b})$   
 $d_g$

Lawn  
 $C_l = (C_{l_r}, C_{l_g}, C_{l_b})$   
 $d_l$

$C = (C_R, C_G, C_B)$

$\min(d_a, d_g, d_l) \rightarrow \text{Road type}$



Results of our method

# Road detection system outdoor -Image recognition with Improved Flood Fill-

Yu Maeda, Kosuke Sekiyama and Toshio Fukuda, Nagoya University March, 2012

## PURPOSE

In order for cars to safely run in an unpaved environment, such as paddy field, mountain with steep slopes and many objects on the ground, we propose an image recognition method for movable region on unpaved roads. It is based on Flood Fill method integrated with color information.



Fig. 1 Target environment

- There is no mountain maps in a high degree of accuracy.
- Kong et al. couldn't decide a road color due to the coverage of sand and snow → Vanishing point → Not so good (Fig. 2)
- Road → Asphalt, ground or lawn?



Fig. 2 Kong et al. (2009)

## EXPERIMENT

Flood Fill is a segmentation method to paint connected seed points like a bucket fill tool of bit map paint. We applied Flood Fill to video images (Panasonic SDR-100). During the process, it gets the mean colors of each region, and selects all the regions which are similar to the biggest region's color in the bottom quarter of the input image. Then, it calculates the color distances of the input and three types and selects a type of the minimum distance. It enables the vehicle to find which road type it is on. Furthermore, we use hysteresis of previous frames (5 and 10 frames before) to recognize those roads more precisely.

Decision of the same region

$$src(x', y')_c - Dif f \leq src(x, y)_c \leq src(x', y')_c + Dif f$$

$$c = R, G, B$$

Decision of road

$$|C_H - C_{i_H}| \leq Thresh\_H$$

$$|C_S - C_{i_S}| \leq Thresh\_S$$

$$|C_V - C_{i_V}| \leq Thresh\_V$$

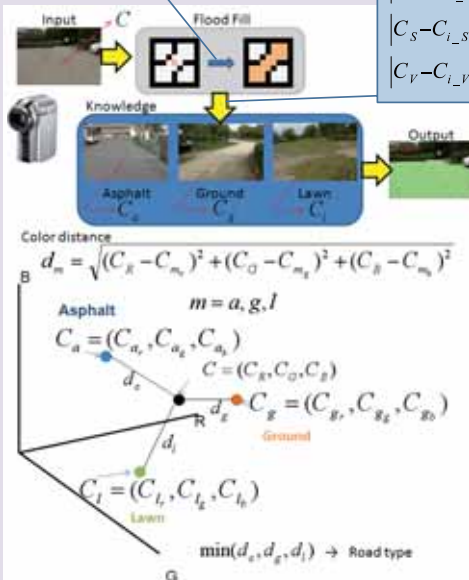


Fig. 3 Process of our method

## RESULTS



Fig. 4 Results of 10 scenes. Input image (left) and result image (right)

Our method, even it uses only camera information, can detect roads as the same as Alvarez Method 2. It takes 583 msec (C++, Core(TM)2 Quad CPU Q8200 @ 2.33 GHz) and 145 msec when we ignore the regions smaller than 5/1000. Alvarez et al.'s took about 735 msec (Matlab, Pentium-4 CPU @ 2.8 GHz).

TABLE I. CONSISTENCY TABLE

Consistency table	Ground-truth	
	Road	Non-road
Result	Road	TP
	FP	FN
	Non-road	TN

TABLE II. DEFINITION OF EVALUATIVE VALUES

Pixel-wise measure	Definition
Quality	Q=TP/(TP+FP+FN)
Detection rate	DR=TP/(TP+FP)
Detection accuracy	DA=TP/(TP+FN)
Effectiveness	F=2*DA*DR/(DA+DR)

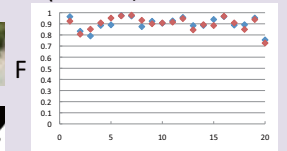
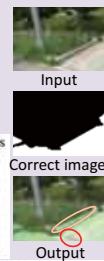


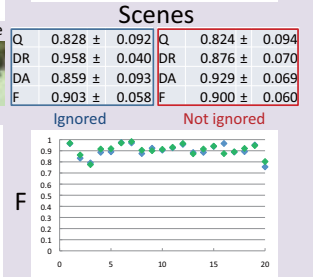
TABLE III. COMPARISON OF RESULTS

Pixel-wise measure	Complete database		
	Improved Flood Fill <sup>a</sup>	Alvarez: Method <sup>1</sup>	Alvarez: Method <sup>2</sup>
Q	0.84±0.08	0.68±0.16	0.84±0.23
DR	0.91±0.07	0.57±0.14	0.87±0.30
DA	0.91±0.05	0.69±0.10	0.90±0.22
F	0.91±0.05	0.63±0.10	0.86±0.25

a. Our method with superimposition and with ignorance of small regions. b. Results of using only HSV color information. c. The highest performances of them, it was integrated 3D cues and other much information.



Fig. 5 Alvarez et al. (2010)



Pixel-wise measure	Ignored		Not ignored	
	Q	DR	DA	F
Q	0.828 ± 0.092	0.824 ± 0.094	0.958 ± 0.040	0.876 ± 0.070
DR	0.859 ± 0.093	0.929 ± 0.069	0.903 ± 0.058	0.900 ± 0.060

Fig. 6 Comparison of ignored/not ignored and single/superimposed image

## CONCLUSION

We proposed a new road detection method using Flood Fill and it detected in a high degree of accuracy in comparison to the method with 3D information. In the future, we will construct a new algorithm for mountain exploration to expect the slippery probability of roads from road type information and calculate the movability of the differences in level and slopes. Moreover, we will challenge more complicated road detection with the variety of weathers.

# Parylene Based Catheter Type Flow Sensor for Detecting Breathing Characteristics



Yudai YAMAZAKI  
yamazaki.yudai@g.mbox.nagoya-u.ac.jp

Mitsuhiro SHIKIDA  
shikida@mech.nagoya-u.ac.jp

Kazuo SATO

sato@mech.nagoya-u.ac.jp

Dept. of Micro-nano Systems Eng., Nagoya University  
Furo-cho, Chikusa-ku, Nagoya 464-8603, JAPAN

## Abstract

The number of cases of chronic obstructive pulmonary disease (COPD), an adult disease, is increasing rapidly. Spirometry is normally used to evaluate the state of this disease.(Fig. 1) It measures the flow at the human mouth. However, the lesions are caused at the ends of diverging bronchi.

We proposed a catheter type thermal flow sensor to evaluate breathing characteristics in small bronchus by means of MEMS technologies. The schematic view of the sensor is shown in Fig. 2. The sensor was suitable for the reciprocating flow measurement and using in vivo.

This sensor was fabricated with biocompatible materials, and parylene was used as a sensor substrate because this sensor was used in vivo. A metal heater working as a flow velocity sensor was formed on the thin parylene film. Hot-wire anemometry sensing was chosen because the flow rate could be measured over a wide range and it had simple structure. However, the signal output of the thermal flow sensor depends on gas temperature. To compensate the flow rate by the temperature change, we integrated the temperature sensing function onto the sensor. It increased the accuracy of the sensor.

The animal experimental setup was shown in Fig.3. We confirmed that this sensor could detect the breathing characteristics at the air passage in mice.



Fig. 1 Measurement by a spirometry

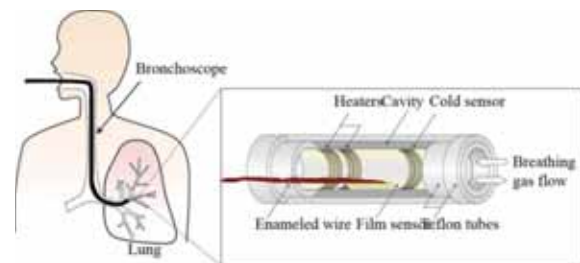


Fig. 2 Schematic view of the sensor

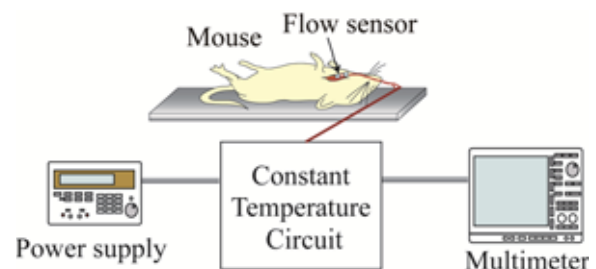


Fig. 3 Detecting the breathing characteristics of mice

## Biography

Yudai Yamazaki received the Bachelor degree in Engineering from Nagoya University in 2011. He is currently a Master course student in Nagoya University, focusing on MEMS technology.



# Parylene Based Catheter Type Flow Sensor for Detecting Breathing Characteristics

Yudai Yamazaki<sup>1</sup>, Mitsuhiro Shikida<sup>2</sup>, and Kazuo Satō<sup>3</sup>

<sup>1</sup>Dept. of Micro-nano Systems Engineering, Nagoya University, Nagoya, Japan

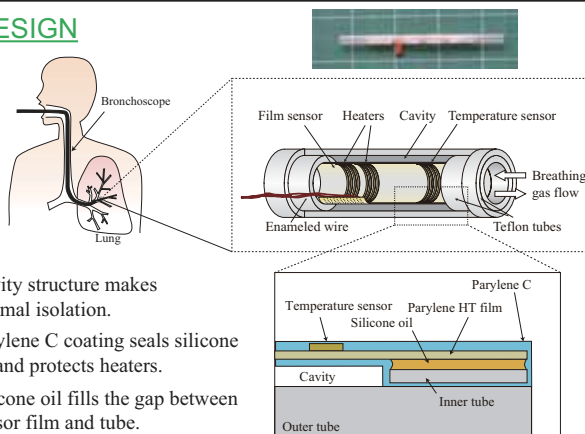
<sup>2</sup>Center for Micro-Nano Mechatronics, Nagoya University, Nagoya, Japan

<sup>3</sup>Dept. of Micro-Nano Systems Engineering, Nagoya University, Nagoya, Japan

## ABSTRACT

We proposed a catheter thermal flow sensor to evaluate breathing characteristics in small bronchus by means of MEMS technologies. We used biocompatible parylene HT film as a substrate, and we protected the heater element with parylene C. Hot-wire anemometry sensing was chosen because it had simple structure. However, the sensor output depends on gas temperature. To compensate the flow rate value by the temperature change, we integrated the temperature sensing function onto the flow sensor. We succeeded in evaluating breathing characteristics at the air passage in mice.

## DESIGN



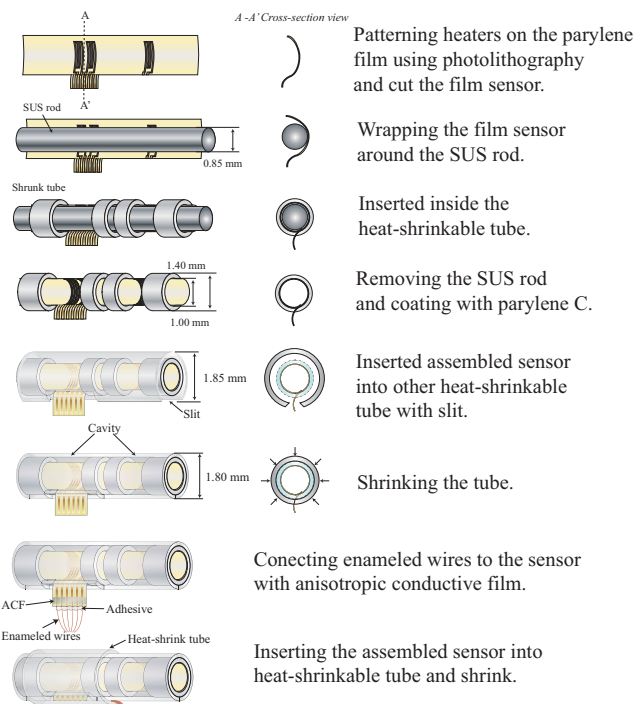
Cavity structure makes thermal isolation.

Parylene C coating seals silicone oil and protects heaters.

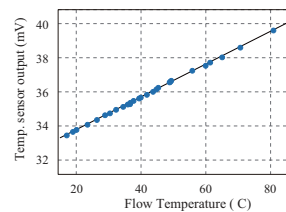
Silicone oil fills the gap between sensor film and tube.

Schematic view of the parylene HT based catheter type flow sensor integrated the temperature sensing function.

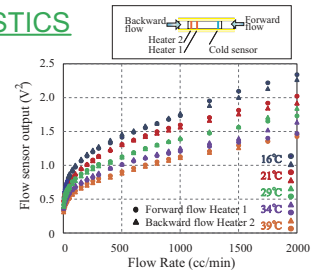
## FABRICATION



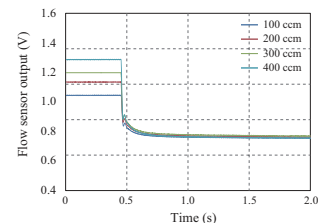
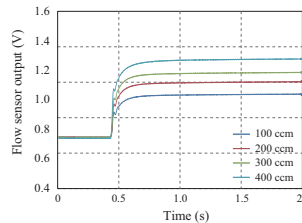
## SENSOR CHARACTERISTICS



Relationship between flow temperature and sensor output.

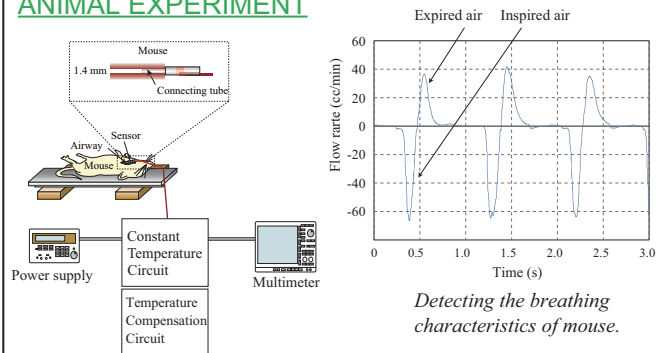


Relationship between flow rate and flow sensor output at different temperature conditions.



Short time 90 % response time of 145 and 147 ms.

## ANIMAL EXPERIMENT



Schematic view of animal experimental setup.

Confirmed the sensor could real-time measurement of the breathing characteristics.

# EHL Analysis of CMP Process by Using ALE Finite Element Method



**Masakazu ASABA**

Graduate School of Engineering, Nagoya University

**Norikazu SUZUKI**

nsuzuki@mech.nagoya-u.ac.jp

**Yohei HASHIMOTO**

hashimo1982@yahoo.co.jp

Furo-cho, Chikusa-ku, Nagoya 464-8603, JAPAN

[asaba@upr.mech.nagoya-u.ac.jp](mailto:asaba@upr.mech.nagoya-u.ac.jp)

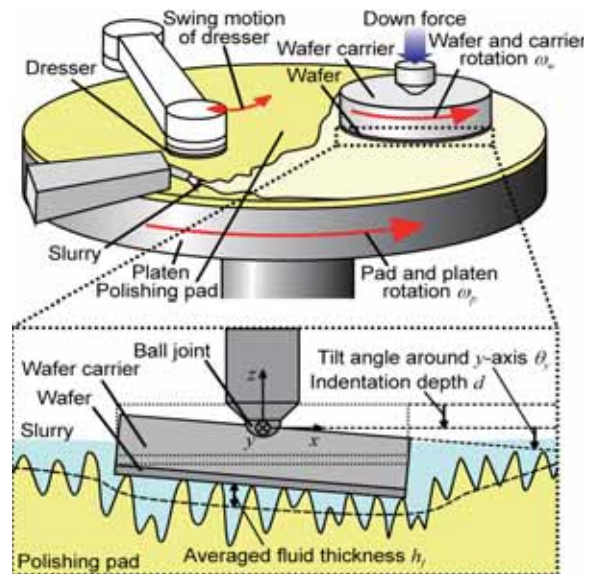
## Abstract

A dynamic structure analysis model of Chemical Mechanical Polishing (CMP) process is developed by utilizing a finite element method (FEM) in the present study. By considering relative motion of a wafer and a polishing pad in a steady-state process, a nonlinear equation of motion is derived based on Arbitrary Lagrangian-Eulerian (ALE) method in the proposed model.

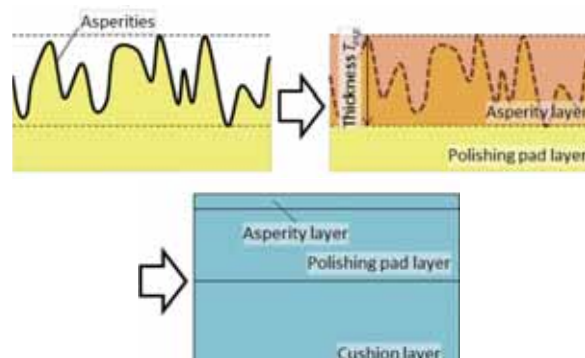
Since the dynamic CMP process in the steady-state can be treated as a static problem in an ALE coordinate system, practical large scale problems can be solved accurately with consideration of the dynamic structural behavior. In order to consider the effect of the nonlinear elastic deformation of the polishing pad due to micro asperity contact, nonlinear elasticity of the pad surface asperity layer is also formulated.

The dynamic structural analyses considering the nonlinear viscoelastic characteristics of the polishing pad were carried out by applying the proposed model.

Analytical results indicate that stress concentration beneath the leading edge of the wafer greatly depends on the viscoelasticity of the polishing pad, i.e., the consideration of dynamic viscoelastic behavior of the polishing pad is significantly important to predict the polishing pressure distribution especially around the wafer edge area.



Schematic illustration of CMP Process



## Biography

Masakazu Asaba received the Bachelor degree in Engineering from Nagoya University. I am currently first-year master in Nagoya University, focusing on the studies of CMP process analysis. I'm interested in precision technology.

# EHL Analysis of CMP Process by Using ALE Finite Element Method

M. Asaba, N. Suzuki, Y. Hashimoto  
 Graduate School of Engineering, Nagoya University, Japan, asaba@upr.mech.nagoya-u.ac.jp

## 1. Introduction

Material removal rate in CMP process strongly depends on polishing pressure. Thus, analytical prediction of polishing pressure distribution, which can be utilized to facilitate understanding of the influence of the process parameters and/or mechanical configurations of polishing head on the polishing pressure distribution, is a major focus of research in CMP technology.

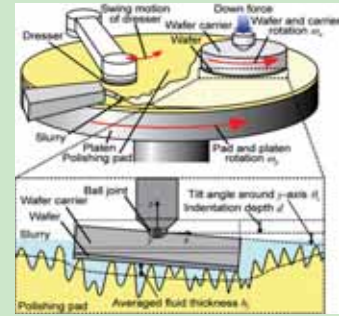
- ✓ A number of EHL analysis models of CMP process have been proposed to predict stress distribution.
- ✓ However, it is still difficult to predict stress distribution containing wafer edge area in structural analysis!!  
 (Most analysis models utilizes "Winkler foundation model" or "elastostatic FE analysis model".)

➡ Simultaneous consideration of "nonlinear asperity contact" and "viscosity of the pad" in FEM

A novel structure analysis model using finite element method is proposed

- Nonlinear asperity contact → Nonlinear elasticity based on Greenwood-Williamson model (G-W model)
- Viscosity of the pad → Dynamic structure analysis based on Arbitrary Lagrangian-Eulerian (ALE) method (ICPT2010)

Suzuki et al.)

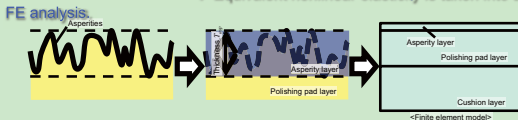


[Schematic illustration of CMP Process]

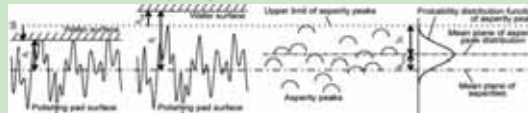
## 2. Nonlinear asperity contact model and ALE (Arbitrary Lagrangian-Eulerian) analysis model

- ✓ A surface of a polishing pad is filled with asperities due to conditioning.
- ✓ The pad surface asperity layer deforms in a nonlinear manner by contacting with a wafer surface.

➡ Equivalent nonlinear elasticity is taken into account in



□ Nonlinear asperity contact model



**Simple stochastic model (Greenwood-Williamson model) is applied.**  
 The pad surface is filled with hemispherical asperities with same radius.  
 The asperity height distributes based on the height probability function  $\psi(z)$ .

$$\sigma = \int_0^{\Delta h} G(\Delta h - z)^2 \psi(z) dz \quad G = \frac{4}{3} \frac{E_{asp}}{1 - \nu_{asp}^2} \sqrt{R_{asp}} \quad \psi(z) = \frac{1}{\sqrt{2\pi}} e^{-\frac{z^2}{2\sigma_{asp}^2}}$$

$$E_{elastic} = \frac{\int_0^{\Delta h} G(\Delta h - z)^2 \psi(z) dz}{|x_{asp}|}$$



- ✓ Dynamic analysis using time-history response method is not feasible due to huge amounts of time required for the computation.
- ✓ Stress distribution at the wafer-pad interface is supposed to be constant in a steady-state.

➡ Motion equation in a steady-state is formulated using

ALE method:

□ Structure analysis by using ALE method

Finite element mesh is generated to the wafer and the pad with ignoring rotation motions.  
 → Relative mesh positions in a steady-state do not change in the ALE coordinate system.

ALE coordinate system:  $(X_1, X_2)$

$$\#(X_1, X_2) = \frac{\partial u}{\partial x} + \frac{\partial v}{\partial x_2} + \frac{\partial w}{\partial x_2} + \frac{\partial w}{\partial x_1}$$

In a steady-state:  $\#(X_1, X_2) = \frac{\partial u}{\partial x_1}$

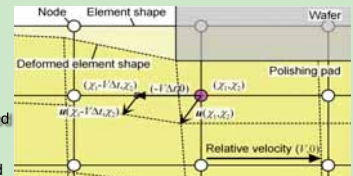
➡ "Time derivative" can be derived from "space derivative"

Displacement vector can be derived from following simple equation;

$$[C](\dot{u}) + [K](u) = ([C](\dot{D}) + [K](D))u = (f_{residual} + U_{constraint}) + (f_{load})$$

[D]: Space derivative matrix

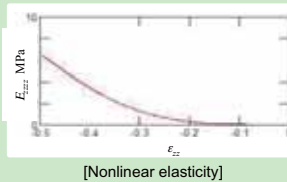
Based on an ALE coordinate system, dynamic CMP process in a steady-state can be treated as a static problem



- ✓ Based on ALE coordinate system → can be treated like a static analysis → time-saving without iteration
- ✓ Stationary relative position → simple meshing procedure

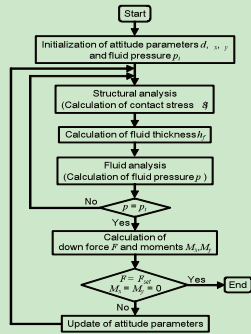
## 3. Influence of asperity contact and viscosity of polishing pad on contact stress distribution

Contact stress analyses are conducted under different parameters by using developed analysis. Proposed contact stress analysis was applied to **soft EHL analysis**. After the structural analysis, thin slurry film thickness is calculated based on contact stress distribution, and then, the fluid analysis is carried out to calculate fluid pressure distribution. From the calculated contact stress and fluid stress, the total reacting force and the moments along the x-axis and y-axis are calculated and compared with initial conditions. By iteratively updating the initial attitude parameters, equilibrium conditions satisfying the down force and the moment balances can be identified. The rotation speeds of the pad and the wafer were set to be 115 min<sup>-1</sup>. The down force was set to be 130 N.



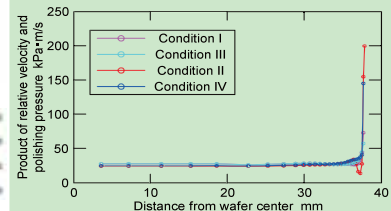
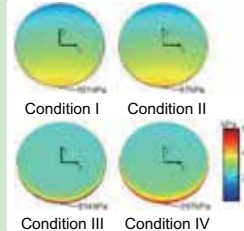
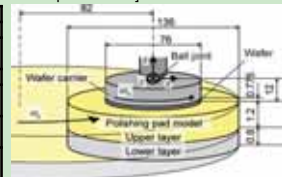
[Nonlinear elasticity]

- [Assumed asperity parameters]
- Asperity density  $\gamma$ : 100 mm<sup>-2</sup>
- Asperity radius  $R_{asp}$ : 50  $\mu$ m
- RMS value of pad surface  $s$ : 6  $\mu$ m
- Young's Modulus of asperity  $E_{asp}$ : 100 MPa
- Poisson's ratio of asperity  $\nu_{asp}$ : 0.3
- Distance btw mean planes of asperity layer and asperity peak distribution  $h_{asp}$ : 9  $\mu$ m
- Asperity layer thickness  $T_{asp} = 2(h_{asp} + 3s) = 52 \mu$ m



[Analytical conditions and identified attitude parameters]

Condition		I	II	III	IV
Proportional damping factor of polishing pad	Upper layer	0	0	0.001	0.001
	Lower layer	0	0	0.01	0.01
Thickness of asperity layer $\mu$ m		-	52	-	52
Indentation depth $\mu$ m		11.2	19.8	10.0	18.5
Identified attitude parameters	Tilt angle around x-axis mdeg	7.0	8.4	0.9	1.8
	Tilt angle around y-axis mdeg	0	0	-0.3	-0.3



[Calculated contact stress distributions and product of relative velocity and polishing pressure]

- ✓ A consideration of the **nonlinear elasticity** due to the asperity contact causes the **decrease** of the edge stress concentration.
- ✓ A consideration of the **viscosity** of the pad causes the **increase** of the edge stress concentration.

➡ The contact stress distribution changes significantly depending on the consideration of the "nonlinear elasticity" and the "dynamic behavior".

## 4. Conclusion

Nonlinear elasticity of the surface asperity layer of the polishing pad is formulated based on G-W micro contact model and applied to ALE finite element analysis to calculate contact stress distribution in the CMP process. From the analytical investigations, it was clarified that the contact stress distribution changes depending on both the nonlinear elasticity and the viscosity of the polishing pad. Especially, the stress concentration around leading edge of the wafer greatly changes. The fluid pressure distribution was also affected due to a change of stress distribution. And thus, **simultaneous considerations of "the nonlinear elasticity" and "the viscosity of the polishing pad" are essential to predict the contact stress distribution especially around the wafer edge area.**

# Study on Tool Damage in High-speed Ceramic Milling of Superalloys



R. Enmei<sup>\*1</sup>, N. Suzuki<sup>\*1</sup>, J. Eto<sup>\*1,\*2</sup>, E. Shamoto<sup>\*1</sup>  
 H. Yoshida<sup>\*2</sup>, R. Shibata<sup>\*2</sup> and Y. Hasegawa<sup>\*2</sup>

<sup>\*1</sup> Graduate School of Engineering, Nagoya University  
 Furo-cho, Chikusa-ku, Nagoya 464-8603, JAPAN

[enmei@upr.mech.nagoya-u.ac.jp](mailto:enmei@upr.mech.nagoya-u.ac.jp)

<sup>\*2</sup> Nagoya Guidance & Propulsion Systems Works,  
 Mitsubishi Heavy Industries, Ltd.

## Abstract

Nickel based superalloy Inconel 718 is beginning to be widely used in aerospace industries. Inconel 718 is also well-known as difficult-to-cut materials due to its high cutting resistance, high temperature-strength and work hardening. High speed milling with SiAlON ceramic tip can attain highly-efficient machining of this material with respect to the conventional tungsten carbide machining. However, the tool life of SiAlON ceramic tip is extremely short due to excessive tool damage with severe boundary wear and unexpected breakage. Although the dynamics of the mechanical structures is suspected to affect the tool life significantly in the ceramic milling, the impact of less dynamic stiffness on the tool damage is not clarified well. Tool damage progress mechanism in ceramic milling of Inconel 718 is experimentally investigated focusing on the influence of the dynamics of the mechanical structures.

A series of cutting tests were conducted and the influence of the dynamics of the mechanical structures on the tool damage was examined. The workpiece fixture was developed and applied to the experimental investigations (see Fig. 1). Its dynamic stiffness and natural frequency in the vertical direction can be changed simultaneously by adjusting the work stage thickness and width. Maximum compliances and natural frequencies are summarized in Table 1.

From the experimental results, the tool wear in the flank face makes progress easily as the stiffness decreases, as shown in Fig. 2. It was confirmed that higher dynamic stiffness in the vertical direction is advantageous to prevent tool damages. In order to clarify the mechanism of the tool damage progress, further investigations on the tool wear mechanism are conducted, which are presented on the POSTER.

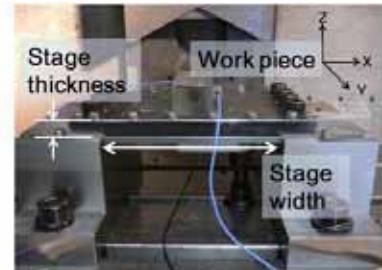


Fig.1 Experimental setup with developed workpiece fixture

Table 1 Stage size and vertical compliance

Settings	Stage size, mm		$G_{-1st}$ bending mode	
	Thickness	Width	Compliance, $\mu\text{m/N}$	Frequency, Hz
A-low	5	135	1.64	977
B-low	8	170	0.90	993
B-high	5	96	0.97	1580
C-low	15	230	0.30	982
C-high	8	119	0.24	1663
D-high	15	155	0.06	1813
H	-	-	0.01	133

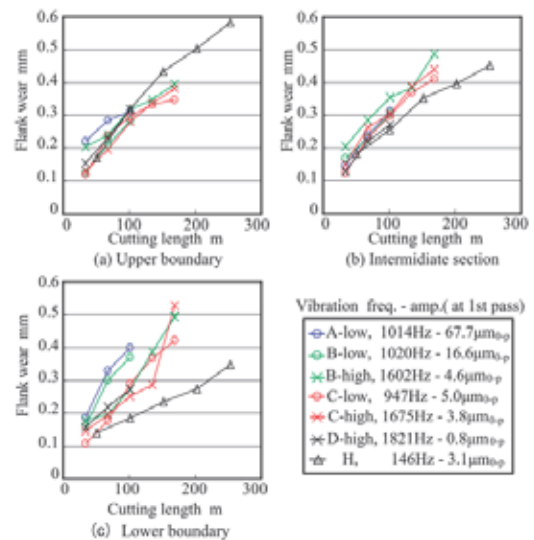


Fig.2 Cumulative cutting length v.s. flank wear width

## Biography

I, Risa EMMEI, received the Bachelor degree in Engineering from Nagoya University. I am currently focusing on the studies of manufacturing technology as a first-year master in Nagoya University. I play the Cello in the Orchestra club.

# Study on Tool Damage in High-speed Ceramic Milling of Superalloys

R. Enmei, N. Suzuki, J. Eto, E. Shamoto, H. Yoshida, R. Shibata and Y. Hasegawa

Graduate School of Engineering, Nagoya University, Japan, [enmei@upr.mech.nagoya-u.ac.jp](mailto:enmei@upr.mech.nagoya-u.ac.jp)  
Nagoya Guidance & Propulsion Systems Works, Mitsubishi Heavy Industries, Ltd.

## 1. Introduction

Nickel based superalloy **Inconel 718** is beginning to be widely used in aerospace industries. Inconel 718 is also well-known as **Difficult-to Cut materials** due to its high cutting resistance, high temperature-strength and work hardening. **High speed milling with SiAlON ceramic tip** can attain highly-efficient machining of this material with respect to conventional tungsten carbide machining. However, the tool life of SiAlON ceramic tip is extremely short due to excessive tool damage with severe boundary wear and unexpected breakage. Although the **dynamics** of the mechanical structures is suspected to affect the tool life significantly in the ceramic milling, the tool damage mechanism is not clarified well.



Jet engine

**Tool damage mechanism in ceramic milling of Inconel 718 is experimentally investigated focusing on the influence of the dynamics of the mechanical structures.**



High speed ceramic milling

- Experimental investigation
  - The workpiece fixture, whose dynamic stiffness and natural frequency can be adjusted simultaneously, was developed and applied to a series of fundamental tool life tests.
- Wear mechanism evaluation
  - The tool damage mechanism was investigated through cutting edge shape measurements.

## 2. Relationship between dynamic stiffness and tool damage

### □ Experimental investigation

- ✓ The special workpiece fixture was developed.
- ✓ Its dynamic stiffness and natural frequency in vertical direction can be changed by adjusting work stage thickness and width.
- ✓ Influence of the dynamics on tool damage is investigated.

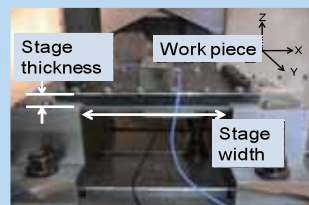


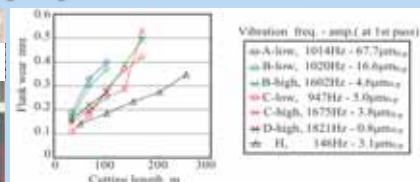
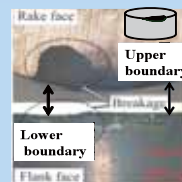
Table Dynamics of designed stage

Settings	Stage size, mm		G <sub>1</sub> -1st bending mode	
	Thickness	Width	Compliance, μm/N	Frequency, Hz
A-low	5	135	1.64	977
B-low	8	170	0.90	993
B-high	5	96	0.97	1580
C-low	15	230	0.30	982
C-high	8	119	0.24	1663
D-high	15	155	0.06	1813
H	-	-	0.01	133

Table Experimental conditions

Cutting speed	700 m/min
Feed rate, $f_t$	0.08, 0.15 mm/tooth
Axial depth of cut	1.0 mm

### □ Cumulative cutting length v.s. flank wear



C-high Tool damage after cutting distance of 169 m ( $f_t$ : 0.15 mm/tooth)

Cutting length v.s. flank wear width ( $f_t$ : 0.15 mm/tooth)

- ✓ Flank wear grows progressively larger, resulting in **breakage** on the Rake face.
- ✓ **Higher dynamic stiffness** of the mechanical structure is **advantageous** to prevent flank wear and breakage.
- ✓ Chatter vibration occurs when milling with the low dynamic stiffness structures **A-low** and **B-low**, resulting in short tool life.

**Dynamic stiffness of the mechanical structure significantly affects the flank wear amount and breakage.**

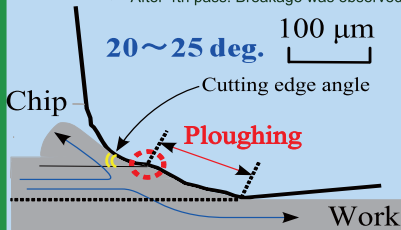
## 3. Estimation of tool wear mechanism

### □ Transition of cutting edge shape

A confocal laser microscope was utilized to measure the cutting edge shape before/after each pass, and the transition of the cutting edge shape was investigated.

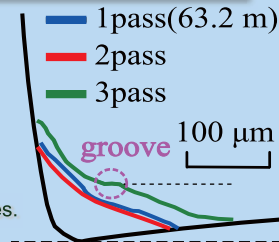
The cutting edge shape gradually deteriorates as the cumulative cutting distance increases.

- ✓ After 1st pass, 2 pass: Tool wear progresses and the cutting edge becomes chamfered.
- ✓ After 3rd pass: A specific groove is formed at the center of the chamfered cutting edge.
- ✓ After 4th pass: Breakage was observed.



Generally, cutting process is involved with material removal as a chip flow and **ploughing**. The boundary of the chip flow and the **ploughing** flow on the cutting edge is known as the "stagnation point". The tensile stress generates at the stagnation point since the material flows are separated in the opposite directions.

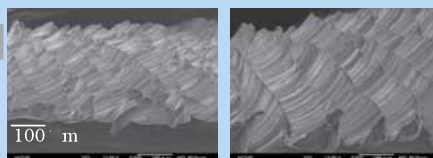
The groove observed on the cutting edge after the 3<sup>rd</sup> pass is considered to be corresponding to the stagnation point. And it is estimated that a crack propagated from this groove, resulting in the breakage while milling at the 4<sup>th</sup> pass.



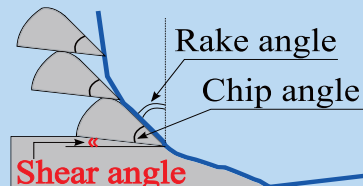
Measured Cross sections of cutting edges at D-high ( $f_t$ : 0.08 mm/tooth, Breakage generated at 224 m)

### □ Chip generation process

"Shear-type chip" was observed by using SEM. From the measured geometry of the chip and the cutting edge, a cutting process with extremely small shear angle was estimated.



SEM image of sampled chip (L)  $f_t$  0.15 mm/tooth (R)  $f_t$  0.08 mm/tooth



Estimated cutting process in ceramic milling of Inconel 718 with shear-type chip generation

## 4. Conclusion

- ✓ Higher dynamic stiffness and lower natural frequency in the vertical direction are advantageous to prevent tool damages.
- ✓ The cutting edge shape gradually deteriorates as the cumulative cutting distance increases.
- ✓ A Specific groove is formed at the center of the chamfered cutting edge before breakage occurrence.
- ✓ Chip removal process is classified into the shear-type.

# On statistical properties of a turbulent boundary layer affected by the cylinder wake in a freestream



Kousuke HIRUTA

[hiruta.kosuke@a.mbox.nagoya-u.ac.jp](mailto:hiruta.kosuke@a.mbox.nagoya-u.ac.jp)

Kouji NAGATA

[nagata@mech.nagoya-u.ac.jp](mailto:nagata@mech.nagoya-u.ac.jp)

Yasuhiko SAKAI

[ysakai@nagoya-u.jp](mailto:ysakai@nagoya-u.jp)

Osamu TERASHIMA

[o-terashima@mech.nagoya-u.ac.jp](mailto:o-terashima@mech.nagoya-u.ac.jp)

Yasumasa ITO

[yito@mech.nagoya-u.ac.jp](mailto:yito@mech.nagoya-u.ac.jp)

Department of Mechanical Science and Engineering, Nagoya University

Furo-cho, Chikusa-ku, Nagoya 464-8603, JAPAN

## Abstract

Effects of a cylinder wake turbulence (CWT) on a turbulent boundary layer (TBL) over a flat plate are experimentally investigated in a wind tunnel (Fig.1). The cylinder location was changed to generate different types of turbulence (fig.2).

Figure 3 shows that turbulence intensities normalized by the inner parameters in the case of turbulent boundary layer with periodic cylinder wake turbulence in a freestream (Case 3). The turbulence intensities are suppressed by the cylinder wake.

Figure 4 shows the ensemble average of velocity in the bursting event in the case of turbulent boundary layer with periodic cylinder wake turbulence in a freestream (Case 3). The velocity fluctuation during the sweep phase is increased by the cylinder wake.

## Biography

Kousuke HIRUTA received the Bachelor degree in Engineering from Nagoya University in 2011. He currently belongs to the statistical fluid engineering group and is pursuing the Master's degree.

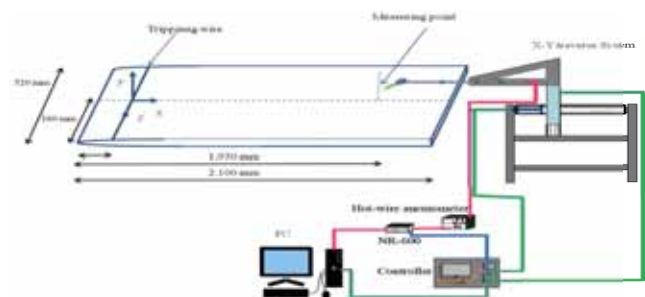


Fig.1 Schematics of experimental apparatus

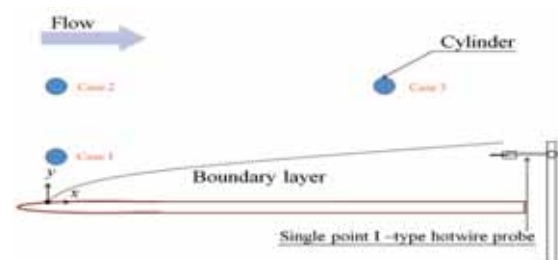


Fig.2 Experimental condition

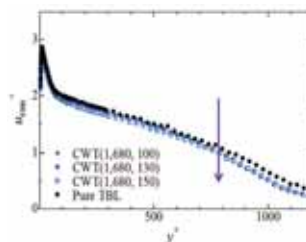


Fig. 3 Vertical profiles of the turbulence intensity (Case 3)

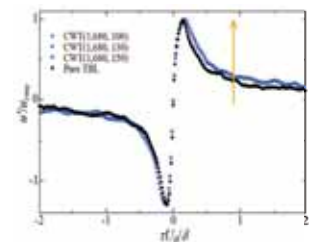


Fig. 4 The ensemble average of velocity in the bursting event (Case 3)

# On Statistical Properties of a Turbulent Boundary Layer Affected by the Cylinder Wake in a Freestream

○Kousuke HIRUTA, Kouji NAGATA, Yasuhiko SAKAI, Osamu TERASHIMA and Yasumasa ITO  
Dept. of Mechanical Science and Engineering, Nagoya University

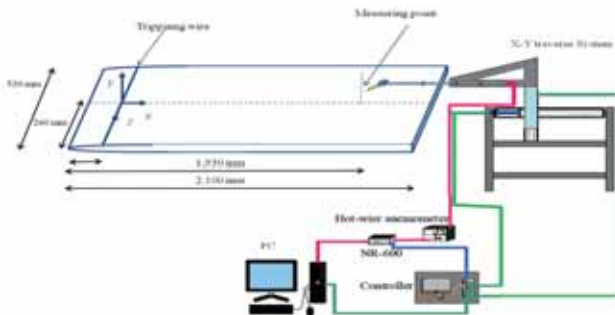
## Abstract

Effects of a cylinder wake turbulence (CWT) on statistical properties of a turbulent boundary layer (TBL) over a flat plate are experimentally investigated in a wind tunnel. The results show that turbulence intensities normalized by the inner parameters are suppressed by the cylinder wake. The velocity fluctuation during the sweep phase in the bursting event is increased by the cylinder wake.

## Introduction

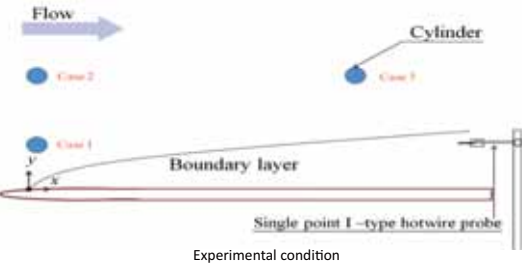
Past researches on turbulent boundary layers have shown that the turbulence intensities are strongly affected by freestream turbulence. Most of these researches have investigated only the effects of weak, small-scale turbulence in a free stream. On the other hand, we investigated the effects of large-scale freestream turbulence generated by a cylinder on statistical properties of a turbulent boundary layer. Experiments have been carried out in a wind tunnel and the streamwise and vertical velocities were measured by a hot wire anemometer.

## Experimental condition



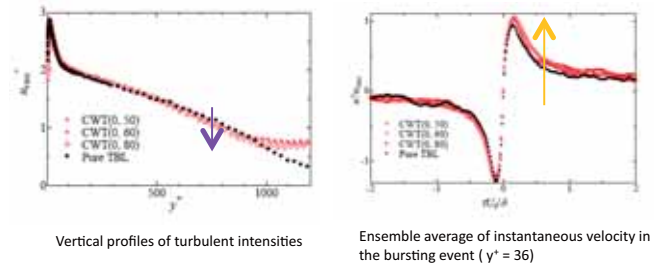
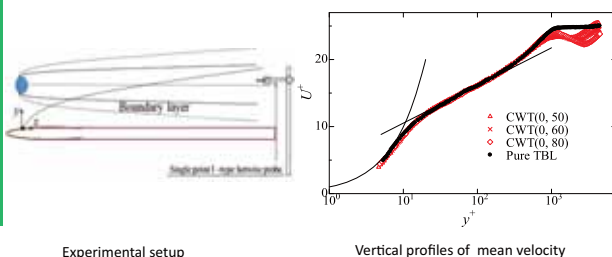
Experimental condition of pure turbulent boundary layer without free stream turbulence

$Re[m^{-1}]$	$Re_0$	$\delta[mm]$	$u_t[m/s]$
738,000	3,140	44	0.583

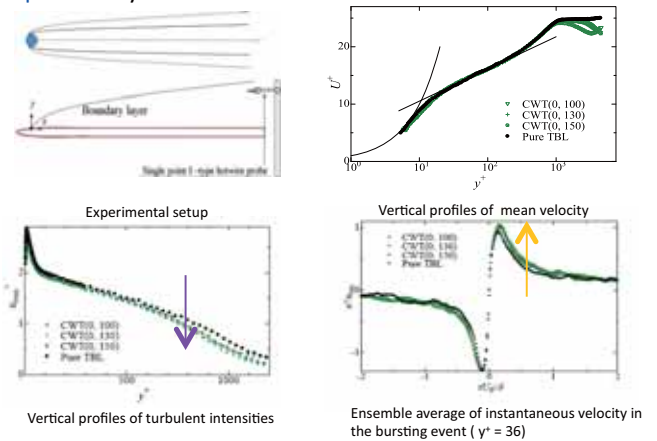


## Results

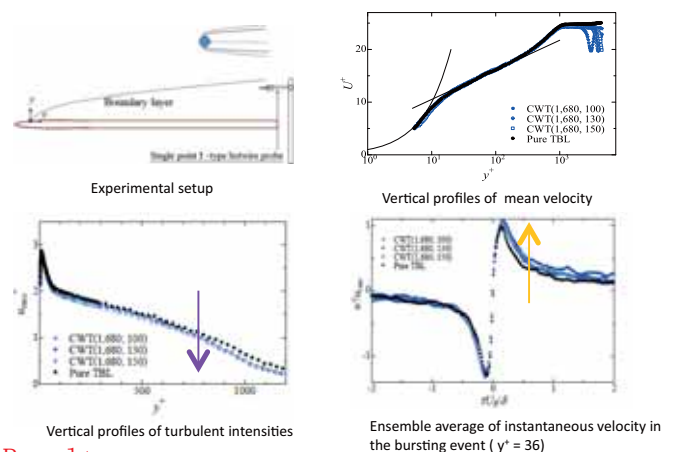
**Case 1 :** Turbulent boundary layer directly influenced by no-periodic cylinder wake turbulence in a free-stream



**Case 2 :** Turbulent boundary layer indirectly influenced by no-periodic cylinder wake turbulence in a free-stream



**Case 3 :** Turbulent boundary layer indirectly influenced by periodic cylinder wake turbulence in a free-stream



## Results

- Turbulence intensities normalized by the inner parameters are suppressed by the cylinder wake in all cases. In the case of TBL with CWT in a freestream (Cases 2 and 3), turbulence intensities in the outer region are largely suppressed compared with that in the TBL directly influenced by CWT (Case 1).
- The velocity fluctuation during the sweep phase in the bursting event is increased by the cylinder wake. On the other hand, the velocity fluctuation during the ejection phase in the bursting event does not significantly change.

## References

- (1) Blackwelder, R. F. and Haritonidis, J. H., "Scaling of the bursting frequency in the turbulent boundary layer", Journal of Fluid Mechanics, Vol. 318, (1996), pp. 339-372.
- (2) Nagata, K., Sakai, Y., and Komori, S., "Effects of small-scale freestream turbulence on turbulent boundary layers with and without thermal convection", Physics of Fluids, Vol. 23, (2011), 065111.

# Measurements of High-Schmidt-Number Scalar Mixing Layers in Grid Turbulence by means of PIV and PLIF



Koichi HOSHINO

Hoshino.koichi@e.mbox.nagoya-u.ac.jp

Yasuhiko SAKAI

ysakai@mech.nagoya-u.ac.jp

Kouji NAGATA

nagata@nagoya-u.ac.jp

Hiroki SUZUKI

hsuzuki@nitech.ac.jp

Yasumasa ITO

yito@mech.nagoya-u.ac.jp

Graduate School of Engineering, Nagoya University  
Furo-cho, Chikusa-ku, Nagoya 464-8603, JAPAN

## Abstract

High-Schmidt-Number scalar mixing layers in grid turbulence are experimentally investigated in a water channel. The particle image velocimetry (PIV) and the planar laser induced fluorescence (PLIF) techniques are applied to measure instantaneous streamwise and vertical velocities and instantaneous concentration respectively.

Fig.1 shows the schematic of the experimental apparatus and measuring system. A regular grid or a fractal square grid (Fig.2) is installed at the entrance of the test section to generate turbulence. The flow is separated into upper and lower layers by a splitter plate installed at the upstream of the grid. A turbulent scalar mixing layer develops downstream of the grid. The Reynolds number based on the mesh size,  $Re_M$ , is 2500 for both the cases.

Fig.3 shows the instantaneous fluctuation velocity vector,  $V(u, v)$ , normalized by cross-sectionally averaged mean velocity,  $U_0$ , in the regular grid turbulence and the fractal grid turbulence at  $x/M_{eff} = 40$ . It is found that velocity fluctuation in fractal grid turbulence is much larger than that in the regular grid turbulence.

## Biography

Koichi HOSHINO received the Bachelor degree in Engineering from Nagoya University in 2011. He was awarded the “Ichiju-syo” in “Nagare-no-Yume Contest” sponsored by Fluids Engineering Division of The Japan Society of Mechanical Engineers in 2010.

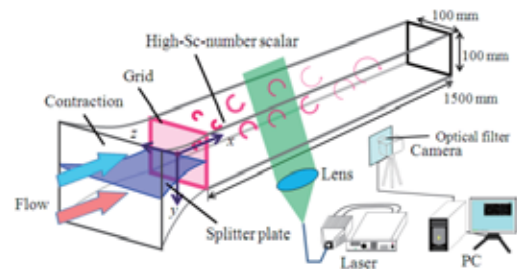


Fig.1 Schematic of experimental apparatus.

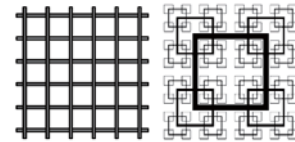


Fig.2 Schematics of turbulence grids. The left is regular grid and the right is fractal grid.

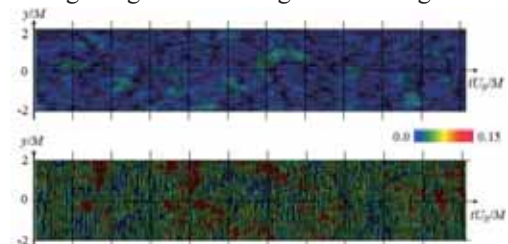


Fig.3 Instantaneous fluctuation velocity vector,  $V$ , normalized by cross-sectionally averaged mean velocity,  $U_0$ , in the regular (upper) and the fractal (lower) grid



# Measurements of High-Schmidt-Number Scalar Mixing Layers in Grid Turbulence by means of PIV and PLIF

Koichi Hoshino<sup>(1)</sup>, Yasuhiko Sakai<sup>(1)</sup>, Kouji Nagata<sup>(1)</sup>, Hiroki Suzuki<sup>(2)</sup>, Yasumasa ITO<sup>(1)</sup>

(1) Nagoya University (2) Nagoya Institute of Technology

## Introduction

The purpose of this study is to investigate high-Schmidt-number scalar mixing layers in **regular** and **fractal grid turbulence** in a water channel. The **particle image velocimetry (PIV)** and the **planar laser induced fluorescent (PLIF)** are applied to measure instantaneous streamwise and vertical velocities and instantaneous concentration respectively.

## Experiments

Fig.1 shows the schematic of the experimental apparatus. A **regular grid** or a **fractal square grid** are installed at the entrance of the test section to generate turbulence. The grid parameters are listed in Table. 1. Here,  $N$  is the fractal interaction,  $D_f$  is the fractal dimension,  $t_r$  is the thickness ratio of the largest to the smallest bar,  $\sigma$  is the blockage ratio,  $M_{\text{eff}}$  is the effective mesh size, defined as  $M_{\text{eff}} = (4T^2 / P_M) \sqrt{1 - \sigma}$ , where  $T^2$  is the cross-sectional area of the channel and  $P_M$  is the fractal perimeter's length of the grid. The flow is separated into upper and lower layers by a splitter plate installed at the upstream of the grid. A turbulent scalar mixing layer develops downstream of the grid. The Reynolds number based on the mesh size,  $\text{Re}_M$ , is 2500 for both the cases.

The **particle image velocimetry (PIV)** and the **planar laser induced fluorescence (PLIF) techniques** are used to measure the velocity and concentration fields. Fig.2 shows image processing procedure of PLIF. To obtain instantaneous non-dimensional concentration field, the captured images (Fig. 2(a)) and the background image (Fig. 2(b)) are taken separately. we obtained the processed image (Fig.2(c)) by subtracting the background image (Fig. 2(b)) from the captured image (Fig. 2(a)).

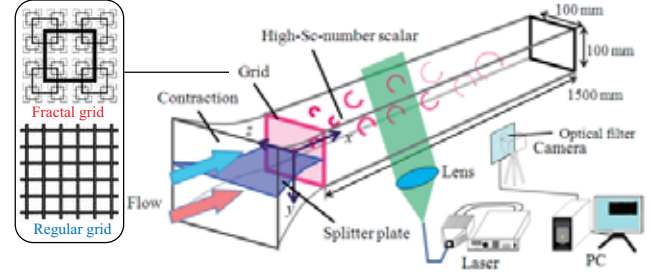


Fig.1 Schematic of experimental apparatus.

Tab.1 Parameters of grids.

	$N$	$D_f$	$t_r$	$\sigma$	$M_{\text{eff}}$	$\text{Re}_M$
Regular	1	2.0	1.0	0.36	10	2500
Fractal	4	2.0	9.76	0.36	5.68	2500

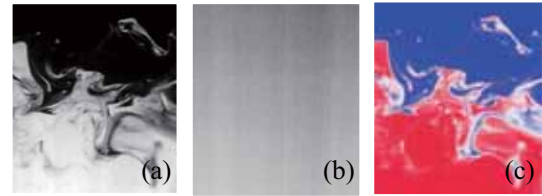


Fig.2 Image processing procedure: (a) a captured image; (b) a background image (reference); an instantaneous non-dimensional concentration fields provided from (a) and (b). In (a) and (b), white: high brightness; black: zero brightness. In (c), red: C=1; white: C=0.5; blue: C=0, where C is instantaneous non-dimensional concentration.

## Results

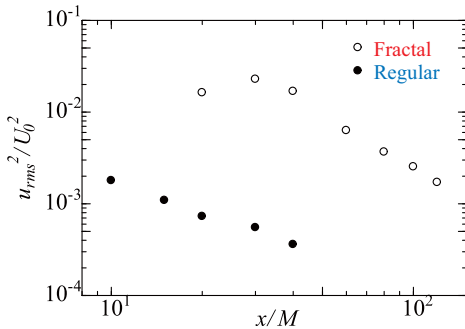


Fig. 4 The downstream profile of streamwise velocity fluctuations

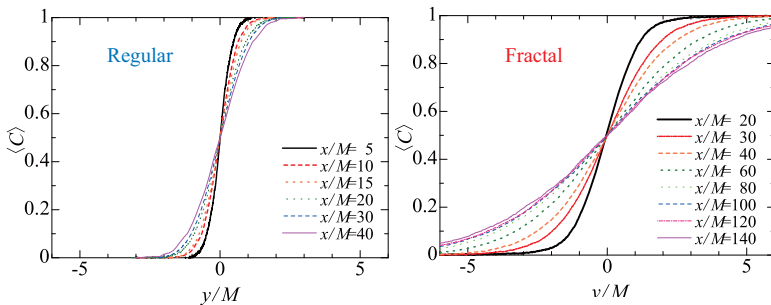


Fig.5 Vertical profiles of the mean concentration

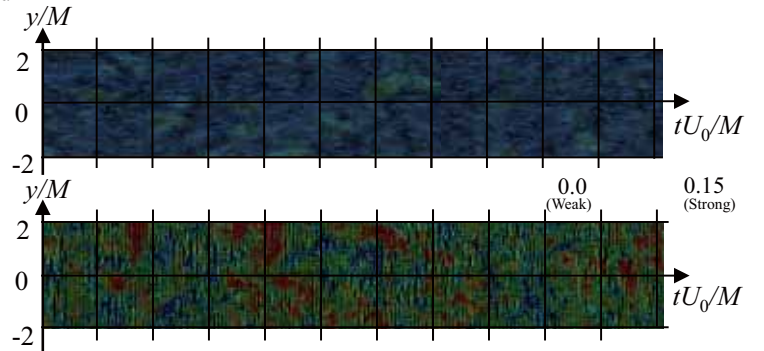


Fig.3 Instantaneous fluctuation velocity vector,  $V$ , normalized by the cross-sectionally averaged mean velocity  $U_0$  in the regular (upper) and the fractal (lower) grid turbulence at  $x/M_{\text{eff}} = 40$ .

Fig.3 shows that the velocity fluctuation in the **fractal grid turbulence** is much larger than that in the **regular grid turbulence**. Fig.4 shows that the turbulence intensity in the **fractal grid turbulence** has a peak around  $x/M = 30$  though that in the **regular grid turbulence** monotonically decreases in the streamwise direction.

Fig.5 shows that the turbulence diffusion is promoted more by the **fractal grid turbulence** than by the **regular grid turbulence** even when the Reynolds number,  $\text{Re}_M$ , is identical.

# Turbulent Mixing in a Planar Liquid Jet with a Second-Order Chemical Reaction



Tomoaki WATANABE  
[watanabe.tomoaki@c.nagoya-u.jp](mailto:watanabe.tomoaki@c.nagoya-u.jp)  
 Yasuhiko SAKAI  
[ysakai@mech.nagoya-u.ac.jp](mailto:ysakai@mech.nagoya-u.ac.jp)  
 Kouji NAGATA  
[nagata@nagoya-u.jp](mailto:nagata@nagoya-u.jp)  
 Osamu TERASHIMA  
[o-terashima@mech.nagoya-u.ac.jp](mailto:o-terashima@mech.nagoya-u.ac.jp)  
 Yasumasa ITO  
[yito@mech.nagoya-u.ac.jp](mailto:yito@mech.nagoya-u.ac.jp)

Department of Mechanical Science and Engineering, Nagoya University  
 Furo-cho, Chikusa-ku, Nagoya 464-8603, JAPAN

## Abstract

A turbulent planar liquid jet with a second-order chemical reaction ( $A + B \rightarrow R$ ) is investigated experimentally. The purpose of this study is to clarify the influence of the chemical reaction on the turbulent mass flux of reactive species. A main stream contains species B and a water solution of species A is issued into the main stream by the planar jet (Fig. 1). The streamwise velocity and the concentrations of all species are measured simultaneously by a combined probe consisting of an I-type hot-film probe and an optical fiber probe based on light absorption spectrometric method.

Figure 2 shows the turbulent mass flux of reactive species on the jet centerline. The results show that the behavior of the turbulent mass flux of the reactant species is different between the upstream ( $x/d < 25$ ) and the far ( $x/d > 25$ ) region. The turbulent mass flux of the product species is negative in the upstream region but positive in the far region.

## Biography

Tomoaki WATANABE received the Bachelor degree in Engineering from Nagoya University in 2011. He currently belongs to the statistical fluid engineering group and is pursuing the Master's degree.

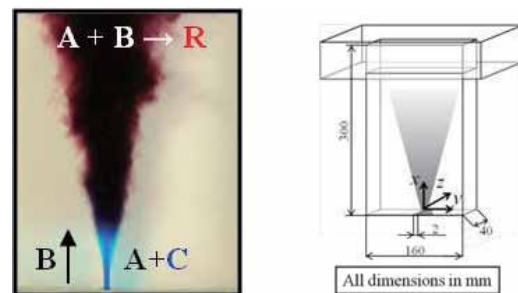


Fig. 1 Schematics of experimental apparatus.

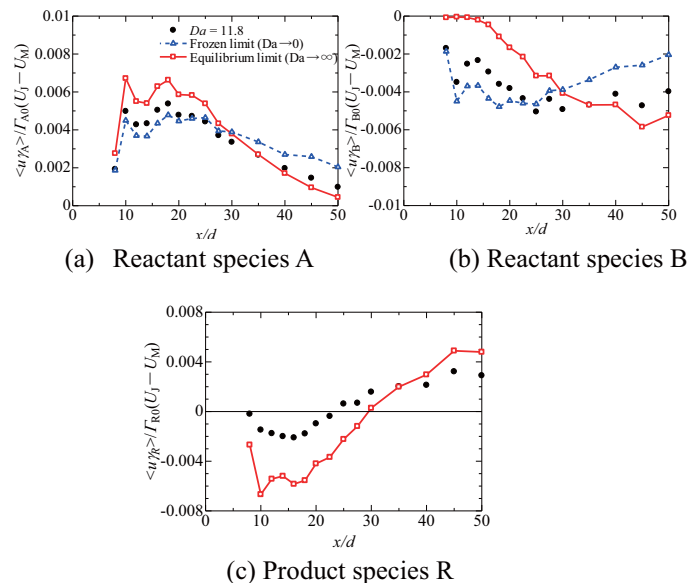


Fig. 2 Streamwise turbulent mass flux of reactive species on the jet centerline

# Turbulent Mixing in a Planar Liquid Jet with a Second-Order Chemical Reaction

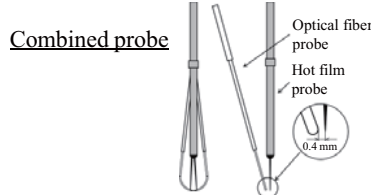
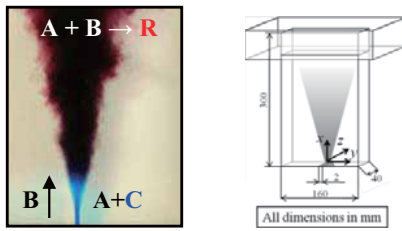
○Tomoaki WATANABE, Yasuhiko SAKAI, Kouji NAGATA, Osamu TERASHIMA and Yasumasa ITO  
Department of Mechanical Science and Engineering, Nagoya University

## Abstract

A turbulent planar liquid jet with a second-order chemical reaction ( $A + B \rightarrow R$ ) is investigated experimentally. A planar jet (A) is issued into a main stream (B). The streamwise velocity and the concentrations of all species are measured simultaneously. The results show that the influence of the chemical reaction on the turbulent mass flux of the reactant species near the jet exit is different from that in the far region. The turbulent mass flux of the product species is negative near the jet exit but positive in the far region.

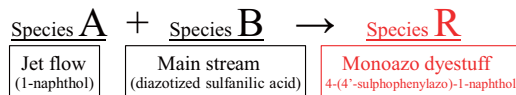
## Experiments

The purpose of this study is to investigate the influence of the chemical reaction on the turbulent mass flux of reactive species. We used a combined probe which consists of an I-type hot-film anemometer and an optical fiber probe<sup>[1]</sup> to simultaneously measure the streamwise velocity and the concentrations of reactive species. The optical fiber probe is based on the light absorption spectrometric method.



Reynolds number	$Re = (U_j - U_M)d/\nu = 2,200$
Damköhler number	$Da = k(\Gamma_{A0} + \Gamma_{B0})/(U_j - U_M) = 11.8$
Jet velocity	$U_j = 1.29$ [m/s]
Main stream velocity	$U_M = 0.073$ [m/s]
<u>Initial concentration</u>	Species A : $\Gamma_{A0} = 0.4$ [mol/m <sup>3</sup> ] Species B : $\Gamma_{B0} = 0.2$ [mol/m <sup>3</sup> ] Species C : $\Gamma_{C0} = 0.1$ [kg/m <sup>3</sup> ]

## • Chemical Reaction



Blue dyestuff, C : conserved scalar (jet flow)

## • Concentration Measurement

Absorptive species R and C : directly measured

•• optical fiber probe based on light absorption spectrometric method

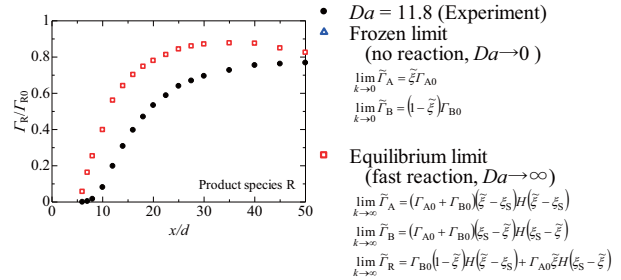
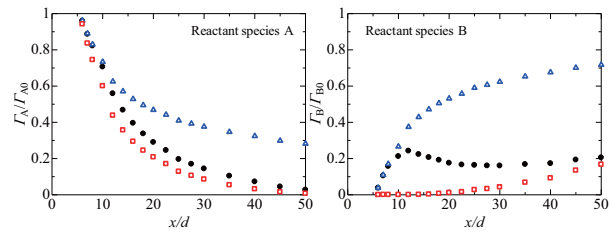
Species A and B : calculated from  $\tilde{T}_R$  and  $\tilde{T}_C$  using conserved scalar theory<sup>[2]</sup>

•••  $\tilde{T}_A = \tilde{\xi}\Gamma_{A0} - \tilde{T}_R$ ,  $\tilde{T}_B = (1 - \tilde{\xi})\Gamma_{B0} - \tilde{T}_R$ .

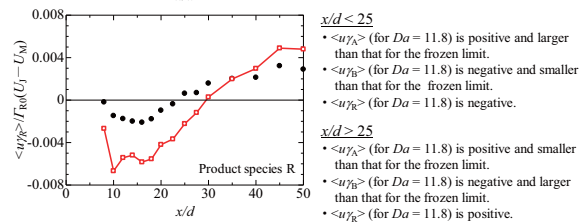
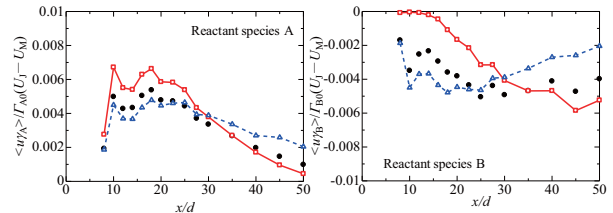
Mixture fraction :  $\tilde{\xi} = \tilde{T}_C/\Gamma_{C0}$

## Results

### • Mean Concentration on the Jet Centerline



### • Streamwise Turbulent Mass Flux on the Jet Centerline



### • Influence of chemical reaction on $\langle u_i \gamma_i \rangle$

In the far region ( $x/d > 25$ ), the deficient reactant is species A (contained in the jet flow) whereas species B (contained in the main stream) is the deficient reactant in the upstream region ( $x/d < 25$ ). This difference causes the different behavior of  $\langle u_i \gamma_i \rangle$  ( $i = A, B, \text{ or } R$ ) between the upstream and the downstream region.

### Reference

- [1] Nakamura, I., Sakai, Y. and Miyata, M., "Diffusion of Matter by a Non-Buoyant Plume in Grid-Generated Turbulence.", Journal of Fluid Mechanics, 1987, vol. 178, pp. 379-403.
- [2] Bilger, R. W., Saetran, L. R. and Krishnamoorthy, L. V., "Reaction in a Scalar Mixing Layer.", Journal of Fluid Mechanics, 1991, vol. 233, pp. 211-242.

# Improvement of light detection of photodiode with local surface plasmon resonance



Atsushi ISHIGURO

ishiguro.atsushi@c.mbox.nagoya-u.ac.jp

Yasuyuki MORITA

morita@mech.nagoya-u.ac.jp

Yang JU

ju@mech.nagoya-u.ac.jp

Graduate School of Engineering, Nagoya University

Furo-cho, Chikusa-ku, Nagoya 464-8603, JAPAN

ishiguro.atsushi@c.mbox.nagoya-u.ac.jp

## Abstract

Photodiode is widely used as detector of light. It has advantages over the other detectors of light in cost, lifetime and so on. But it has disadvantages in sensitivity of light detection. Therefore, that doesn't suitable for measurement of low-intensity light. In our research, we report improvement of light detection of photodiode via excitation of local surface plasmon resonance in Au nanoparticles deposited on the photodiode surface.

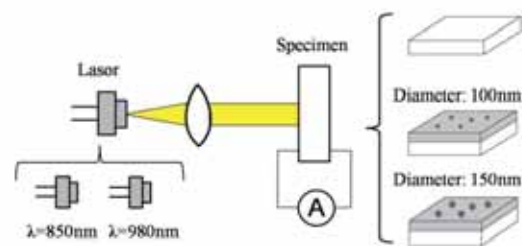


Fig. 1: Optical system for the experiment

By measuring current of photodiode, we investigated improvement of light detection of photodiode. Fig. 1 shows an optical system for measuring the current. In the experiment, we used two kinds of Au nanoparticles whose diameters are 100nm and 150nm respectively. Before the experiment, Au nanoparticles are scattered by using ultrasonic cleaner.

Fig. 2 (a) shows that current of photodiode increased by 4.4% (100nm), 4.2%(150nm). Fig. 2 (b) shows that it increased by 8.2%(100nm), 6.1%(150nm). But, as density of particles increase, these current decrease(Fig. 3). We considered that the increase were caused by condensation of nanoparticles.

We succeeded improvement of light detection of photodiode as increasing current of photodiode via excitation of local surface plasmon resonance in Au nanoparticles. And we report condensation of particles suppressed the current from increasing.

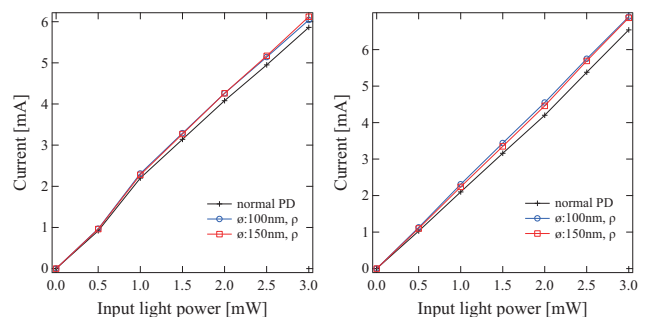


Fig. 2: Current of photodiode as a function of input light power at wavelengths of (a) 850 nm, (b) 980 nm

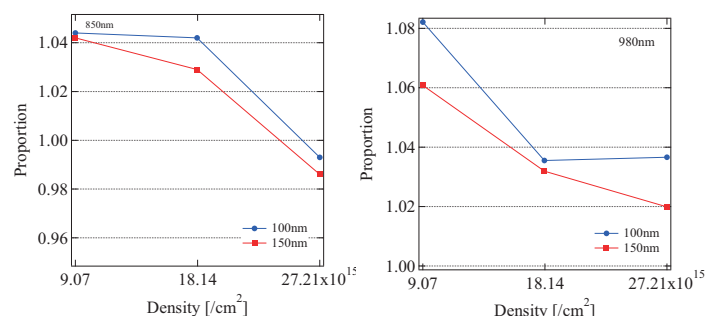


Fig. 3: Output power ratio of photodiode current enhanced by Au nanoparticles to normal in density variations of particles at wavelengths of (a) 850 nm, (b) 980 nm

## Biography

Atsushi Ishiguro received the Bachelor degree in Engineering from Nagoya University in 2011. He is currently Master degree student in Nagoya University, focusing on the studies of fabricating metal nanoparticles.

# Improvement of light detection of photodiode with local surface plasmon resonance

Atsushi Ishiguro\* Yasuyuki Morita\* Yang Ju\*

\* Department of Mechanical and Science, Nagoya University

March, 2012

## PURPOSE

Photodiode is widely used as detector of light. It has advantages over the other detectors of light in cost, lifetime and so on. But it has disadvantages in sensitivity of light detection. Therefore, that doesn't suitable for measurement of low-intensity light. In our research, we report improvement of light detection of photodiode via excitation of local surface plasmon resonance in Au nanoparticles deposited on the photodiode surface.

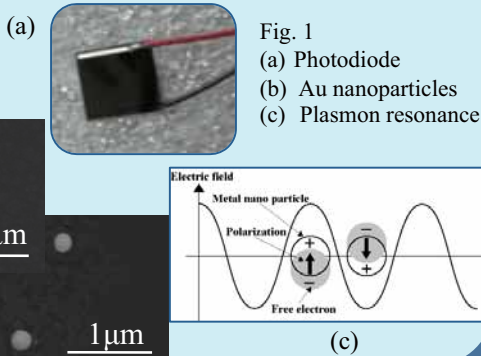


Fig. 1  
(a) Photodiode  
(b) Au nanoparticles  
(c) Plasmon resonance

## EXPERIMENT

By measuring current of photodiode, we investigated improvement of light detection of photodiode. Fig. 2 shows an optical system for measuring the current. In the experiment, we used two kinds of Au nanoparticles whose diameters are 100nm and 150nm respectively. Before the experiment, Au nanoparticles are scattered by using ultrasonic cleaner(Fig. 3).

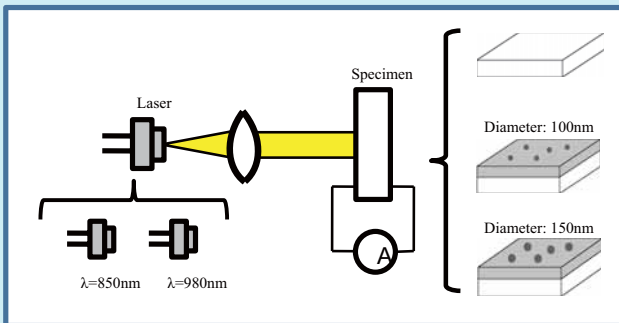


Fig. 2: Optical system for the experiment.



Fig. 3: Observation of Au nanoparticles by SEM:  
(a) before using ultrasonic cleaner; (b) after using ultrasonic cleaner.

## RESULTS

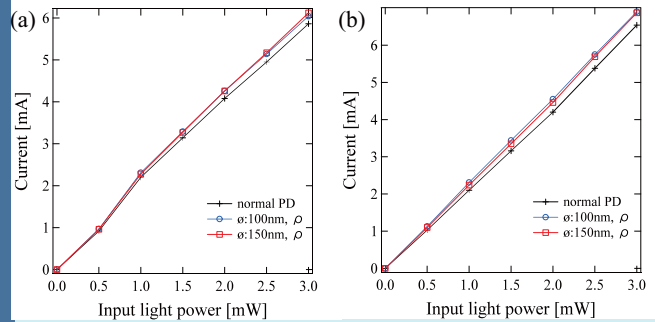


Fig. 4: Current of photodiode as a function of input light power at wavelengths of (a) 850 nm, (b) 980 nm

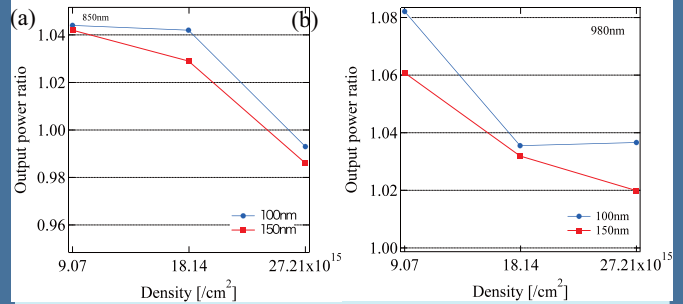


Fig. 5: Output power ratio of photodiode current enhanced by Au nanoparticles to normal in density variations of particles at wavelengths of (a) 850 nm, (b) 980 nm

Fig. 4 (a) shows that current of photodiode increased by 4.4% (100nm), 4.2%(150nm). Fig. 4 (b) shows that it increased by 8.2%(100nm), 6.1%(150nm). But, as density of particles increase, these current decrease(Fig. 5). We considered that the increase were caused by condensation of nanoparticles(Fig. 6).

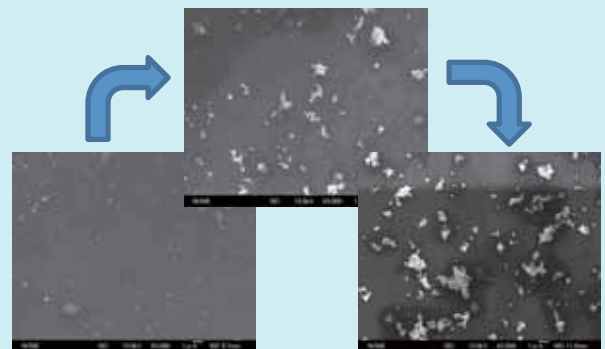


Fig. 6: Changes of particles condensation

## CONCLUSION

We succeeded improvement of light detection of photodiode as increasing current of photodiode via excitation of local surface plasmon resonance in Au nanoparticles. And we report condensation of particles suppressed the current from increasing.

# Effect of cyclic mechanical stretching on stem cell-to-tenocyte differentiation: Assessment by extracellular matrix expression levels and structure



Satoshi SUZUKI

Suzuki.satoshi@h.mbox-u.ac.jp

Yasuyuki MORITA

morita@mech.nagoya-u.ac.jp

Yang JU

ju@mech.nagoya-u.ac.jp

Graduate School of Engineering, Nagoya University  
Furo-cho, Chikusa-ku, Nagoya 464-8603, JAPAN

## Abstract

In the human body, tendon is a type of connective tissue which physically binds muscles to skeletal structures permitting locomotion and enhancing joint stability. There are some problems in the current treatment of tendon.

Meanwhile several researchers have shown that cyclic uniaxial stretching effects human marrow mesenchymal stem cells (hMSCs) differentiation into tenocytes. From this, many researchers try to construct tendon tissue from stem cells. The organization of the extracellular matrix (ECM) of tendon is the principal determinants of the physiological function and the mechanical strength of tendon. Tendon is mainly constructed from collagen type I (Col I) and tenascin-C (TNC), so Col I and TNC are commonly used to confirm the differentiation of stem cells into tenocyte and construction of tendon structure.

In this study, stem cells were applied uniaxial cyclic mechanical stretching(Fig.1), and the influence of mechanical stretching on the ECM expression and construction was analyzed. In Fig.2, expression level of Col I and TNC at 48h was higher than at 24h and at 8% stretching was higher than at 10%. Additionally, the increasing rate of ECM expression level from 24h to 48h was higher at 8% stretching than 10%.

From fluorescence images of stem cells and ECM after stretching(Fig.3), at each parameter, positive expression of Col I could be confirmed from all images, but TNC could not. Figure 4 shows the binary images of fluorescence images. The area and degree of circularity of each mass was calculated by image processing. At 10% stretching, the area of Col I was larger and the degree of circularity was smaller than 8% stretching. From this result, at 10% stretching, Col I expressed by mechanical stretching constructed some structure.

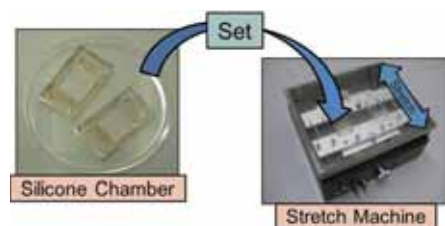


Fig.1. Mechanical stretching instruments. Stem were cells seeded on the silicone chamber.

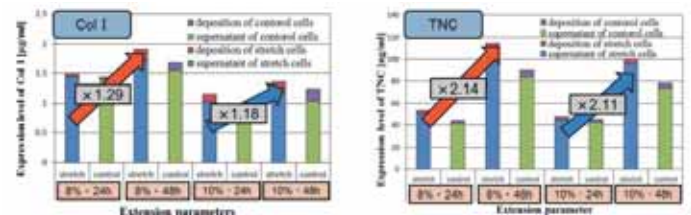


Fig.2. Expression level of ECM measured by absorbance determination.

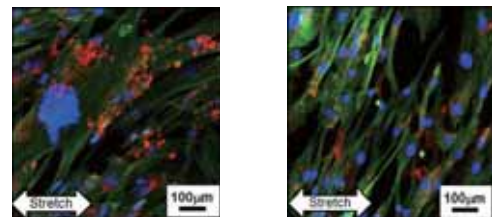


Fig.3. Fluorescence images. In these images, blue section shows nucleus, green shows cytoskeleton, red shows Col I and purple shows TNC.

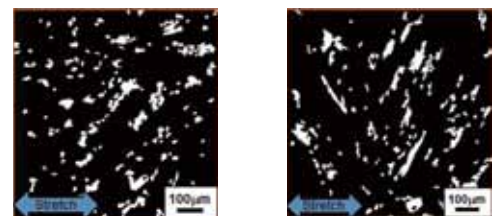


Fig.4. Binary images of Col

## Biography

Satoshi Suzuki received the Bachelor degree in engineering from Nagoya University in 2011. He is currently a student of master's course in Nagoya University, focusing on the study of tissue engineering.

# Effect of cyclic mechanical stretching on stem cell-to-tenocyte differentiation: Assessment by extracellular matrix expression levels and structure



Satoshi Suzuki, Sachi Watanabe, Yasuyuki Morita, Yang Ju  
Department of Mechanical Science and Engineering, Nagoya University

## Introduction

In the human body, tendon is a type of connective tissue which physically binds muscles to skeletal structures permitting locomotion and enhancing joint stability. However, there are some problems in the current treatments of tendon. Meanwhile several researchers have shown that cyclic uniaxial stretching effects human marrow mesenchymal stem cells(hMSCs) differentiation into tenocyte. Then, many researchers have tried to construct tendon tissue from stem cells. The organization of the extracellular matrix(ECM) is the principal determinants of the physiological function and the mechanical strength of tendon. Tendon is mainly constructed from type 1 collagen(Col 1) and tenascin-C (TNC). In this study, stem cells were applied uniaxial cyclic mechanical stretching, and the influence of mechanical stretching on the ECM expression and construction was analyzed.

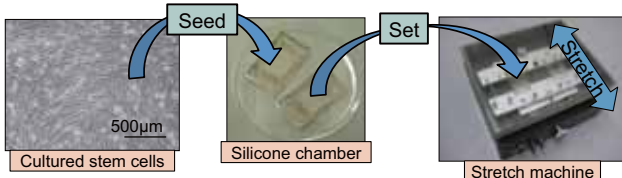
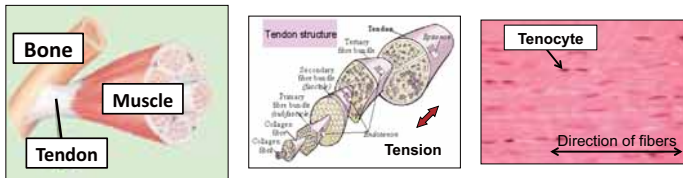


Fig.1.Exposure to mechanical stretch.

Stretch parameter					
	sample1	sample2	sample3	sample4	control
frequency		1Hz			0Hz
extension ratio	8%		10%		0%
duration	24h	48h	24h	48h	24h 48h

### Analyzing ECM

- Measuring Expression Level → Absorbance Determination
- Observing the structure of ECM → Fluorescence Staining

### Measure subject

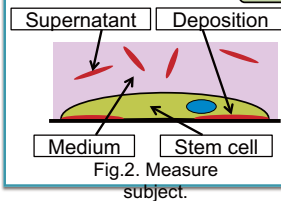


Fig.2. Measure subject.

Absorbance was measured at 450nm wavelength. Fig.2 shows the measure subjects. The subjects were ECM dissolved in supernatant and depositing around cells.

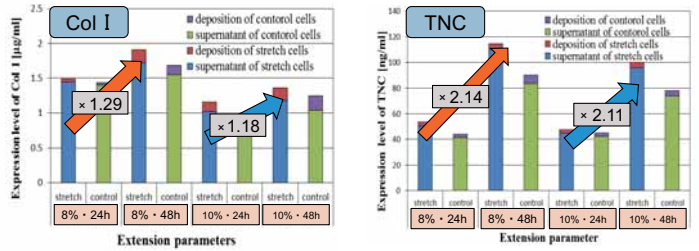


Fig.3. Expression Level of ECM.

Subject : Supernatant > Deposition  
Duration : 48h > 24h  
Extension Ratio : 8% > 10%

Increasing rate of ECM(24h→48h)		
	8%	10%
Col I	1.29	1.18
TNC	2.14	2.11

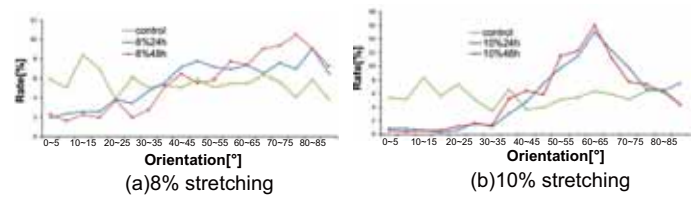


Fig.4. Orientation of Cells after Stretching.

Cell Orientation 8%: Slowly, 10%: Rapidly



### Analysis structure of Col I

Positive expression of Col 1 could be confirmed from all images, but TNC could not. The structure of Col 1 of 8%48h and 10%48h stretching were compared from fluorescence and binary images. The area and degree of circularity of each mass was calculated.

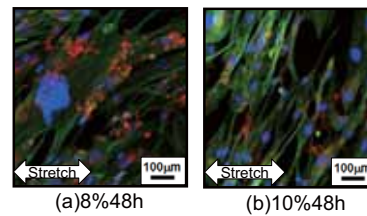


Fig.5. Fluorescence Images.

### Explanatory note

- Col I (red)
- Cell nucleus (blue)
- TNC (magenta)
- Cell cytoskeleton (green)

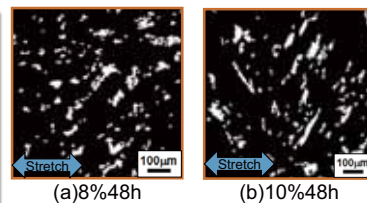


Fig.6. Binary Images.

Comparison 8% and 10%		
	Average Area	Average Degree of Circularity
8%	1289	0.470
10%	1780	0.124

Area : 10% > 8%  
Degree of Circularity : 8% > 10%

At 10% stretching, Col 1 constructed some structure.

Figure 3 shows the result of absorbance determination. ECM contained in supernatant was extremely numerous compared with deposition. Especially, this trend was particular at TNC. Additionally, the increasing rate of ECM expression level from 24h to 48h was higher at 8% stretching than 10%. Fig.4 shows comparison of cell orientation between stretching rate. Stem cells responded to mechanical stretching by reorganizing their orientation close to about 60°. Therefore, if stem cells are subjected to mechanical stretching at same extension rate, stimulation for cells is decreased with the orientation.

- The expression level of ECM was the highest at 8%48h.
- The expression level in supernatant was very high compare with deposition. Especially, this trend was particularly at TNC.
- The structure of Col 1 was the most particularly at 10%48h stretching.
- The different relativity of strain exists between the expression level and constructing structure of Col 1.

# Fabrication of high density Au nanowires by template method



Hiromasa TESHIMA

teshima.hiromasa@f.mbox.nagoya-u.ac.jp

Yang Ju

ju@mech.nagoya-u.ac.jp

Graduate School of Engineering, Nagoya University  
Furo-cho, Chikusa-ku, Nagoya 464-8603, Japan

## Abstract

There is an urgent need in nano devices, nano sensor and so on, of high density nanowires which can afford good mechanical support as well as electrical properties. Meanwhile in the nanotechnology, many excellent and unique structure-related properties such as the high mechanical strength, the high conductivity and the adhesion ability of nanowires have been studied. It is important to understand the crystal structure of nanowires in order to use them as the component of nano devices, nano sensor and so on.

In this paper, we fabricated Au nanowires by template method and observed them by scanning electron microscopy (SEM) and transmission electron microscopy (TEM). Figure 1 shows the schematic diagram of process chart of fabricating Au nanowires by template method.

Figure 2 is the AAO template used for the fabrication of high density nanowire array. Nanowires were deposited under a constant current of 0.002 A. Au nanowire array was characterized by SEM and TEM. Figure 3 shows that high density Au nanowire array has been fabricated. Au nanowires were continuous and the diameter of the Au nanowires was 200 nm. Au nanowires made on the thin Au film form bundled structures. The formation of these structures is related to the attractive interaction among the nanowires, for example van der Waals attraction. Figure 4 shows that Au nanowire had high density because electron beam didn't penetrate through the nanowire. Figure 5 shows that Au nanowire was polycrystalline structure because diffraction pattern image of Au nanowire was circular pattern.

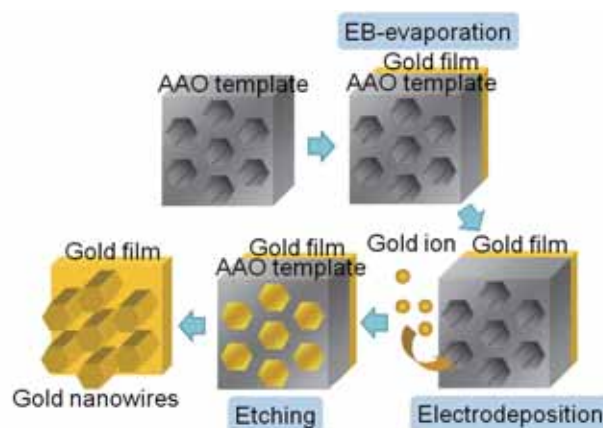


Fig.1 Schematic of process chart of fabricating Au nanowires by template method.

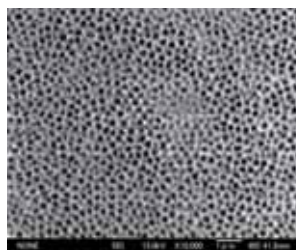


Fig.2 SEM image of AAO template.

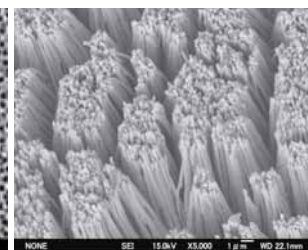


Fig.3 SEM image of Au nanowires.



Fig.4 TEM image of Au nanowire.



Fig.5 Diffraction patterns image of Au nanowire.

## Biography

Hiromasa Teshima received the Bachelor degree in Engineering from University of Nagoya, Japan, in 2009. He is currently a student of master's course in Nagoya University, studying Fabrication of high density Au nanowires by template method.

# Fabrication of high density Au nanowires by template method



Hiromasa Teshima, Yang Ju

Department of Mechanical Science and Engineering, Nagoya University

March, 2012

There is an urgent need in nano devices, nano sensor and so on, of high density nanowires which can afford good mechanical support as well as electrical properties. Meanwhile in the nanotechnology, many excellent and unique structure-related properties such as the high mechanical strength, the high conductivity and the adhesion ability of nanowires have been studied. It is important to understand crystal structure of nanowires in order to use them as the component of nano devices, nano sensor and so on.

In this paper, we fabricated Au nanowires by template method and observed them by scanning electron microscopy (SEM) and transmission electron microscopy (TEM).

To fabricate high density nanowire array, we adopt template method (Fig. 1a). Nanowires were deposited under a constant current of 0.002 A for 24h, 48h and 72h (Fig. 1b). Figure 2 shows SEM image of AAO template. Au nanowire array was characterized by SEM and TEM. Finally, we investigated a crystal structure of Au nanowire.

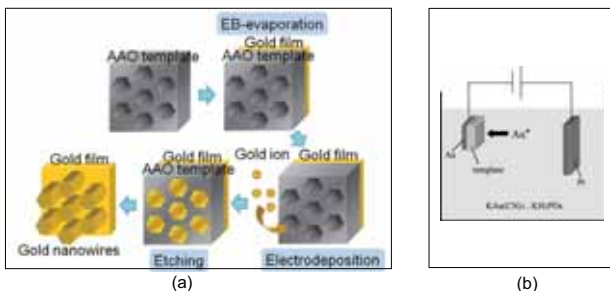


Fig. 1 Schematic of fabricating Au nanowires method: (a) Process chart of template method; and (b) Schematic of electrodeposition.

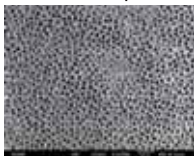


Fig. 2 SEM image of AAO template x10000.

SEM images shows that high density Au nanowire array has been fabricated for 24h, 48h and 72h (Fig. 2a, b, c, d, e, f). Au nanowires were continuous and the diameter of the Au nanowires was 200 nm. In all cases, Au nanowires made on the thin Au film formed bundled structures. It was considered that the formation of these structures was related to the attractive interaction among the nanowires, for example van der Waals attraction. It was considered that this phenomenon was characteristics of Au nanowires because the surfaces of Au nanowires were inoxidizable. In the cases of other metals, in order to repel each nanowires by having a slightly negative charge at the oxidized surfaces, nanowires are considered not to form bundled structures. In addition, it was found that the longer Au nanowires were, the larger bundled structures of Au nanowires became.

Figure 3g shows results of length measurements. It was found that the length of nanowires was in proportion to the time of electrodeposition.

Figure 4a and b show TEM image of Au nanowire. Figure 4 shows that Au nanowire had high density because electron beam didn't penetrate through the nanowire. Figure 4b shows TEM image of particle which constitute Au nanowire. It was considered lattice spacing of particle which constitute Au nanowire was 2.64 Å. On the other hand, in the case of Au, the longest lattice spacing (111) was 2.35 Å. So lattice plane of particle which constitute Au nanowire was considered to be (111) plane. Figure 4c shows electron diffraction pattern image of Au nanowire. This image shows a circular pattern and it was found that Au nanowire was polycrystalline structure. In addition, from that this circle was not perfect, it was found that the orientation distribution of crystal grain was not completely random and that the nanowire was polycrystal with a preferred orientation.

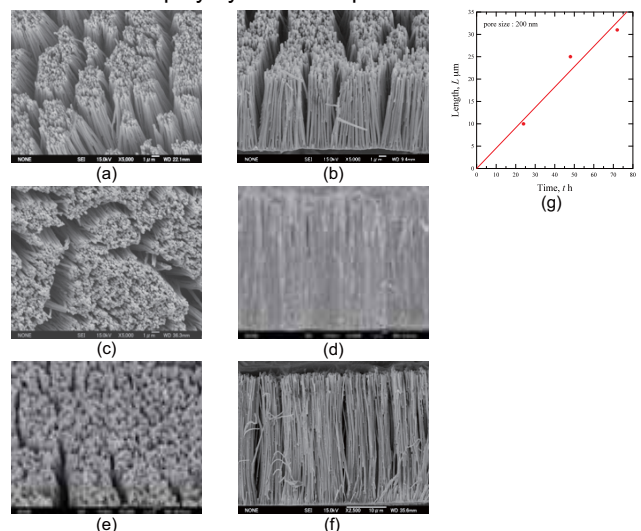


Fig. 3 SEM images of nanowires: time of deposition = 24h (a) view of the surface x5000; (b) cross-sectional view x5000; time of deposition = 48h (c) view of the surface x5000; (d) cross-sectional view x3000; time of deposition = 72h (e) view of the surface x5000; (f) cross-sectional view x2500; and (g) results of length measurements.

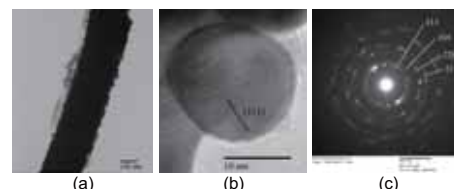


Fig. 4 TEM investigations of the individual nanowire: (a) TEM image of the Au nanowire; (b) high-resolution image; and (c) diffraction patterns of the Au nanowire shown in b.

1. High density Au nanowire array has been fabricated.
2. In all cases, Au nanowires formed bundled structure.
3. The length of Au nanowire was in proportion to the time of electrodeposition.
4. TEM observation showed Au nanowire was high density and polycrystalline structure.
5. It was considered the growth direction of particles which constitute Au nanowires was (111).

# Measurement of electrical properties of cell surface by Microwave Atomic Force Microscopy



Takanori MAKINO

makino.takanori@e.mbox.nagoya-u.ac.jp

Atsushi HOSOI

hosoi@mech.nagoya-u.ac.jp

Yasuyuki MORITA

morita@mech.nagoya-u.ac.jp

Yang JU

ju@mech.nagoya-u.ac.jp

Graduate School of Engineering, Nagoya University  
Furo-cho, Chikusa-ku, Nagoya 464-8603, JAPAN

## Abstract

Recently, regenerative medicine has been focused with stem cells that can regenerate lost human tissues and organs. It has become a great need to measure healthiness of cells non-invasively because of fear that non-health cells become cancer cells. We have proposed a microwave atomic force microscope (M-AFM) which can measure electrical properties and topography of cells has been developed.

M-AFM technique is a combination of the principles of an atomic force microscopy (AFM) and a microwave measurement technique. Microwave signals are emitted forward to the sample and reflection signals of microwave from the sample detected at the tip-top of the cantilever. The reflection signals of the microwave are measured to determine the electrical properties of the materials.

M-AFM probe was fabricated on a non-doped GaAs wafer by using wet etching process. A parallel-plate waveguide was formed by evaporating Au films onto the top and bottom surfaces of the probe. To make microwave signals emit from the tip-top of the probe, a nano-slit introduced by using focused ion beam (FIB) fabrication. Figure 1 shows the fabricated M-AFM probe.

Stem cells were used as a sample. AFM topography image and microwave image of the output voltage that was converted from the measured microwave signals were obtained by M-AFM, simultaneously. Figure 2 shows the experimental results. The M-AFM worked in non-contact mode. The scanning speed was fixed to 5  $\mu\text{m/s}$ , the scanning area was 20  $\mu\text{m} \times 20 \mu\text{m}$ . The response of the microwave signals changed corresponding to the different tissues of the cell. The experimental result demonstrates that electrical properties of the cell are different from each cell tissue.

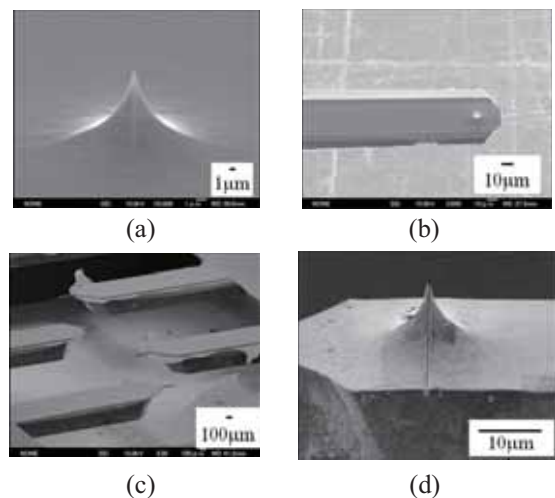


Fig.1 SEM images: (a) the tip of the GaAs AFM probe; (b) the cantilever of the M-AFM probe; (c) the M-AFM probes; (d) the nanoslit of the M-AFM probe

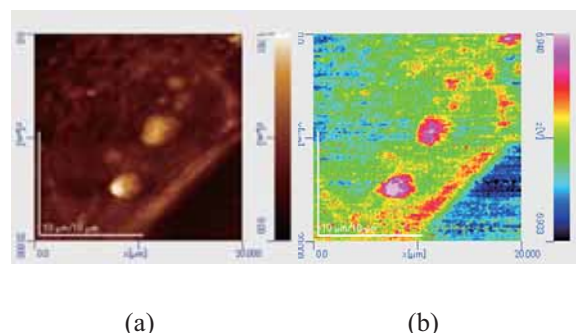


Fig.2 The scanning results of the stem cells by the M-AFM: (a) AFM topography; (b) Imaging by microwave signals.

## Biography

Takanori MAKINO received the Bachelor degree in Engineering from University of Nagoya, Japan, in 2009. He is currently a student of master's course in Nagoya University, studying the measurement of electrical properties of the materials by microwave atomic force microscopy.

# Measurement of electrical properties of cell surface by Microwave Atomic Force Microscopy

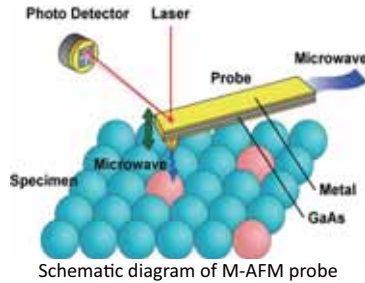


T. MAKINO\*, A. HOSOI\*, Y. MORITA\* and Y. Ju\*

\* Department of Mechanical Science and Engineering, Nagoya University

## Introduction

Recently, regenerative medicine has been focused with stem cells that can regenerate lost human tissues and organs. It has become a great need to measure healthiness of cells non-invasively because of fear that non-health cells become cancer cells.



Schematic diagram of M-AFM probe

We have proposed a microwave atomic force microscope (M-AFM) which can measure electrical properties and topography of cells has been developed. Microwave signals were emitted forward to the sample and reflection signals of microwave from the sample detected at the tip-top of the cantilever. The reflection signals of the microwave were measured to determine the electrical properties of the materials.

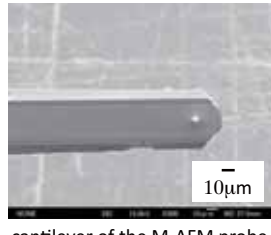
M-AFM probes were fabricated and the electrical properties of mesenchymal stem cells were measured by M-AFM.

## Experimental Setup

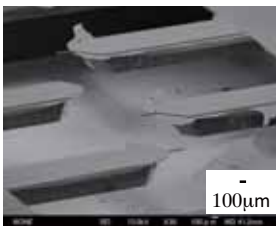
### Probe fabrication



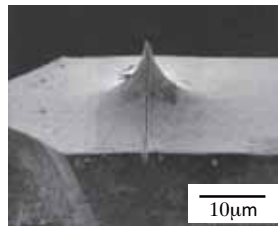
tip of the GaAs AFM probe



cantilever of the M-AFM probe



M-AFM probes

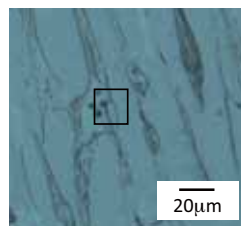


nanoslit of the M-AFM probe

A no doped GaAs wafer was used as the substrate of the probe. To obtain the desired structure, wet etching was used to fabricate the probe. A parallel-plate waveguide was formed by evaporating Au films onto the top and bottom surfaces of the probe. The Au films on both sides are connected at the end of the cantilever. To make microwave signals emit from tip-top of the probe, a nano-slit introduced by using focused ion beam (FIB) fabrication.

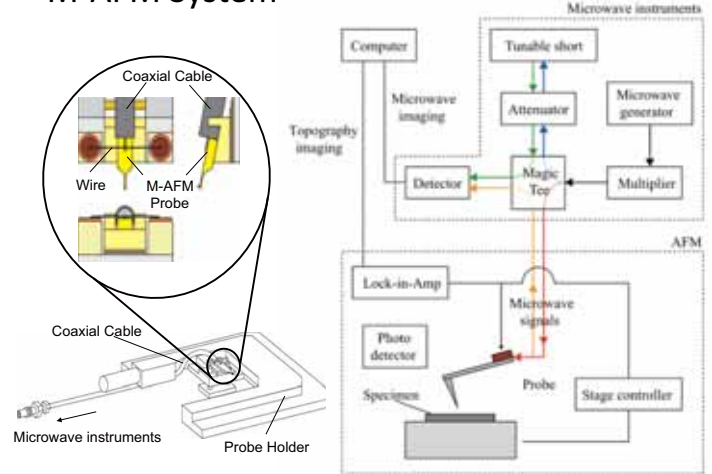
### Samples

Human bone marrow mesenchymal stem cells were used as the samples. Stem cells were dehydrated by using 50%, 70%, 80%, 90%, 99.5% concentrations ethanol and dried in atmosphere.



mesenchymal stem cells

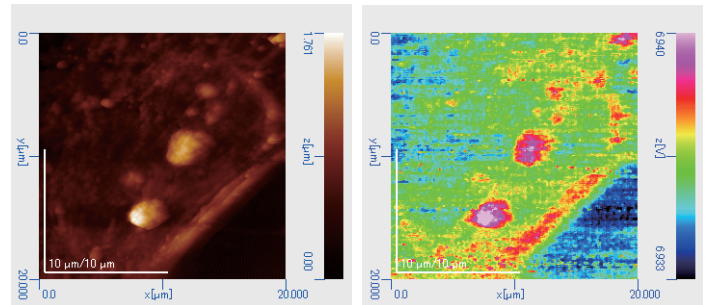
### M-AFM System



Attachment of the M-AFM probe

Diagram of the M-AFM system

## Experimental Results



AFM topography of the stem cell

Microwave image of the stem cell

Stem cells were measured by M-AFM. The M-AFM worked in noncontact mode. The scanning speed was fixed to 5  $\mu\text{m/s}$ , scanning area was 20  $\mu\text{m} \times 20 \mu\text{m}$ . The frequency of the microwave was 94 GHz. AFM topography image and microwave image of the output voltage that was converted from the measured microwave signals were obtained, simultaneously. The response of the microwave signals changed corresponding to the different tissues of the cell. This experimental result demonstrates that the electrical properties of the cell are different from each cell tissue. The spherical part of the cell is considered as a nucleus which is composed of proteins and nucleic acids found within the nucleus.

## Conclusion

M-AFM probes were fabricated on the GaAs wafer by using wet etching process. We succeeded in measuring both the microwave response and the surface topography of dried mesenchymal stem cells after ethanol dehydration by M-AFM with the probe. As a result, the change of microwave signals depending on the cell tissues was detected.

This work was supported by the Japan Society for the promotion of Science under Grants-in-Aid for Scientific Research (A) 20246028 and (S) 18106003.

# Measurement and evaluation of electrical conductivity of doped GaAs wafers using microwaves



Takahiro YOSHIDA

yoshida.takahiro@g.mbox.nagoya-u.ac.jp

Yang JU

ju@mech.nagoya-u.ac.jp

Graduate School of Engineering, Nagoya University  
Furo-cho, Chikusa-ku, Nagoya 464-8603, JAPAN

## Abstract

To control the quality of doped GaAs wafers either in the process of wafer manufacturing or device fabrication, it is important to know the electrical conductivities of the wafers. There is still no method available for measuring the conductivity nondestructively to characterize and control the quality of doped GaAs wafers during manufacturing or even the finished wafer products. In this study, analytical and explicit expressions of conductivity derived by microwave theory are carried out.

Therefore, after  $k_0$  and  $b_0$  in Eq. (1) are calibrated using two reference wafers whose conductivities are known, a wafer's conductivity can be determined by measuring the output voltage under the same conditions and evaluating Eqs. (1) and (2).

Figure 1 shows the view of the measurement where the wafer is set on the antenna in a contact fashion, i.e., the standoff distance is set to be zero.

Using their output voltages shown above, the conductivities of wafers are evaluated from Eqs. (1) and (2). The evaluated conductivities are compared with those measured using the Hall effect measurement (HEM) method in Fig. 2. From Fig. 2, it is found that the evaluated conductivities match well with the ones measured by the HEM method. The maximum error of evaluation is less than  $\pm 4.5\%$  of the conductivity of the wafers. The evaluation method and results are independent of the wafers' thicknesses. Therefore, a high-precision nondestructive evaluation method has been established.

$$V = k_0 |\Gamma_s|^2 + b_0 \quad (1)$$

$$|\Gamma_s| = \frac{|1 - \sqrt{\epsilon_r - j\sigma/(\omega\epsilon_0)}|}{|1 + \sqrt{\epsilon_r - j\sigma/(\omega\epsilon_0)}|} \quad (2)$$

$|\Gamma_s|$ : Absolute value of the top surface reflection coefficient  
 $\sigma$ : Conductivity of wafer  
 $\epsilon_r$ : Relative dielectric constant of wafer  
 $\omega$ : Angular frequency of microwave  
 $\epsilon_0$ : Permittivity of free space

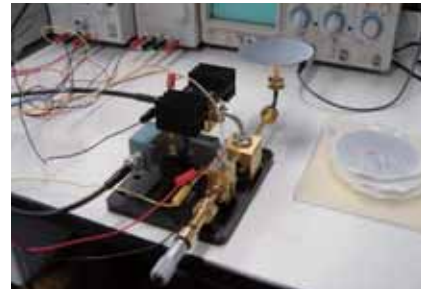


Fig. 1 Photograph of the experimental instrument with a doped GaAs wafer under measurement

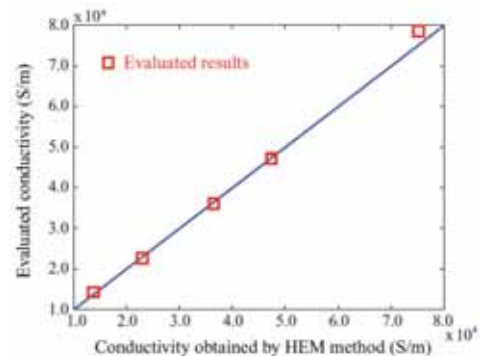


Fig. 2 Evaluated conductivities in comparison with those measured by the HEM method

## Biography

Takahiro Yoshida received the Bachelor degree in Engineering from University of Nagoya, Japan, in 2009. He is currently a student of master's course in Nagoya University, studying nondestructive measurement by microwave.

# Measurement and evaluation of electrical conductivity of doped GaAs wafers using microwaves



Takahiro Yoshida, Yang Ju  
Department of Mechanical Science and Engineering, Nagoya University

To control the quality of doped GaAs wafers either in the process of wafer manufacturing or device fabrication, it is important to know the electrical conductivities of the wafers. There is still no method available for measuring the conductivity nondestructively to characterize and control the quality of doped GaAs wafers during manufacturing or even the finished wafer products.

In this paper, analytical and explicit expressions of conductivity derived by microwave theory are carried out.

$$V = k_0 |\Gamma_s|^2 + b_0 \quad (1)$$

$$|\Gamma_s| = \left| \frac{1 - \sqrt{\epsilon_r - j\sigma/(\omega\epsilon_0)}}{1 + \sqrt{\epsilon_r - j\sigma/(\omega\epsilon_0)}} \right| \quad (2)$$

$|\Gamma_s|$  : Absolute value of the top surface reflection coefficient  
 $\sigma$  : Conductivity of wafer  
 $\epsilon_r$  : Relative dielectric constant of wafer  
 $\omega$  : Angular frequency of microwave  
 $\epsilon_0$  : Permittivity of free space

Therefore, after  $k_0$  and  $b_0$  in Eq. (1) are calibrated using two reference wafers whose conductivities are known, a wafer's conductivity can be determined by measuring the output voltage under the same conditions and evaluating Eqs. (1) and (2).

The compact microwave instrument can generate microwave signals at 96 GHz (microwaves of this frequency are also referred to as millimeter waves) with power of 10 dBm. Figure 1 shows the view of the measurement where the wafer is set on the antenna in a contact fashion, i.e., the standoff distance is set to be zero.

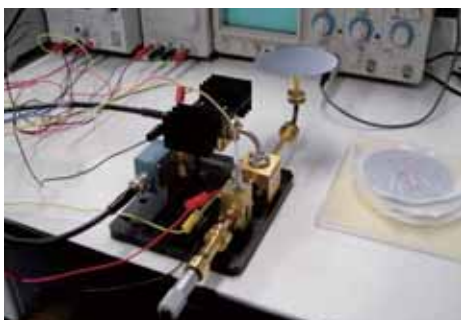


Fig. 1 Photograph of the experimental instrument with a doped GaAs wafer under measurement

Two doped GaAs wafers (Nos. 1 and 2) are used as the reference samples to calibrate the two undetermined constants in Eq. (1). Another five wafers (Nos. 3 to 7) are evaluated using the suggested method. The detailed characteristics of the wafers are shown in Table I.

Table I Characteristics of the seven doped GaAs wafers

Wafer No.	Conductivity (S/m)	Diameter (mm)	Thickness ( $\mu\text{m}$ )	Output voltage (V)
1	$2.9240 \times 10^4$	$84 \pm 0.05$	$690 \pm 25$	-0.3731
2	$5.9880 \times 10^4$	$84 \pm 0.05$	$560 \pm 25$	-0.3758
3	$3.6496 \times 10^4$	$84 \pm 0.05$	$700 \pm 25$	-0.3740
4	$4.7393 \times 10^4$	$84 \pm 0.05$	$550 \pm 25$	-0.3750
5	$7.5188 \times 10^4$	$84 \pm 0.05$	$510 \pm 25$	-0.3766
6	$1.3774 \times 10^4$	$76 \pm 0.05$	$400 \pm 25$	-0.3693
7	$2.3041 \times 10^4$	$76 \pm 0.05$	$350 \pm 25$	-0.3719

The two undetermined constants are calculated to be  $k_0 = -0.2416446$ ,  $b_0 = -0.1405282$ .

Using their output voltages shown above, the conductivities of wafers Nos. 3 to 7 are evaluated from Eqs. (1) and (2). The evaluated conductivities are compared with those measured using the Hall effect measurement (HEM) method in Fig. 2. From Fig. 2, it is found that the evaluated conductivities match well with the ones measured by the HEM method. The maximum error of evaluation is less than  $\pm 4.5\%$  of the conductivity of the wafers. The evaluation method and results are independent of the wafers' thicknesses. Therefore, a high-precision nondestructive evaluation method has been established.

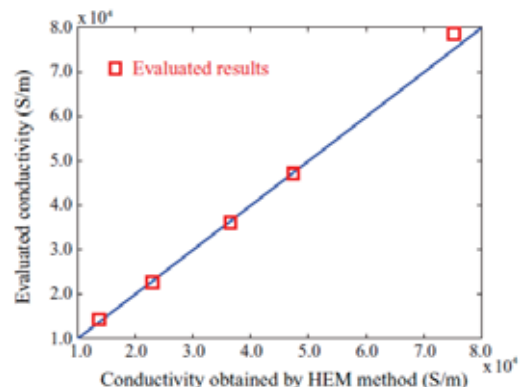


Fig. 2 Evaluated conductivities in comparison with those measured by the HEM method

1. A nondestructive method for measuring the electrical conductivity of doped GaAs wafers using a compact microwave instrument is demonstrated.
2. The measurement is independent of wafer thickness.
3. The evaluated results agree well with those obtained with the conventional HEM method, with an error less than  $\pm 4.5\%$ .

# Evaluation of mechanical property of thin films using ultrasonic waves induced by femtosecond pulse laser



Kosuke Azuchi

azuchi.kosuke@h.mbox.nagoya-u.ac.jp

Yasuyuki Morita

morita@mech.nagoya-u.ac.jp

Jang Ju

ju@mech.nagoya-u.ac.jp

Graduate School of Engineering, Nagoya University  
Furo-cho, Chikusa-ku, Nagoya 464-8603, Japan

## Abstract

Thin films of wiring for semiconductor integrated circuit and others could include the nano-scale defects and residual stress. The defects affect mechanical property of material. Therefore, to improve the performance and quality for the device, it is important to detect them. We evaluated them by measuring the elastic constant of the film. In this study, we use laser-induced ultrasound method for measuring elastic constants of the thin film. This method is non-contact and non-destructive evaluation technique. We measure the reflectivity changes of the pulsed light.

Specimens were used three metals of Au, Ag and Cu respectively were evaporated on glass wafer by EB deposition equipment. Figure 1 shows our optical setup. The pump light was modulated by acousto-optical device. The probe light reflected from sample surface and half mirror were entered into detector. The detector output was fed into a lock-in-amplifier to the modulation frequency.

Figure 2 shows elastic constant of specimen. Elastic constant of specimen was calculated by following equation:

$$E = \rho \left( \frac{2d}{\Delta t} \right)^2$$

Where E is the elastic constants,  $\rho$  is film density, d is film thickness and  $\Delta t$  is period of ultrasonic waves transmitted between sample surface and substrate interface. We consider the calculated elastic constants of specimens are affected from crystalline structure.

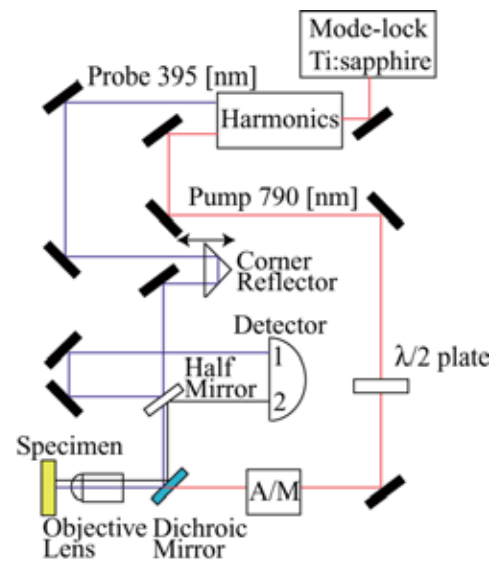


Fig.1 Optical setup

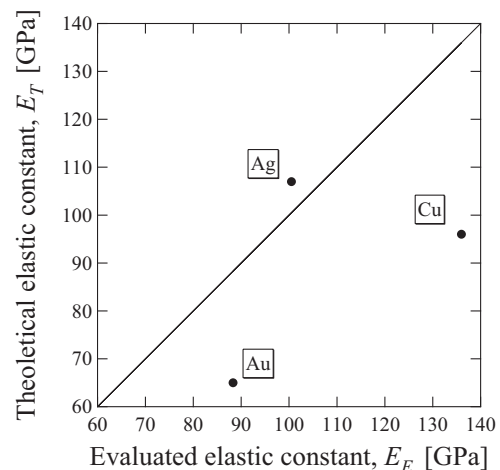


Fig.2 Comparison of elastic constants between theoretical and measured values.

## Biography

Kosuke Azuchi received the Bachelor degree in Engineering from University of Nagoya, Japan, in 2011. He is currently a student of master's course in Nagoya University, studying evaluation of mechanical property of material with femtosecond pulse laser.



# Evaluation of mechanical property of thin films using ultrasonic waves induced by femtosecond pulse laser

Kosuke Azuchi, Yasuyuki Morita, Yang Ju  
Department of Mechanical Science and Engineering, Nagoya University

## 1. Introduction

A fine integrated circuit for a semiconductor and others could include nano-scale defects and residual stress. Since the defects affect quality and performance of the devices, it is more important to detect and evaluate them. And they give an influence on mechanical property of material. Therefore we used laser-induced ultrasound method for evaluating them. Our research purpose is evaluating elastic constant of thin films.

Specimens were used three metals of Au, Ag and Cu (Fig. 1). Those metals were evaporated on glass wafer by EB deposition equipment. Table 1 shows experimental condition. Figure 2 shows our optical setup. The pump light was modulated by acousto-optical device. Then the probe light reflected from sample surface was entered into detector, whose output was fed into a lock-in-amplifier to the modulation frequency.

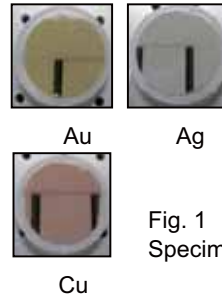


Fig. 1 Specimens

Table 1. Experimental Conditions

Wavelength [nm]	790
Power [mW]	760
Repetition Frequency [MHz]	80
Modulation Frequency [kHz]	100
<hr/>	
Pump light Wavelength [nm]	790
Pump light Power [mW]	115
<hr/>	
Probe light Wavelength [nm]	395
Probe light Power [mW]	49

## 2. Experiment

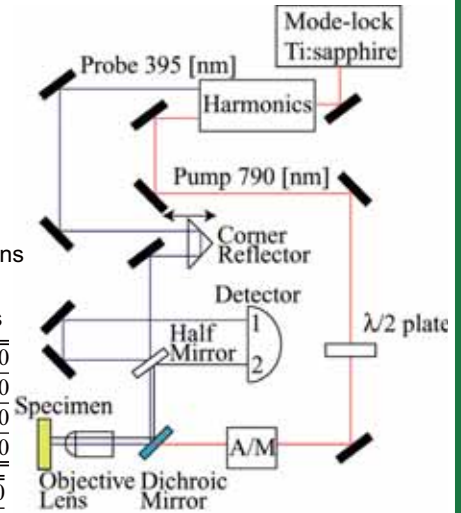


Fig. 2 Optical Setup

## 3. Results

Figure 3 (a), (b) and (c) show measuring results of Au, Ag and Cu films.

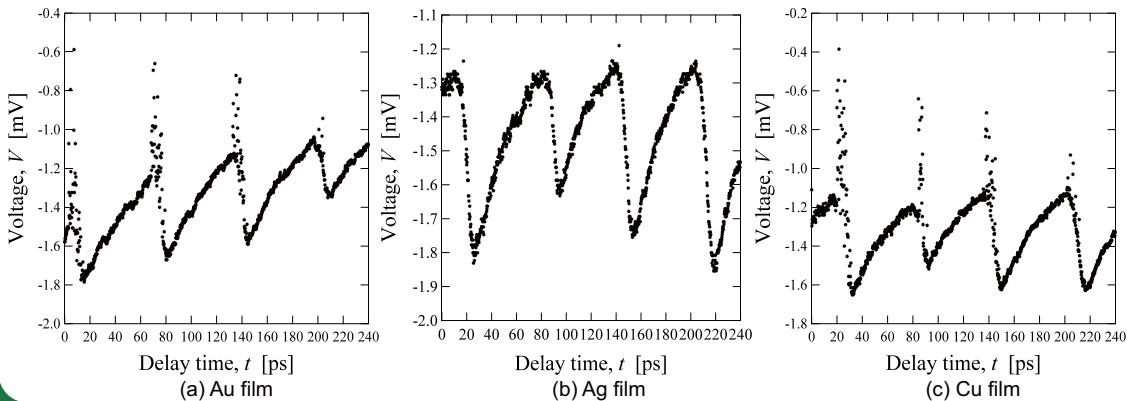


Fig. 3 Experimental results. The vertical axis is the output voltage of the detector, and the horizontal axis represents the delay time of a stage translation.

## 4. Discussion

Figure 4 shows elastic constant of specimen obtained by this technique. Elastic constant of specimen was calculated by following equation:

$$E = \rho \left( \frac{2d}{\Delta t} \right)^2$$

Where E is the elastic constants,  $\rho$  is film density, d is film thickness and  $\Delta t$  is period of ultrasonic waves transmitted between sample surface and substrate interface.

Table 2. Experimental results

	Au	Ag	Cu
Density, $\rho$ [g/cm <sup>3</sup> ]	19.32	10.49	8.96
Thickness, d [nm]	60	100	100
Average Period, $\Delta t$ [ps]	65.4	62.6	60.9
Elastic Constant [GPa]	65	107	96

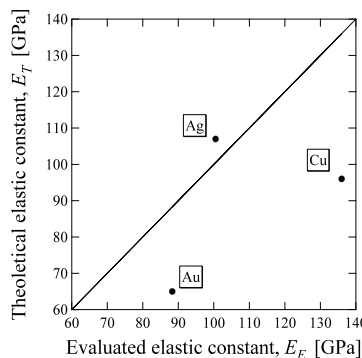


Fig. 4 Comparison of elastic constants between theoretical and measured values.

## 5. Conclusion

We observed ultrasonic waves in several metals with pump-probe method using femtosecond pulse laser. From the measuring results, we calculated the elastic constants of the metals. Of Au and Cu film was evaporated by EB deposition equipment, the decreasing of elastic constants was seen. On the other hand, the elastic constant of Ag film made by same method was increase.

# Development of fatigue crack-healing technique for metals



Tomoya KISHI

kishi.tomoya@e.mbox.nagoya-u.ac.jp

Yang JU

ju@mech.nagoya-u.ac.jp

Atsushi HOSOI

hosoi@mech.nagoya-u.ac.jp

Graduate School of Engineering, Nagoya University  
Furo-cho, Chikusa-ku, Nagoya 464-8603, JAPAN

## Abstract

Improving long-term durability and reliability of metal structures is a critical issue to decrease the environmental load from the viewpoint of reducing consumption of energy in the lifecycle. Specifically, fatigue is the main cause of failure accident in metal structures. So various methods to heal the fatigue crack have been studied. Fatigue crack healing by controlling pulsed electric current is one of them. In this method, it is revealed that the crack was closed. However, the bonding between the crack surfaces was prevented due to the oxide layer on the crack surfaces.

In this study, we improve adhesion of crack surface by surface-activated pre-coating technique, which eliminate oxide layer and coat Ni, and try to heal the fatigue crack by controlling high density electric current. Fig.1 shows the schematic view of healing technique. By using extremely adjacent probes, high-density electric current filed was caused at the crack tip

Figures 2 and 3 show the change of the crack shape before and after the application of electric current. It was observed that the microcrack was disappeared after the application of high density electric current. Crack closure is caused by the thermal expansion resulting from the high local temperature due to Joule heating by current concentration. Since the surround of expansion area is cool, the direction of expansion is restricted and toward crack closure. In this study, oxide layer preventing from bonding is eliminated, and Ni film works as the inner layer helping each crack surfaces bonding. As the results, the surface-activated pre-coating technique was successful in closing the fatigue crack and bonding the crack surfaces.

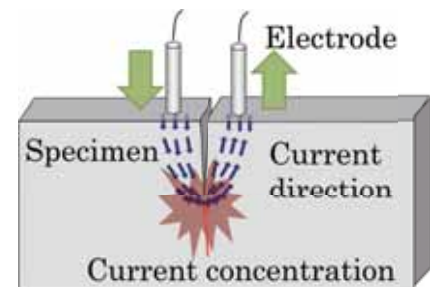


Fig.1 Schematic of applying electric current by using extremely adjacent electrode.

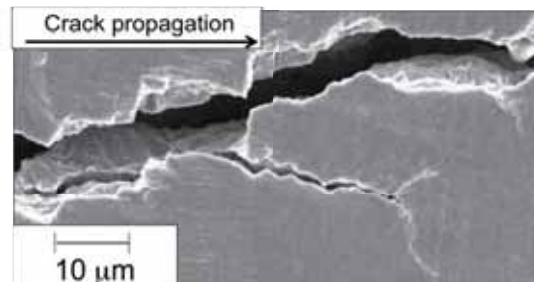


Fig.2 SEM image of fatigue crack before applying electric current.

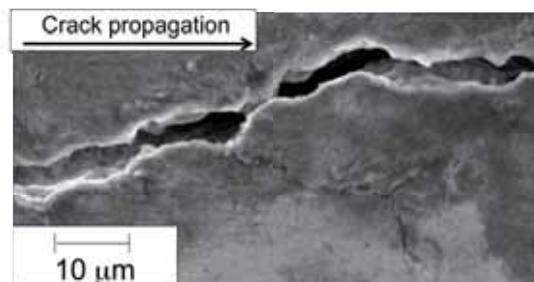


Fig.3 SEM image of fatigue crack after applying electric current.

## Biography

Tomoya Kishi received the Bachelor degree in Engineering from University of Nagoya, Japan, in 2009. He is currently a student of master's course in Nagoya University, studying the effect on healing fatigue crack in metals by applying high density electric current.

# Development of fatigue crack-healing technique for metals

T. Kishi, Y. Ju, and A. Hosoi

Department of Mechanical Science and Engineering, Nagoya University

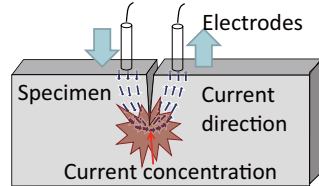
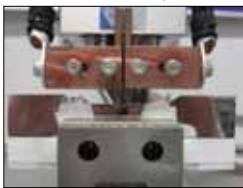
## INTRODUCTION

Improving long-term durability and reliability of structures is a critical issue to decrease the environmental load. Specifically, fatigue is the main cause of failure accident in metal structures. So various methods to heal a fatigue crack have been studied. Fatigue crack healing by controlling pulsed electric current is one of them. In this method, it is revealed that the crack was closed. However, the bonding between the crack surfaces was prevented due to the oxide layer on the crack surfaces.

In this study, we improved adhesion of crack surfaces by surface-activated pre-coating technique, which eliminates oxide layer and coat Ni, and try to heal fatigue crack by controlling high density electric current.

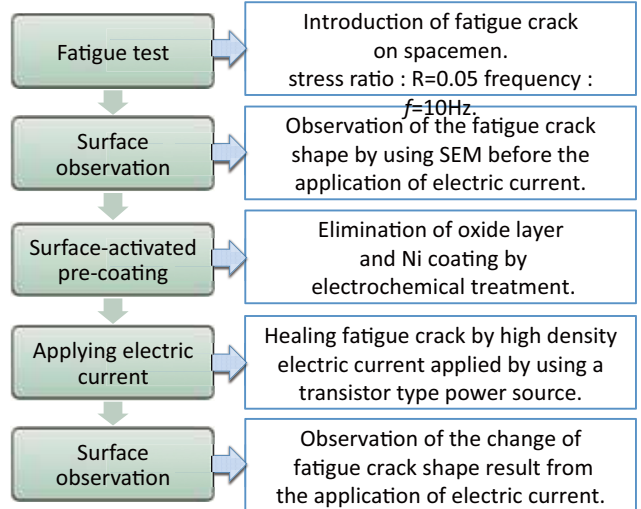
## THE APPLICATION OF ELECTRIC CURRENT

By using adjacent electrodes, high-density electric current filed was induced at the crack tip due to electric current concentration.

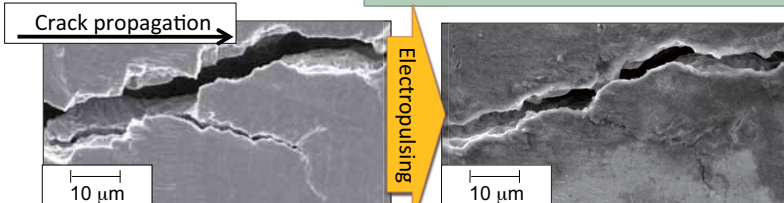


## EXPERIMENTAL PROCEDURES

Austenite stainless steel SUS316 was used as the experimental material. The dumbbell-shaped specimen was employed.



## EXPERIMENTAL RESULTS



**Experimental conditions**  
 $\sigma_{\text{max}} = 180 \text{ [Mpa]}$ ,  $\Delta K = 24.42 \text{ [MPa} \cdot \text{m}^{1/2}]$   
 $I'_{\text{max}} = 5730 \text{ [A]}$ ,  $t = 1.0 \text{ [msec]}$   
 $I'_{\text{max}} = 5860 \text{ [A]}$ ,  $t' = 1.0 \text{ [msec]}$

Spherical materials were formed on the crack surfaces after the application of high density electric current. Each Crack surfaces was connected by these materials.

And then, high density electric current was applied again. The crack was one-tenth closure and bonding of each crack surfaces after the second application.

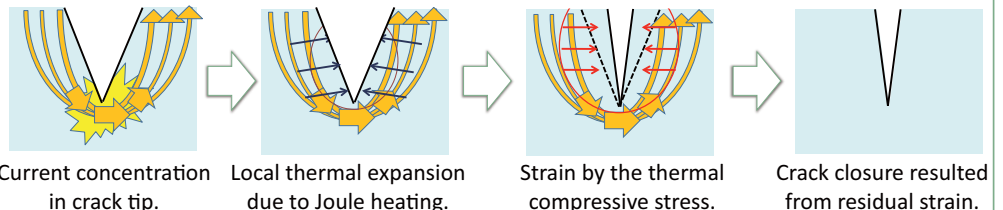
**Experimental conditions**  
 $\sigma_{\text{max}} = 180 \text{ [Mpa]}$ ,  $\Delta K = 25.08 \text{ [MPa} \cdot \text{m}^{1/2}]$   
 $I'_{\text{max}} = 5880 \text{ [A]}$ ,  $t = 1.0 \text{ [msec]}$

Left figures show the change of the crack shape before and after the application of electric current by SEM. It was observed that the microcrack was healed after the application of high density electric current.

## DISCUSSIONS

### Closure of fatigue crack

Crack closure is caused by the thermal expansion resulting from the high local temperature due to Joule heating by current concentration. Since the surround of expansion area is cool, the direction of expansion is restricted and toward crack closure.

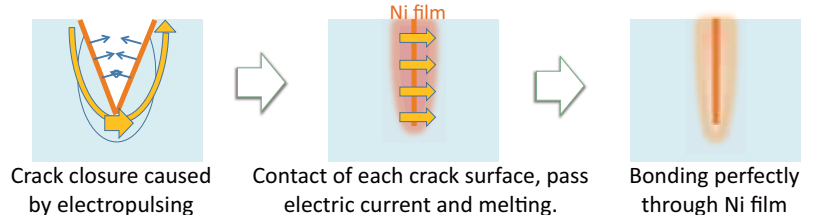


### Bonding of each crack surfaces

Surface-activated pre-coating is effective to bond crack.

Eliminate oxide layer  
Coat Ni film

Oxide layer preventing from bonding is eliminated, and Ni film works as the inner layer helping each crack surfaces bonding.



## CONCLUSIONS

The closure of fatigue crack, the healing of microcrack and the bonding of each crack surfaces was realized after the application of high density current and eliminating oxide layer by surface-activated pre-coating in SUS316. From these results, it is expected that the crack growth rate is suppressed.

# Study of copper oxide nanowires generated by stressmigration at the selectivity metal deposits



Naoki KOJIMA

kojima.naoki@g.mbox.nagoya-u.ac.jp

Yang JU

ju@mech.nagoya-u.ac.jp

Department of Mechanical Science and Engineering, Nagoya University  
Furo-cho, Chikusa-ku, Nagoya 464-8603, Japan

## Abstract

Copper oxide nanowires have been found having excellent properties, and may be used for NEMS or MEMS. To apply nanowires to practical device, a lot of nanowire pattern is needed. In this study, we evaporated metal film on Si substrate in micro region and evaluated the nanowires generated on the micro pattern.

Experimental conditions are set below. A 60 nm thick Ta layer was deposited directly on the Si substrate to serve as the adhesive layer and 200, 400, 700 nm thick copper layer was deposited on the Ta layer by the electron beam evaporation. The size of pattern 5, 10, 15  $\mu\text{m}$  were created. Samples were heated in air at 613 K, and the time of heating was 2h, 5h, 9h, 18h.

A lot of micro pattern can be created. Nanowires are generated on the square-patterns by heating at 613 K. But there are few nanowires on the circle-pattern at the same condition.

To confirm the relationship between nanowires growth and experimental conditions, samples are observed by SEM. The minimum size of square pattern which can generate nanowires is 5  $\mu\text{m}$ . Density and length of nanowires changed by the size of pattern, heating time and Cu film thickness. Nanowires can grow by extending heating time, but varied little after 9h. The size of pattern is bigger, the length and density of nanowires become larger. Cu film is thicker, the length and density of nanowires become larger.

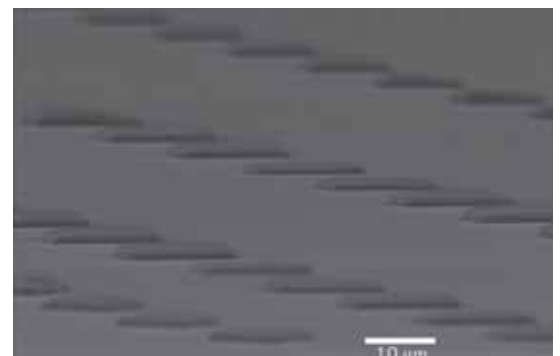


Fig.1 SEM images of metal patterns

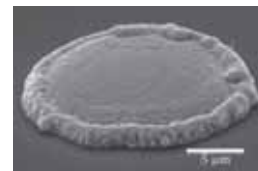


Fig.2 SEM images of circle pattern after heating for 5h

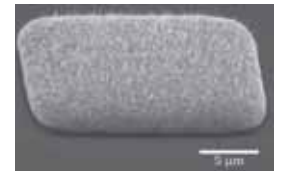


Fig.3 SEM images of square pattern after heating for 5h

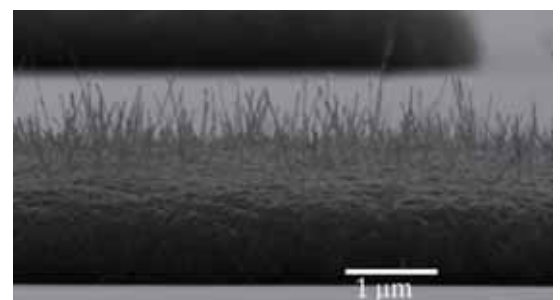


Fig.3 SEM images of nanowires on the 15-mm-square pattern after 5h heating

## Biography

Naoki KOJIMA received the Bachelor degree in Engineering from University of Nagoya, Japan, in 2012. He will become a student of master's course in Nagoya University.

# Study of copper oxide nanowires generated by stressmigration at the selectivity metal deposits

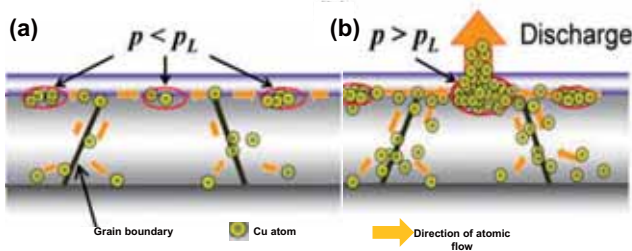


Naoki KOJIMA, Mingji CHEN and Yang JU  
 Department of Mechanical Science and Engineering, Nagoya University  
 Furo-cho, Chikusa-ku, Nagoya 464-8603, Japan

## Introduction

Semiconductor nanowire has excellent properties and may be used as new functional element especially in NEMS or MEMS. In this paper we created nanowires by stressmigration which depend on hydrostatic stress in sample. Copper oxide is a p-type semiconductor which can react with gas such as CO. So if we can growth nanowires on the sensing element, we can make higher precision gas sensor than usual one. To apply nanowires to practical sensor, a lot of nanowire pattern is needed. In this study, we report the fabrication of copper oxide nanowires on the micro metal pattern through heating sample in air.

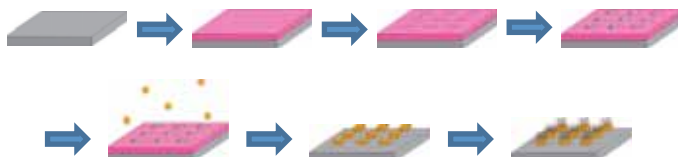
## Growth Principle of the Method



$p$ : interfacial compressive stress;  $p_L$ : compressive stress of lowest limit for nanowires formation

Stressmigration is a phenomenon of atoms migration driven by the gradient of hydrostatic stress. Atom diffuse a region of higher compressive stress toward that of lower stress. When Sample is heated, Cu film is subjected to thermal stress because of the mismatch in thermal expansion coefficients between the metals. And then Cu atoms diffused and migrated toward some site on the top face of Cu film. If the compressive hydrostatic stress induced by the accumulation of Cu atoms at interface between the oxide layer and the Cu film attain a critical value, Cu atoms penetrated the oxide layer via any weak spot to form nanowires.

First, two-layers photoresist were spin-coated on silicon wafer and then various pattern were written in  $\mu$ -PG. A 60 nm thick Ta layer was deposited directly on the Si substrate to serve as the adhesive layer and 200, 400, 700 nm thick copper layer was deposited on the Ta layer by the electron beam evaporation. The final lift-off was carried out by dissolving the remaining photoresist in acetone. Pattern whose size is 5, 10, 15  $\mu\text{m}$  was able to be created by these process. Samples were heated in air at 613 K by a ceramic heater. In this paper time of heating was 2h, 5h, 9h, 18h. After heating, copper oxide nanowires were generated on the pattern, and we measured the density and length of nanowires.



## Results and Discussion

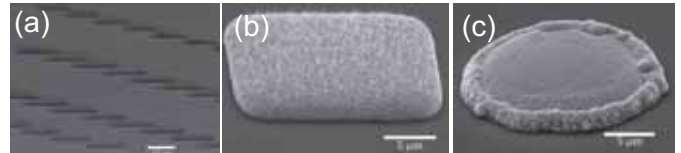


Fig.1. (a)SEM image of metal pattern, (b)SEM image of square pattern after heating for 5h, (c)SEM image of circle pattern after heating for 5h.

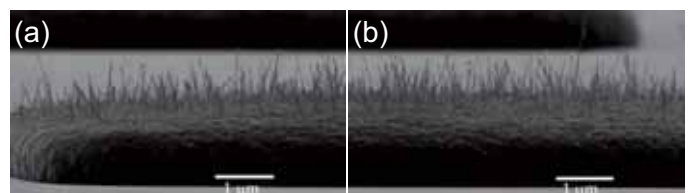


Fig.2. SEM images of nanowires on the 15- $\mu\text{m}$ -square pattern after 5h heating, (a)the edge of pattern, (b)the center of pattern.

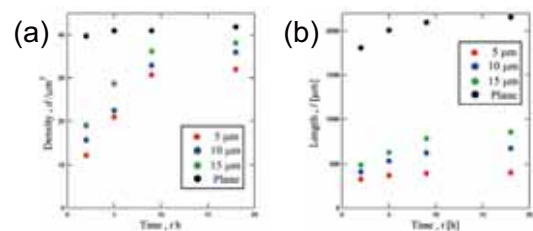


Fig.3. (a)Relation between Time and Density(Cu film thickness;700 nm), (b)Relation between Time and Length(Cu film thickness;700 nm).

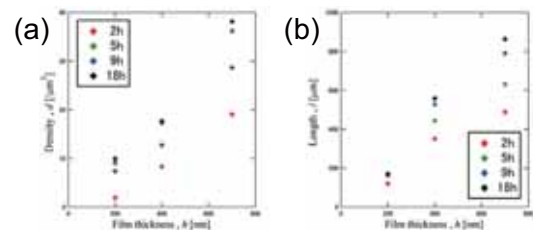


Fig.4. (a)Relation between Cu film thickness and Density(15- $\mu\text{m}$ -square pattern), (b)Relation between Cu film thickness and Length(15- $\mu\text{m}$ -square pattern).

Fig.1 shows the result of pattern after heating. Nanowires on the square pattern grew well, but few nanowires grew on the circle pattern at the same condition. Fig.2 shows the appearance nanowires on the square pattern. From that there wasn't a great difference in length and density between the edge and center. From Fig.3 nanowires could grow by extending heating time, but varied little after 9h. And the size of pattern was bigger, the length and density of nanowires became larger. From Fig.4 Cu film was thicker, length and density of nanowires became larger.

- We can growth copper oxide nanowires on the 5- $\mu\text{m}$ -square pattern. But size of pattern was small, nanowires didn't grow much.
- Density and length of nanowires didn't change over 9h-heating
- Copper film is thicker, density and length of nanowires become larger.

# Development of Evaluation Technique of Electrical Properties Using Microwave Atomic Force Microscope



Takahiro NAKASHIMA

nakashima.takahiro@g.mbox.nagoya-u.ac.jp

Atsushi HOSOI

hosoi@mech.nagoya-u.ac.jp

Yang JU

ju@mech.nagoya-u.ac.jp

Department of Mechanical Science and Engineering, Nagoya University  
Furo-cho, Chikusa-ku, Nagoya 464-8603, Japan

## Abstract

The microwave response of materials is directly relative to the electrical properties of materials. However, the microwave response of materials is severely affected by the standoff distance change between the tip of the probe and the sample. Microwave atomic force microscope (M-AFM) can evaluate electrical properties by measuring microwave near-field signal and control the standoff distance by measuring the atomic force. In this study, we confirm that the microwave response imaging isn't dependent on the surface shape. Fig.1 shows the schematic diagram of the M-AFM system.

The M-AFM probe was fabricated by MEMS process. M-AFM probe consists of AFM cantilever integrated with a parallel plate waveguide. To ensure effective transmission of microwave, gallium arsenide (GaAs) was used as the substrate.

In order to confirm that microwave response imaging is not dependent on the surface shape, two difference surface shape samples were measured by original M-AFM system. Sample A had convex Au patterns, and sample B had concave Au patterns. These two types of samples are different to the shapes, but the same to the pattern of electrical properties.

As a result, Fig.2 and Fig.3 showed measurement result of sample A, and Fig.4 and Fig.5 showed measurement result of sample B. By comparing with these results, the microwave response imaging indicated the same tendency despite of the difference of the surface shapes. So it is indicated that the microwave response imaging obtained by M-AFM is not dependent on the surface shape of materials.

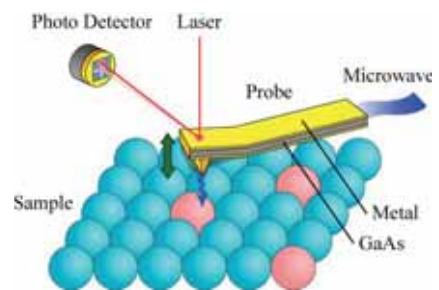


Fig.1 Schematic diagram of the M-AFM system

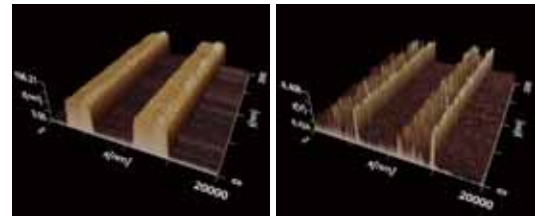


Fig.2

Fig.3

Fig.2 3D topography of Sample A

Fig.3 3D microwave image of Sample A

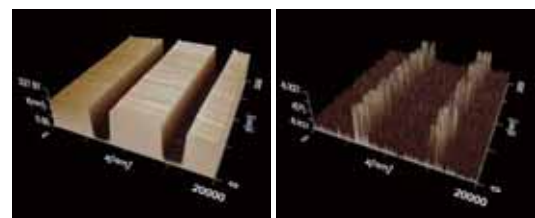


Fig.4

Fig.5

Fig.4 3D topography of Sample B

Fig.5 3D microwave image of Sample B

## Biography

Takahiro Nakashima is a senior student in the department of Mechanical Science and Engineering, Nagoya University.

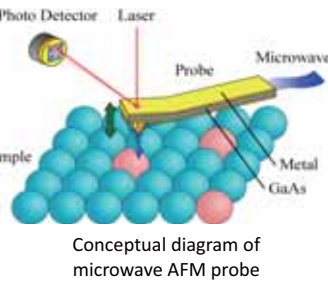
# Development of Evaluation Technique of Electrical Properties Using Microwave Atomic Force Microscope



T. Nakashima, A. Hosoi, and Y. Ju  
Department of Mechanical Science and Engineering, Nagoya University

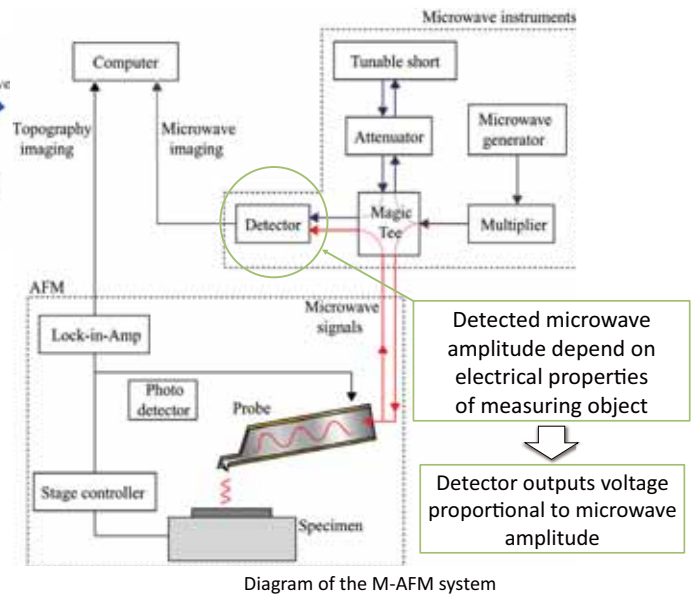
## Introduction

With development of nanotechnology, evaluation technique for electrical properties in local area of materials has become a great need. To satisfy such requirement, we have proposed a microwave atomic force microscope (M-AFM). M-AFM can evaluate electrical properties by measuring microwave near-field signal and control the standoff distance by measuring the atomic force.

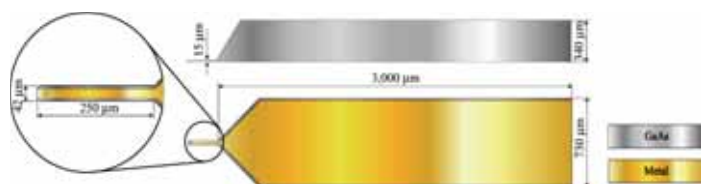


The microwave response of materials is directly relative to the electrical properties of materials. However, the microwave response of materials is severely affected by the standoff distance change between the tip of the probe and the sample. To solve this problem, we have developed M-AFM probe and system. In theory, the microwave response imaging is not dependent on the surface shape using the M-AFM. In this study, we confirm that the microwave response imaging is not dependent on the surface shape.

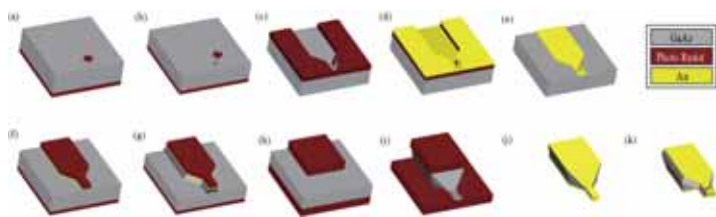
In order to confirm the theory, the microwave response of two different surface shape types of Si-Au grating samples were measured by M-AFM. As a result of comparing two measured results, it is indicated that the theory is valid.



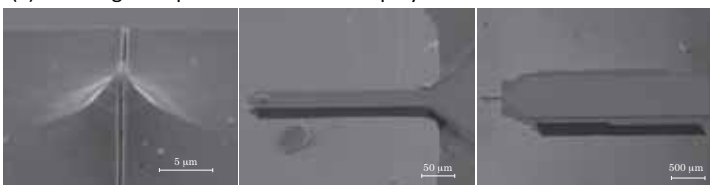
In order to confirm that M-AFM can actually maintain a constant standoff distance, two difference surface shape samples are measured. One has convex Au patterns (Sample A), and the other has concave Au patterns (Sample B). These two types of samples are different to the shapes, but the same to the pattern of electrical properties. So if M-AFM can actually maintain a constant standoff distance, the microwave scanning results of these two samples show the same tendency. The M-AFM can sense the topography and microwave image of materials in one scanning process simultaneously. These results indicate that M-AFM can discriminate electrical properties of the sample.



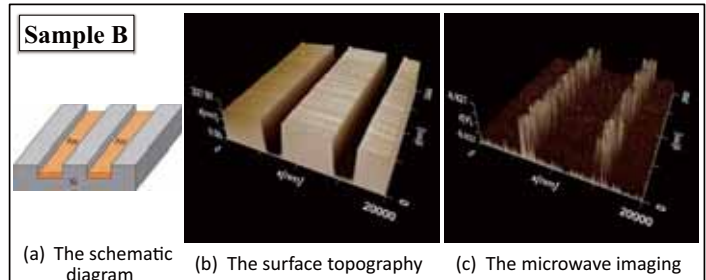
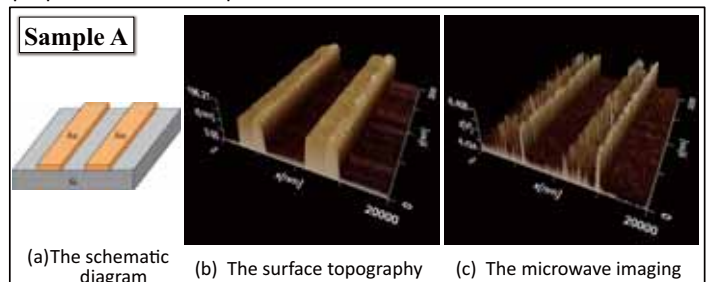
The microwave atomic force microscope (M-AFM) probe consists of AFM cantilever integrated with a parallel plate waveguide. To ensure effective transmission of microwave, gallium arsenide (GaAs) was used as the substrate.



- Patterning of the etching mask for the probe tip fabrication
- Forming the tip of the probe by wet etching
- Patterning of the stencil mask to form the waveguide on the top surface
- Coating the metal film on the top surface
- Forming the waveguide by lift-off process
- Patterning of the etching mask for cantilever fabrication
- Forming the cantilever of the probe by wet etching
- Patterning of the etching mask on back side for holder fabrication
- Forming the holder of the probe by wet etching
- Coating metal film on the bottom surface to form the waveguide
- Forming the open structure at the tip by FIB fabrication



(a) SEM image of the tip (b) SEM image of the cantilever (c) SEM image of the M-AFM probe



By comparison the results between sample A and sample B, the two microwave imaging show the same tendency despite of the difference of the surface shapes. Therefore, it is indicated that the microwave response imaging obtained by M-AFM is not dependent on the surface shape of the materials.

# Study on detection of delamination in unidirectional CFRP by microwave reflectometry



Yuhei Yamaguchi

yamaguchi.yuhei@e.mbox.nagoya-u.ac.jp

Yang Ju

ju@mech.nagoya-u.ac.jp

Atsushi Hosoi

hosoi@mech.nagoya-u.ac.jp

Department of Engineering, Nagoya University  
Furo-cho, Chikusa-ku, Nagoya 464-8603, Japan

## Abstract

Carbon fiber reinforced plastic (CFRP) composites have higher specific strength and specific stiffness than existing metal materials. However, the presence of defects as delamination may significantly affect the strength and stiffness of CFRP. Thus, the detection of delamination in CFRP is a great issue.

From the reason described above, we attempted to detect defects in CFRP by noncontact, rapid and high sensitive microwave reflectometry utilizing the focusing mirror sensor (Fig. 1.). Microwave reflectometry is a method to detect defects by measuring the phase variation of reflected wave from the sample. Besides, a focusing mirror sensor has high resolution, high sensitivity and long standoff distance. However, the resolution and sensitivity of the sensor for the delamination in CFRP depends on the standoff distance and frequency.

Thus, in this study, the experiments were conducted to decide an optimal frequency and standoff distance for the detection of delamination in CFRP utilizing the focusing mirror sensor. The unidirectional CFRP inserted circular kapton films whose thickness is 100  $\mu\text{m}$  internally instead of delamination was applied as a sample. Additionally, the detection of defects utilizing the focusing lens sensor (Fig. 2) and the waveguide sensor (Fig. 3) was conducted in each optimal experiment condition.

Figure 4 showed the result of imaging of the phase variation utilizing the focusing sensor. The great phase variation in the center of this image indicated the presence of defects.

## Biography

Yuhei Yamaguchi attends bachelor degree in Nagoya University of department of engineering.



Fig.1 The focusing mirror sensor



Fig.2 The focusing lens sensor



Fig.3 The waveguide sensor

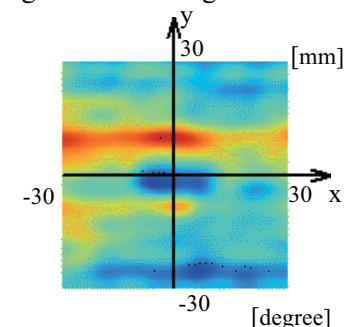


Fig.4 The imaging of phase variation

# Study on detection of delamination in unidirectional CFRP by microwave reflectometry

Yuhei Yamaguchi, Yang Ju\*, Atsushi Hosoi

Department of Mechanical Science and Engineering, Nagoya University  
Furo-cho, Chikusa-ku, Nagoya 464-8603, Japan

\*: ju@mech.nagoya-u.ac.jp



Carbon fiber reinforced plastic (CFRP) composites have higher specific strength and specific stiffness than existing metal materials. However, the presence of defects as delamination may significantly affect the strength and stiffness of CFRP. Thus, the detection of delamination in CFRP is a great issue.

In this study, we attempted to detect defects in CFRP by noncontact, rapid and high sensitive microwave reflectometry utilizing a focusing mirror sensor (Fig. 1(a)) which has high resolution, high sensitivity and long standoff distance.

Additionally, the detection of defects was conducted utilizing a focusing lens sensor (Fig. 1(b)) and a waveguide sensor (Fig. 1(c)).

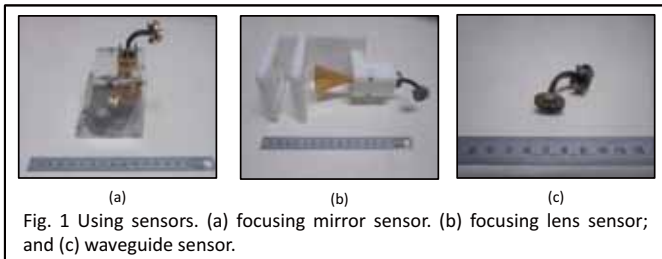


Fig. 1 Using sensors. (a) focusing mirror sensor. (b) focusing lens sensor; and (c) waveguide sensor.

In this study, unidirectional CFRP inserted circular kapton film whose thickness is 100  $\mu\text{m}$  internally instead of delamination was applied as a sample.

Three experiments utilizing the focusing mirror sensor were conducted.

- At first, metal plates was put under the CFRP sample (Fig. 2). With different frequency, the sample was scanned and phase variation was measured. After that, optimal frequency was decided from sensitivity for metal plates.
- With different standoff distance, the sample was scanned on defect area and phase variation was measured. After that, optimal standoff distance was decided from sensitivity for film.
- In optimal condition decided above, 2D scan of the sample was conducted around defects area. After that, 2D scan utilizing other sensors was conducted.

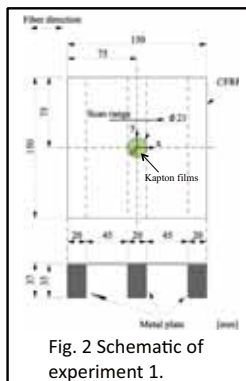


Fig. 2 Schematic of experiment 1.

Figure 3(a) showed the result of experiment 1. To decide optimal frequency, the relation between frequency and signal-noise ratio was showed in Fig. 3(b). Frequency  $f=75\text{GHz}$  that had the highest signal-noise ratio was decided the optimal frequency.

Figure 4(a)~(e) showed the results of experiment 2. To decide optimal standoff distance, the relation between standoff distance and signal-noise ratio was showed in Fig. 4(f). Standoff distance  $l=11.8\text{mm}$  was decided the optimal standoff distance.

Figure 5(a)~(c) showed the results of experiment 3 that imaged the phase variation utilizing the focusing mirror sensor ( $f=75\text{GHz}$ ,  $l=11.8\text{mm}$ ), the focusing lens sensor ( $f=75\text{GHz}$ ,  $l=42.1\text{mm}$ ) and the waveguide sensor ( $f=75\text{GHz}$ ,  $l=2.8\text{mm}$ ), respectively.

Figure 5(a) and 5(b) indicated that the focusing mirror and lens sensor could detect film. The focusing mirror and lens sensor had high sensitivity because of focusing microwaves at depth of the film inserted in the specimen. Therefore, film could be detected sensitively.

On the other hand, as Fig. 5(c) showed, the waveguide sensor detected the fiber orientation in surface more sensitively than the film in the specimen due to attenuation of microwaves.

These results indicated that the detection method focusing microwave had the potential of detecting the delamination in CFRP.

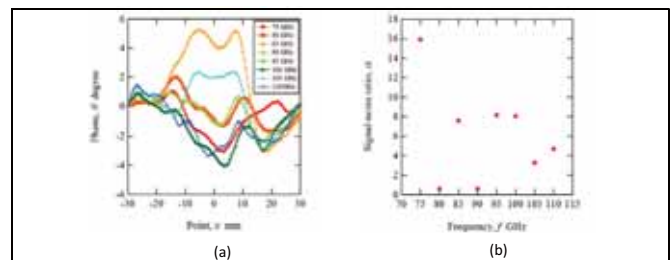


Fig. 3 Results of experiment 1. (a) frequency  $f=75\text{GHz}\sim 110\text{GHz}$ . (b) relation between frequency and signal-noise ratio.

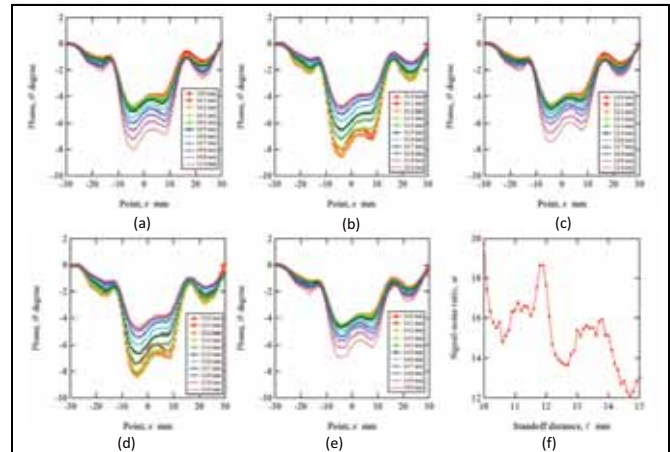


Fig. 4 Results of experiment 2. (a) standoff distance  $l=10\text{mm}\sim 11\text{mm}$ . (b)  $l=11\text{mm}\sim 12\text{mm}$ . (c)  $l=12\text{mm}\sim 13\text{mm}$ . (d)  $l=13\text{mm}\sim 14\text{mm}$ . (e)  $l=14\text{mm}\sim 15\text{mm}$ ; and (f) relation between frequency and signal-noise ratio.

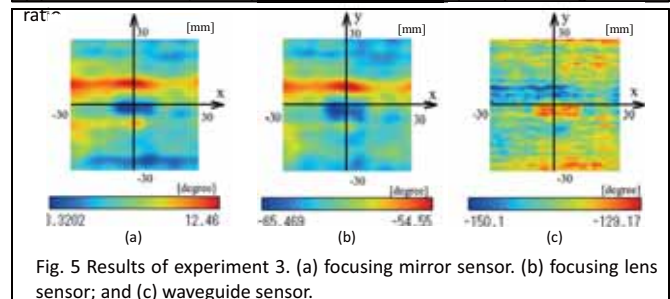


Fig. 5 Results of experiment 3. (a) focusing mirror sensor. (b) focusing lens sensor; and (c) waveguide sensor.

- The waveguide sensor could detect the fiber orientation sensitively.
- The focusing mirror sensor ( $f=75\text{GHz}$ ,  $l=11.8\text{mm}$ ) and the focusing lens sensor ( $f=75\text{GHz}$ ,  $l=42.1\text{mm}$ ) could detect film whose thickness is  $100\mu\text{m}$  in unidirectional CFRP.
- The detection method focusing microwave had the potential of detecting delamination in CFRP.

# What Is the Adequate Feature of a Robot for Children with Autism in Robot-Assisted Therapy?



Jaeryoung LEE  
lee.jaeryoung@a.mbox.nagoya-u.ac.jp

Hiroki TAKEHASHI  
h.takehashi@esi.nagoya-u.ac.jp

Chikara NAGAI  
nagai@coe.mech.nagoya-u.ac.jp

Goro OBINATA  
obinata@mech.nagoya-u.ac.jp

Graduate School of Engineering, Nagoya University  
Furo-cho, Chikusa-ku, Nagoya 464-8603, JAPAN

Autism has the features of reciprocal social interaction associated with impairment in communication skills and stereotyped behavior. Recently, various robots have been used in research to mediate interaction for children with autism. Previous studies suggest that social interaction and communication skills of autistic children have improved by playing with therapeutic robots.

Social skills	Questionnaire
Eye contact	Does he or she make eye contact?
Gesture	Does he or she use gestures to express his or her feeling?
Facial expression	Does expression on his or her face match what he or she is saying?
language	Does he or she use language to express his or her feeling?

Fig. 1 Section 1 on the questionnaire: the degree of social skill which their child is capable of

However, the physical features of many therapeutic robots for autistic children have not been tested as to their ability to improve social skills. Moreover, previous work has not examined the interaction between autistic children and robots with verbal functions, and therefore has only focused on non-verbal communication skills.

Therefore, we have conducted two studies in order to examine these issues. Study 1 (Fig.1) explores the relationship between the features of interactive devices that autistic children usually play with and the development of the children's social skills. Study 2 (Fig.2 and Fig.3) investigates the possibility of robots with verbal functions affecting the communications skills of autistic children.



Fig. 2 Facial expression game, in which the prompts make the children exhibit 4 particular facial expressions.

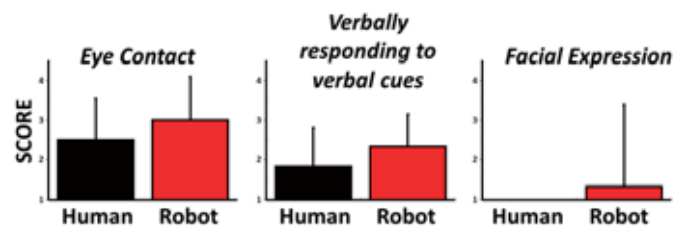


Fig. 3 The mean of eye contact, responding to verbal cues and facial expression game score in the experiment with robot are higher than those with human.

## Biography

Jaeryoung Lee received the Bachelor degree in Mechanical engineering from Pusan National University in 2009. She is currently a Master student at Nagoya University, focusing on the studies of Human Robot Interaction in Autism therapy.

# What Is the Adequate Feature of a Robot for Children with Autism in Robot-Assisted Therapy?



Jaeryoung Lee<sup>1</sup>, Hiroki Takehashi<sup>2</sup>, Chikara Nagai<sup>1</sup>, Goro Obinata<sup>2</sup>

<sup>1</sup>Nagoya University, <sup>2</sup>EcoTopia Institute, Nagoya, Japan

## What is Autism?

- repetitive behaviors, language delays, obsessive interests
- to avoid looking at human faces
  - prefer looking at objects rather than human faces

## Robot-assisted Autism Therapy

To help autistic children better understand social cues

- Simple appearance & Movement, Repetitive Play
- Predictable

\* The physical features of many robots have not been tested as to their ability to improve social skills

### STUDY 1

the features of TOYS that autistic children usually play with

the development of the children's social skills

### STUDY 1 - Procedure

\* According to some research, play materials (e.g., toys) contribute to the social development of children.

## Participants

- 15 parents of children with autism (ages 6 to 15)

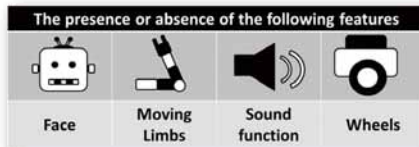
### Section 1

The degree of social skill which their child is capable of



### Section 2

The features of a toy which their child prefer to play with in daily life



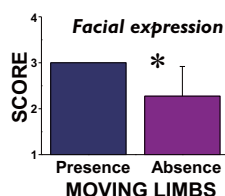
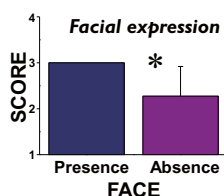
### STUDY 1 - Results

\* To examine the relationship between the presence or absence of toy's features and each aspect of social skills, we conduct a Mann-Whitney test.

■ Toys with faces facilitate the social skill of facial expression more often than toys without ( $p < .05$ ). On the other hand, the presence of a face has no influence on other skills ( $ps > .18$ ).

■ Toys with moving limbs also facilitates facial expression ( $p < .05$ ), but has no influence on other skills ( $ps > .55$ ).

■ Sound function and wheels do not influence any of the communication skills ( $ps > .18$ ).



\* Previous works have not examined the interaction between autistic children and robots with verbal functions

### STUDY 2

robots with verbal functions

affecting

the social skills of autistic children

### STUDY 2 - Procedure

## Participants

- 6 children with low-functioning autism (ages 7-12)

## Trials

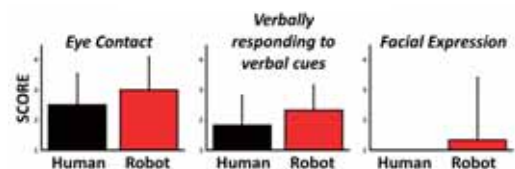
- Two trials with different prompters; HUMAN/ROBOT
- To engage in a facial expression game
- Prompters make the children exhibit 4 facial expressions



## Measurements

- Making eye contact toward the prompter
  - Responding to verbal cues from the prompter
  - Facial expression game score
- All the trials were observed by the experimenter in real-time.

### STUDY 2 - Results



## Results

- The result of eye contact indicates that autistic children were more interested in the robot than human.
- The result of responding to verbal cues demonstrates the children followed the instructions of the robot's verbal communication more than the human's.
- The score of the facial expression game shows the children achieved better results following the prompting of the robot than the human.

## Conclusion

The presence of faces and moving limbs on robots

have a positive effect on

Facial expression therapy in autistic children

Prompting of facial expression by robots with verbal function

can elicit greater response

than prompting by humans

## Future direction

- Further data collection from low-functioning autistic subjects to high functioning autistic subjects in order to validate these findings for general use.

# Sensory perception by Electrical Stimulation



Miyako BANNO

[banno.miyako@g.mbox.nagoy-u.ac.jp](mailto:banno.miyako@g.mbox.nagoy-u.ac.jp)

Goro OBINATA

[obinata@mech.nagoya-u.ac.jp](mailto:obinata@mech.nagoya-u.ac.jp)

Chikara NAGAI

[nagai@coe.mech.nagoya-u.ac.jp](mailto:nagai@coe.mech.nagoya-u.ac.jp)

School of Engineering, Nagoya University  
Furo-cho, Chikusa-ku, Nagoya 464-86-3, JAPAN

## Abstract

Our research aims to develop a new electric stimulation device to present information to humans, especially, upper limb prosthesis users. The performance of upper limb prosthesis improves these days, and the upper limb prosthesis which moves by user's intention is developed. However, the upper limb prosthesis doesn't have artificially sense tactile feedback.

We proposed feedback method using electric stimulation for upper limb prosthesis users. When a suitable current flows through a part of body, people can distinguish directions of the current. Our research investigated that people can distinguish directions of two currents.

We used to four electrodes and 2channel currents to present several combination patterns (Fig.1). The waveform is rectangular pulse, duty ratio is 5%, and frequency is 2000Hz (The frequency is not painful). The results of the first experiment show that the subjects couldn't distinguish directions of two currents which is the same frequency. Next, we experimented with 2000Hz and 2001Hz. The subjects could distinguish directions of two currents which are different to frequency. Moreover, the subjects could distinguished the change of one current frequency (another frequency is fasten to 2000Hz). By changing frequency, two currents interfere, and the beat frequency occurs. It was verified that the proposed method accomplished presentation of 4bit resolution information using electric stimulation without changing a voltage.

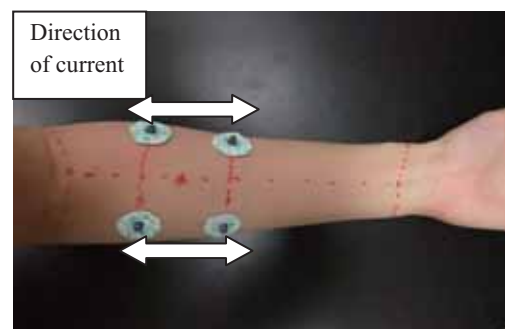


Fig.1 the place of four electrodes and direction of flowing currents

Table.1 direction of currents and paten number

①	②	③	④
→	→	←	←
→	←	→	←

Table.2 one of the results of experiment using two frequencies

Subject1		Subjects answer			
		①	②	③	④
flowing currents pattern	①	80	20	0	0
	②	0	100	0	0
	③	0	0	100	0
	④	0	0	0	100

[%]

## Biography

Miyako Banno is currently a school of engineering department in Nagoya University. She is majoring in human engineering.

# Sensory Perception by Electrical Stimulation

(1)Miyako Banno, (1)Goro Obinata, (1)Chikara Nagai, (1)Hitoshi Hirata

(1) School of Engineering, Nagoya University

(2) Department of Mechanical Science & Engineering, Graduate School of Engineering, Nagoya University

(3) Global COE Micro-Nano Mechatronics, Graduate School of Engineering, Nagoya University

(4)Department of Hand Surgery, Graduate School of Medicine, Nagoya University

March, 2012

## Purpose

We have already designed many types of upper limb prosthesis with electric actuators to perform several tasks. However, we have not achieved dexterous handling like human hands yet. One of the reasons is lack of sensory feedback of tactile information to the user. In the most contexts around upper limb prosthesis, the users can use the visual feedback with their eyes but cannot obtain any tactile information because of the absence of their hands. There exist several tactile sensors which can collect simultaneously the several kinds of tactile information like human tactile receptors. However, there does not exist the direct way for feeding back the signals of tactile sensors to the users.

Our research aims to develop a new electric stimulation device to present information to humans, especially, upper limb prosthesis users.

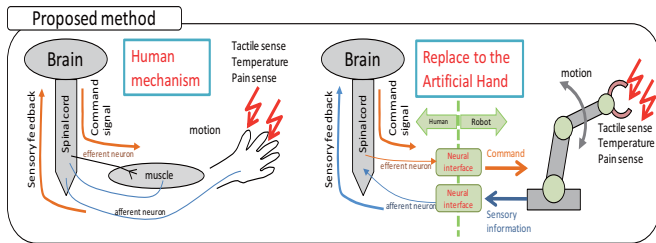
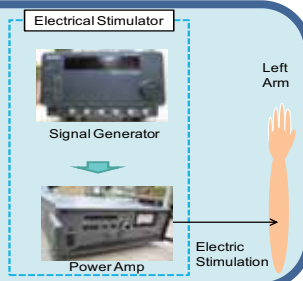


Fig.1 sensory feedback system

## Experiment

### device

We constructed an experimental setup consisting of surface electrodes, voltage amplifier and electrical function generator. Using the setup, we can provide any voltage pattern of electrical signals to the subjects through the surface electrodes.



### experiment1

In the first experiment, we investigated a relationship between duty ratio and sensory perception. We used a rectangular pulse. The frequencies were 2000Hz and change duty ratio from 3% to 15%. Each subject provided current of centripetal or opposite direction at random. They evaluated the difference of the stimulation while the different duty ratios were provided, and check the accuracy ratio.

### experiment2

We investigated sensory perception with two channel currents. The duty ratio was 5%. Each subject provided currents of centripetal or opposite directions at random. They drew the place of the stimulation and check the strength of the sense.



Fig.2 the place of four electrodes direction of two currents

### experiment3

We investigated sensory perception with two channel currents which are different to frequency (2000Hz and 2001Hz). Each subject provided currents of centripetal or opposite directions at random.

## experiment4

We investigated the change of frequency. One frequency was fasten to 2000Hz, another changed from 2000Hz to 2010Hz.

## Result

### experiment1

All subjects to obtain the highest accuracy rate at 5% duty cycle. Accuracy rate is greater than 5% of the duty ratio will be reduced, in identifying a polarity change is considered difficult to identify larger the duty ratio. When the duty ratio of 3%, accuracy rate reduce so that current flow time will be shortened.

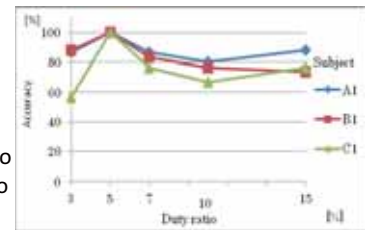


Fig.3 Experimental results: Duty ratio vs. Accuracy

### experiment2

The place of the stimulation present obvious difference. The result suggests that the directions can be distinguished.

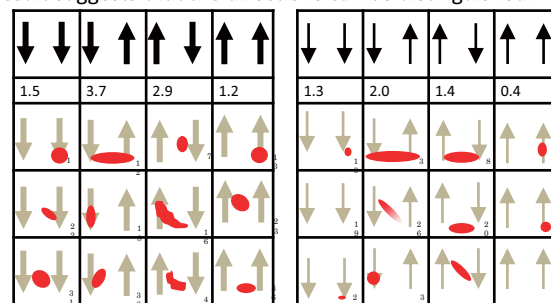


Fig.4 A experimental results: the place of stimulation with two currents

### experiment3, and4

In two experiment, four subjects distinguished higher than 90percents. The figure is adequate high.

Table.1 Experimental results: accuracy rate changing directions

Subject	s1	s2	s3	s4	s5	All
Accuracy rate	95.0	90.0	80.0	95.0	90.0	90.0

Table.2 Experimental results: accuracy rate changing frequency

Subject	s1	s2	s3	s4	s5	All
Accuracy rate	97.5	82.5	90.0	92.5	90.0	90.5

## Conclusion

By changing frequency, two currents interfere, and the beat frequency occurs. It was verified that the proposed method accomplished presentation of 4bit resolution information using electric stimulation without changing a voltage. We suggest that the method can use sensor feedback of direction of touch power.

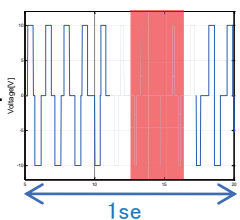


Fig.5 potential difference of two current

Table.3 Characterization of Sensory Nerve Fibers

Fiber Type	Function	Diameter [ $\mu$ m]	Frequency [Hz]
Unmyelinated Fiber (C Fiber)	Polymodal Nociceptors, Temperature, Slow Pain	0.4-1.5	5
Small Myelinated Fiber (A $\delta$ Fiber)	Mechanoreceptors, Pressure, Temperature, Fast Pain	1-5	250
Large Myelinated Fiber (A $\beta$ Fiber)	Touch, Pressure	5-15	2000

# Simulation of Human Walking with Orthosis for Keeping Balance of Upper Body



Yoshiho Uchiyama

uchiyama.yoshiho@b.mbox.nagoya-u.ac.jp

Goro Obinata

obinata@mech.nagoya-u.ac.jp

Chikara Nagai

nagai@coe.mech.nagoya-u.ac.jp

Nagoya University

Furo-cho, Chikusa-ku, Nagoya 464-8603, Japan

## Abstract

We have developed a powered assistive orthosis for paraplegic persons (Fig.1). Our purpose is to help rehabilitation for the person who has disturbance of motility and to substitute this orthosis for a wheelchair. This orthosis has 4 actuators which placed at knee joints and hip joints. These actuators are controlled by Central Pattern Generator (CPG). In aspect of rehabilitation we can get adequate assist to wearer. However this orthosis is limited to the motion on the sagittal plane, and not ensure stability of frontal plane. In order to design safer orthosis against three dimensional disturbances, we planned to implement new actuator at waist joint and simulated walking motion of human who wears the proposed orthosis. In the proposed orthosis, we can provide CPG-based power assist on the joint motion both on frontal and sagittal planes. By introducing one actuator at waist joint, we can control the motion balance on frontal plane.

The model dynamics of the coupled human-orthosis is represented by a 10-rigid-link system. In this model, we newly embedded rotational joint at waist, in addition to conventional joints at both thighs and both legs. These joints are controlled by CPG. The CPG controller consists of 13 oscillators which have the sensory feedbacks. The mutually entrainment of the rigid-link system and the controller has a potential of generating walking motions. The parameters of the oscillators and the connection in the network are optimized with a performance index by using a genetic algorithm. With the optimized controller we have achieved the successful simulation of steady gait (Fig.2).

Using this model we have searched how robust against disturbances in frontal plane. We added various external forces to this model and examined if the model could continue walking or fall down. As a result it continued walking at some cases. On the other hand falling down case can be divided two patterns, and if we prevent these we develop orthosis that prevent falling down. The simulation result can be used as a guideline for the new orthosis.

## Biography

Yoshiho Uchiyama is student of Department of Mechanical Engineering, Nagoya University. His research interests are biomechanics, human motion simulation, welfare engineering. This year, he will enroll at Graduate School of Engineering, Nagoya University.



Fig.1 Powered assistive orthosis

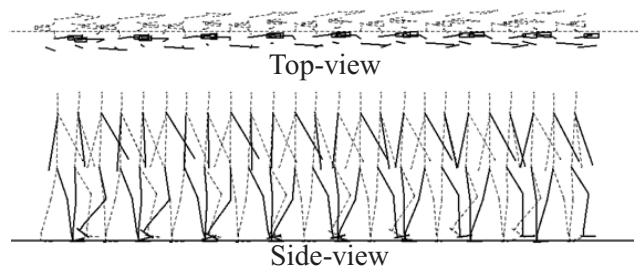


Fig.2 The model of steady gait.

# Simulation of Human Walking with Orthosis for Keeping Balance Upper Body

Yoshiho Uchiyama<sup>1</sup>, Goro Obinata<sup>2</sup>, Chikara Nagai<sup>3</sup>

<sup>1</sup>School of Engineering, Nagoya University <sup>2</sup>EcoTopia Sience Institute, Nagoya University

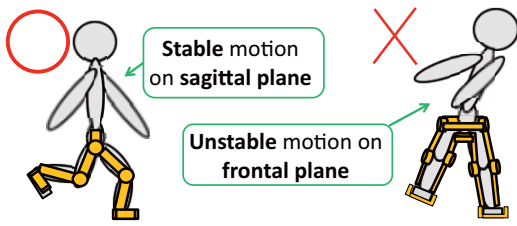
<sup>3</sup>Graduate School of Engineering, Nagoya University

## <Introduction>

The goal of this work is help **rehabilitation** for the person who has disturbance of motility and to **substitute** this orthosis for a **wheelchair**.

### Conventional orthosis

Conventional orthosis developed in our group has 4 actuators, which are placed at knee joints and hip joints and controlled by Central Pattern Generator (CPG). Therefore, the assist motion is limited on the sagittal plane.

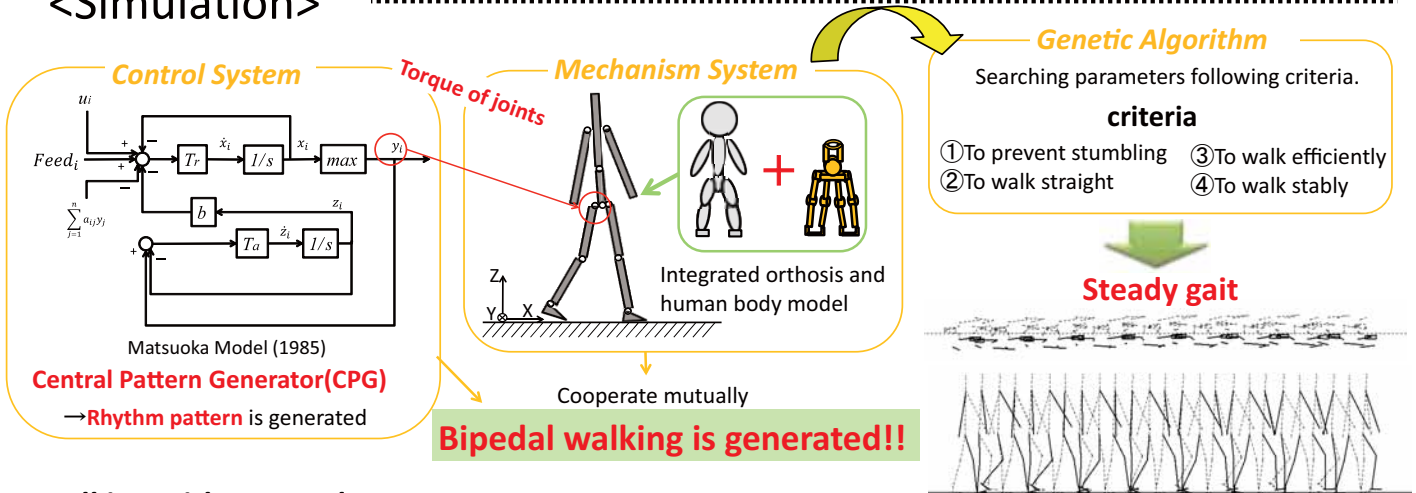


### Proposed system

**New actuator** planned to installed at waist joint.

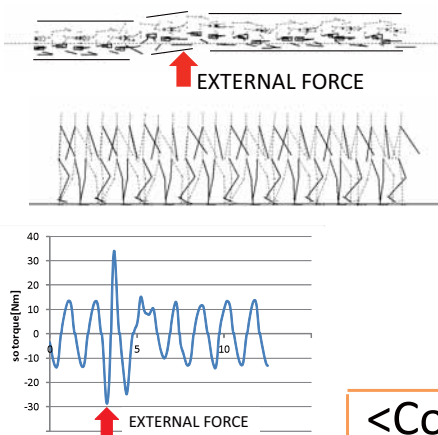
- 1 CPG-based power assist on the joint motion both on frontal and sagittal planes.
- 2 The motion balance on frontal plane can be controlled.

## <Simulation>



### Walking with External Force

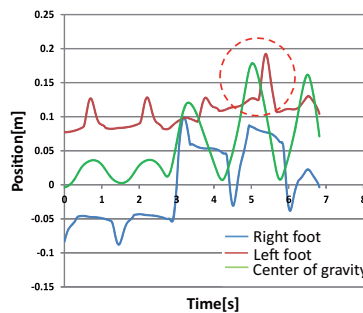
<continue to walk>



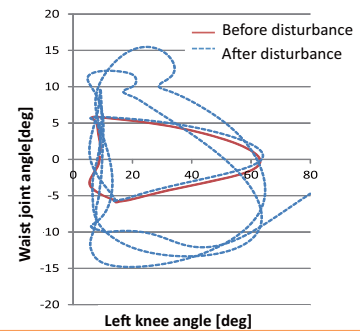
After disturbance the torque of waist joint become bigger to keep the upper body at center position.

<Falling Pattern>

Relationship between foot positions and center of gravity position



The transition of limit-cycle of each joint motion



## <Conclusions>

In order to design safer orthosis against three dimensional disturbances, a model that is composed of control system and mechanical system was developed. As a result we could have this model perform steady gait. Furthermore robust walking performance was obtained when we added external forces on the frontal plane. The simulation result can be used as a guideline for the new orthosis.

# Study of Operability on a Lever Steering System



Ryohei Sano

[sano.ryouhei@a.mbox.nagoya-u.ac.jp](mailto:sano.ryouhei@a.mbox.nagoya-u.ac.jp)

Goro Obinata

[obinata@mech.nagoya-u.ac.jp](mailto:obinata@mech.nagoya-u.ac.jp)

Chikara Nagai

[nagai@coe.mech.nagoya-u.ac.jp](mailto:nagai@coe.mech.nagoya-u.ac.jp)

School of Engineering, Nagoya University

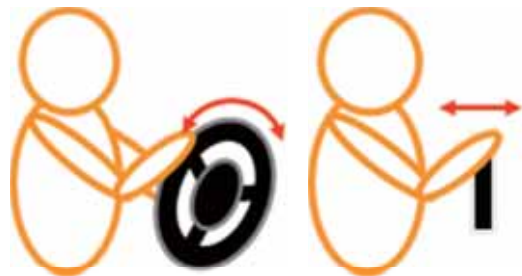
Furo-cho, Chikusa-ku, Nagoya 464-8603, JAPAN

## Abstract

We generally use circular movements with steering wheel in vehicle. (Fig. 1a) But today we can design various kinds of steering movements by using steer-by-wire system(The steer-by-wire system in vehicle substitutes the typical mechanical linkage with electric wires.). So other steering movements can potentially have better operability. Our purpose is to find more operable movements than circular movements.

To study operability of steering movements, we used a robot manipulator and a force sensor. An experimental setup is shown in Fig. 2. The robot manipulator is impedance-controlled. So it allows us to simulate various kinds of steering movements and amount of force to move. At the beginning of research, we simulated two steering movements; a forth-back steering movement (Fig.1 (b)) and a circular steering movement like a steering wheel. The both movements are operable with one hand. We compared their movements with reaching task. In the reaching task, an operator controls his hand position to target position as quickly as possible. Target and hand position (Mark) are shown in the display. Fig. 3 shows rise time with some viscosities. From the result of the task, forth-back movements have advantage in steering speed.

This result implies some steering movements are more operable than circular movement with steering wheel. But the results of this task are not enough. To find more operable steering movement, we have to consider other movements and aspects like a steering stability, fatigue of operators and so on.



(a)Circular movements (b) Forth-back movements

Fig. 1 Steering movements

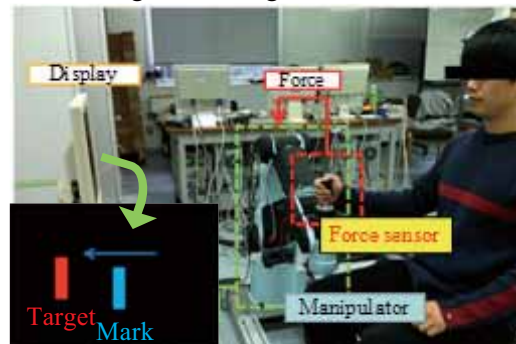


Fig. 2 Experimental setup

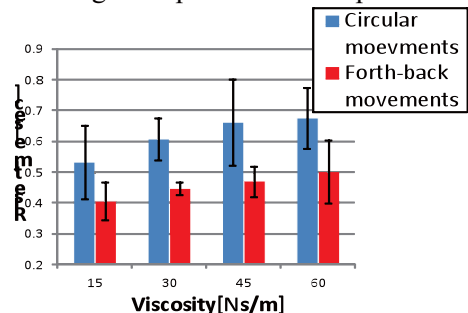


Fig. 3 Rise time from 10% to 90 % of the target position with two steering movement

## Biography

Ryohei Sano is a student in the Department of Mechanical Engineering, Nagoya University. He enters the Graduate School of Engineering, Nagoya University next year, and continues to study engineering for human.

# Study of Operability on a Lever Steering System

Ryohei Sano<sup>1</sup>, Goro Obinata<sup>2</sup>, Chikara Nagai<sup>3</sup>

<sup>1</sup>School of Engineering, Nagoya University

<sup>2</sup>EcoTopia Science Institute, Nagoya University

<sup>3</sup>Graduate School of Engineering, Nagoya University

## PURPOSE

The steer-by-wire (SBW) system in vehicle substitutes the typical mechanical linkage with electric wires. Using SBW technology, we can design various kinds of steering movement. And other steering movements can potentially have better operability. So we used a Robot manipulator and a force sensor to simulate various kinds of steering movements to study operability of steering movements.

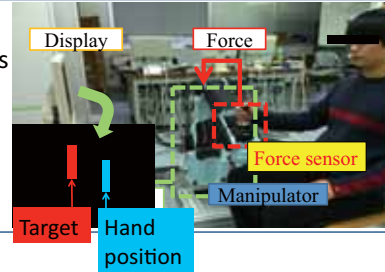
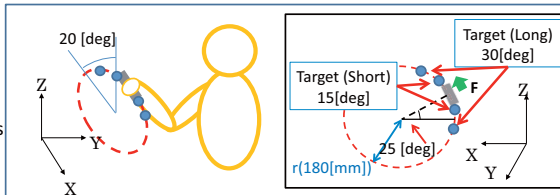


Fig. 1 Experiment setup

## EXPERIMENT

Fig. 2 Circular movements



Movements and target positions

$$I\ddot{\theta} + d\dot{\theta} = F \cdot r$$

$F$ : Force  
 $I$ : Inertia  
 $d$ : Viscosity  
 $r$ : Radius of the movement(180mm)

Both movements are operable with one hand. We compared them using reaching task. In the task, Subjects control their hand position to stop in the target position as quickly as possible. A part of the task is shown in Fig. 4.

4.

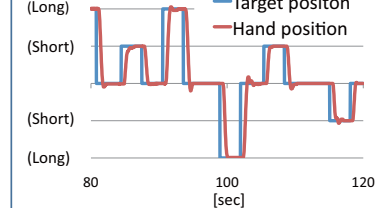
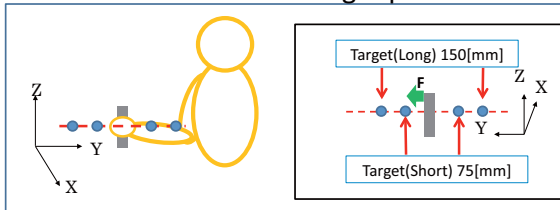


Fig. 4 Reaching task

Fig. 3 Forth-back movements



Movements and target positions

Manipulator control

$$m\ddot{y} + c\dot{y} = F$$

$F$ : Force  
 $m$ : Mass  
 $c$ : Viscosity

## RESULTS

### Difference between two movements

Fig. 5 shows settling time and rise time. Rising time is the time to move hand position from 10% to 90% of the target position. Settling time is the time to stop hand position from 10% to 95% of the target position in case target is long. (from 10% to 90% in case target is short.)

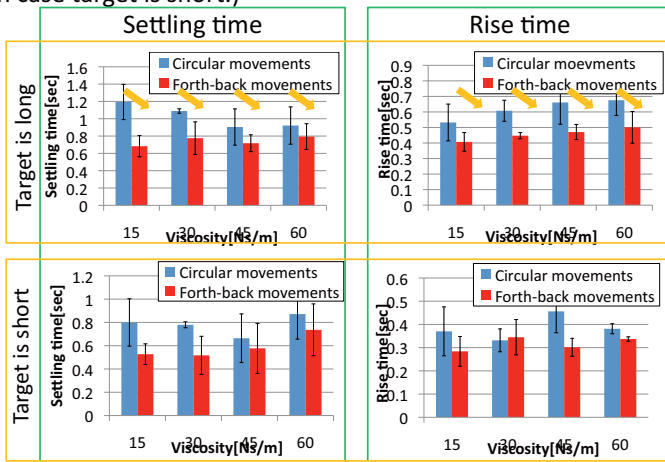


Fig. 5 Settling time and rise time in two movements

### Difference between target positions

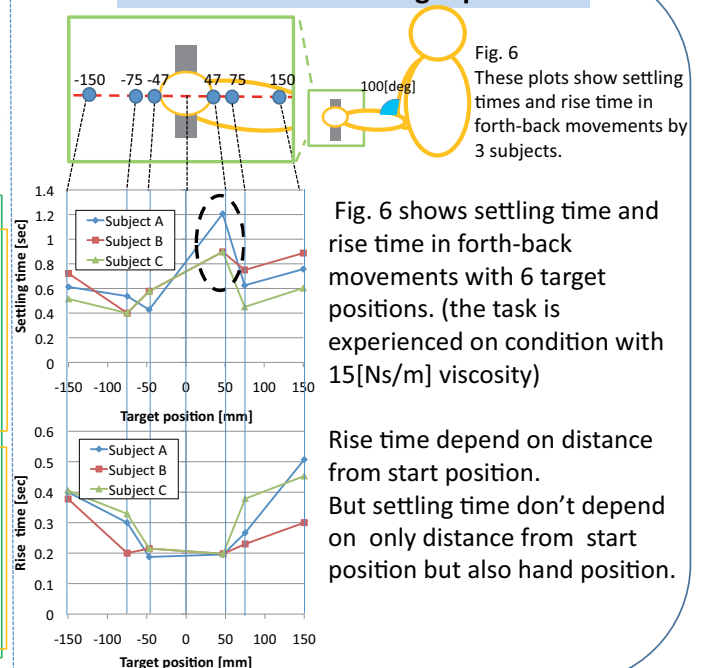


Fig. 6 These plots show settling times and rise time in forth-back movements by 3 subjects.

Fig. 6 shows settling time and rise time in forth-back movements with 6 target positions. (the task is experienced on condition with 15[Ns/m] viscosity)

Rise time depend on distance from start position. But settling time don't depend on only distance from start position but also hand position.

## CONCLUSION

In forth-back movements, human can control steering more speedy than that in circular movements. And control characteristics of forth-back movement is dependent on operator's posture heavily. If we can design steering movements appropriately, some steering movements are more operable than circular movement with steering wheel.

# Analysis on Hand Motions in Activity of Daily

## Living



Toshikatsu TANASE

[tanase.toshikatsu@h.mbox.nagoya-u.ac.jp](mailto:tanase.toshikatsu@h.mbox.nagoya-u.ac.jp)

Goro OBINATA

[obinata@mech.nagoya-u.ac.jp](mailto:obinata@mech.nagoya-u.ac.jp)

Chikara NAGAI

[nagai@coe.nagoya-u.ac.jp](mailto:nagai@coe.nagoya-u.ac.jp)

Nagoya University

Furo-cho, Chikusa-ku, Nagoya 464-8603, Japan

### Abstract

Most robot hands today are impractical in welfare field due to either too a large of actuators causing high energy consumption or a too small number of joints constraining the robot hand motions.

Our goal in this study is to reveal the needs of the hand motions in the daily life. Therefore we conduct experiment to reveal human hand mechanism which allows us to develop the prosthetic robot hand of simple mechanism with a few actuators achieving the versatile tasks of human hand.

In our experiment, we selected power grasping and pinching tasks (Fig.1) for motion analysis. We used 3D-motincapture system to measure hand joint angles of human who performs power grasping and pinching tasks. The hand motion can be realized by robot actuators whose number is same with the number of principal components of human hand motion.

The results of motion analysis show that human hand motion has 3 principal components (Fig.2). This means we can reduce the actuator number of the robot hand for realizing power grasping and pinching tasks. The results obtained in this study can be used as a guideline to develop a simple-structured robot hand.



Fig.1 Pinching and power grasping

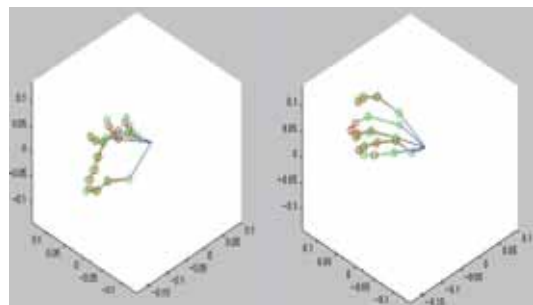


Fig.2 Reconstruction of pinching and power grasping

### Biography

Toshikatsu Tanase is student of Department of Mechanical Science & Engineering, School of Engineering, Nagoya University. This year, he will graduate there and enroll at Graduate School of Engineering, Nagoya University.

# Analysis on Hand Motions in Activity of Daily Living

Toshikatsu TANASE<sup>1</sup>, Goro OBINATA<sup>2</sup>, Chikara NAGAI<sup>3</sup>

<sup>1</sup>Department of Engineering, Nagoya University <sup>2</sup>Graduate School of Engineering, Nagoya University

<sup>3</sup>Eco Topia Science Institute, Nagoya University

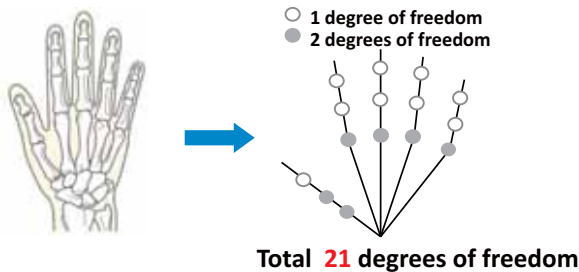
## Previous Research & Goal

Most robot hands today are impractical in welfare area due to either too many actuators causing too much energy consumption or due to a too small number of joints constraining the robot hand motions.

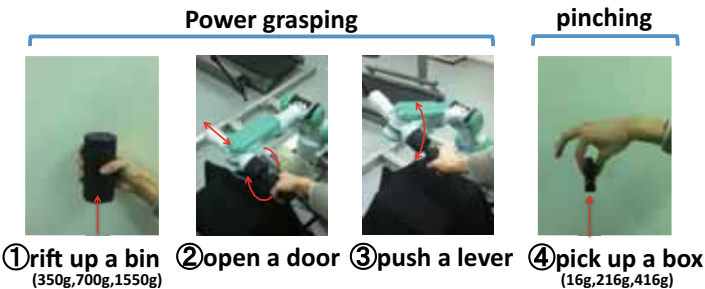
Our goal is to reveal human hand mechanism which allows us to develop the prosthetic robot hand of simple mechanism with a few actuators achieving the versatile tasks of human hand. And we want to find out enough number of actuators to express the versatile hand motions in daily living.

## Experiment Approach

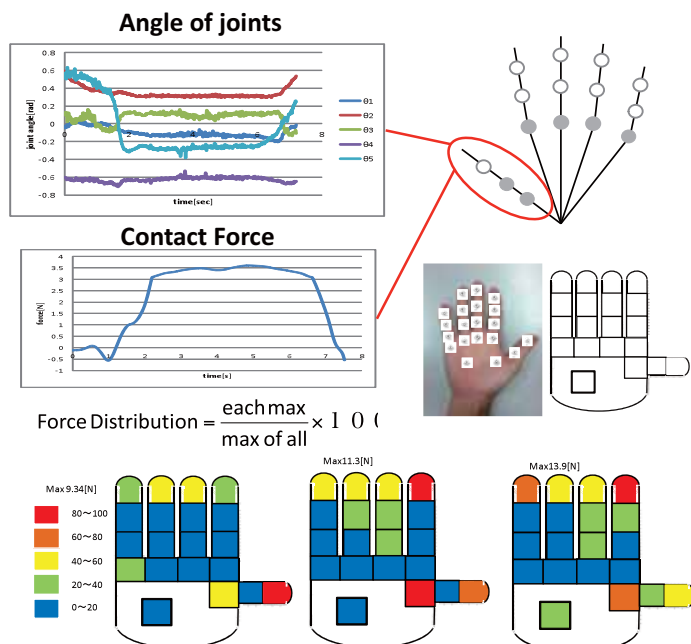
### 1. Assumption of Skelton Model of The Hand



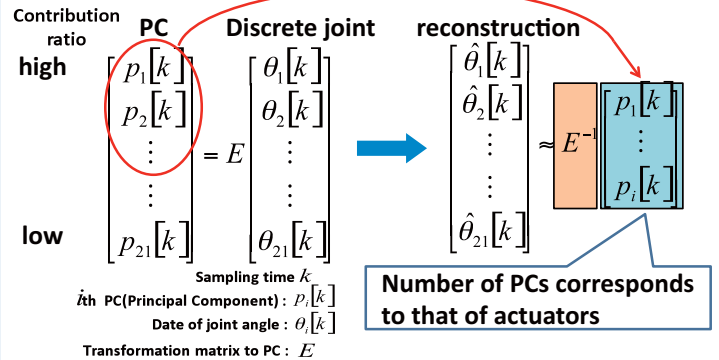
### 2. Selection of The hand motions



### 3. Measuring angle of joints & Contact Force



## 4. Principal Component Analysis(PCA)



## Results

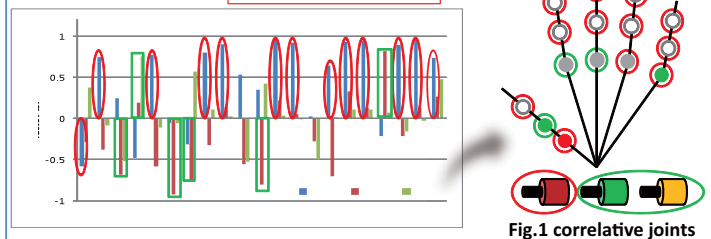
### PCA results of Multiple motions

Motion	①all	①700g②③	①all②③	①700g②③④216g	①all②③④all
1th PC	84.6%	69%	66.8%	76.6%	64.3%
2th PC	6.61%	22.7%	22.2%	13.4%	20.8%
3th PC	3.33%	2.85%	5.03%	2.8%	5.94%
4th PC	1.69%	1.39%	1.65%	1.62%	2.15%
5th PC	1.04%	0.934%	1.01%	1.45%	1.70%

■ : Total cumulative contribution ratio over 90%

We estimated the number of PCs enough to express all of these motions by analyzing these signals by PCA. As a result, we found out that these motions can be expressed by 3 PCs, since total cumulative contribution ratio is over 90% by 3 PCs.

### Factor Loading of PC of [①all②③④all]

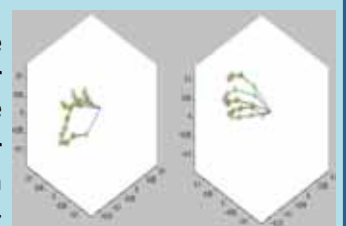


Focus on factor loading of PC, and we find out what joints are correlative with 1th~3th PC. We showed that correlative joints with 1th PC and 2,3th PC are red and green (Fig.1). As a result, we found out that most of the required joints to express these hand motions can be moved by 1th~3th PC.

## Conclusion

We found out that most of the required joints to express these hand motions can be moved by 1th~3th PC and to be able to reconstruct these motions by 1th~3th PC sufficiently (Fig.2).

We concluded that these hand motions such as power grasping and pinching can be made with 3 actuators. Our result can be used as a guideline to develop a simple-structured robot hand.





## **<4> Appendix**

**a) Travel Schedule**

**b) Pictures**

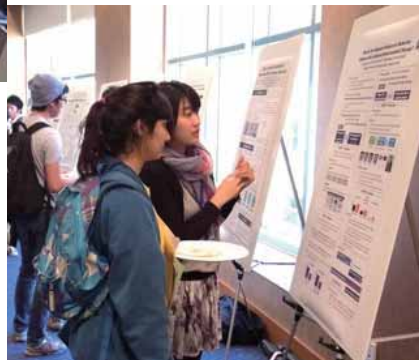
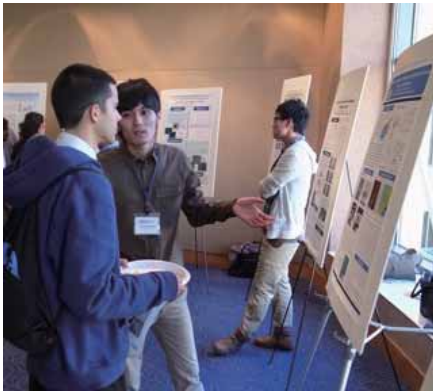
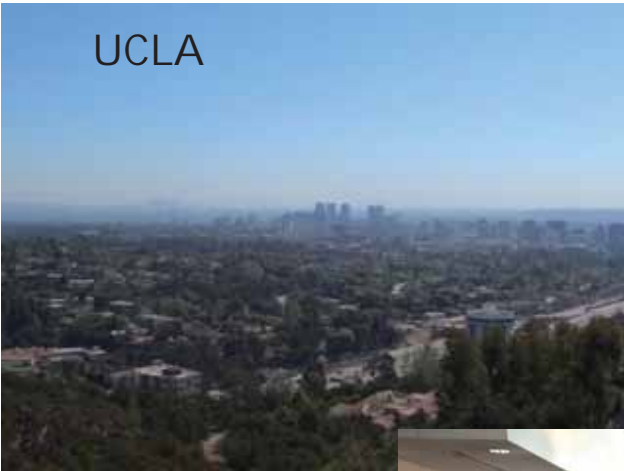


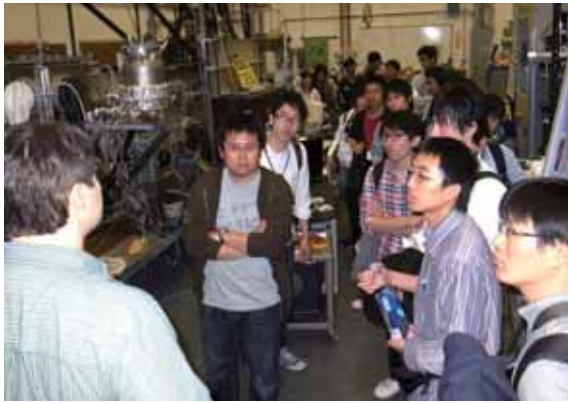
# Travel Schedule

March 7 - 17, 2012

月日	都市名	現地時間	行程
3月7日 (水)	名古屋大学豊田講堂 中部国際空港 成田空港 成田空港 ロサンゼルス空港	6:00 8:25 9:35 15:30 8:45	大型バスにて中部国際空港へ 空路日本航空にて成田空港へ  空路デルタ航空にてロサンゼルス空港へ 専用車にてホテルへ
3月8日 (木)	ホテル UCLA  ホテル	9:30 11:00-15:00 15:30-	Poster presentations Lunch party
3月9日 (金)	ホテル UCLA ホテル	10:00 13:00-16:00	Lab tours
3月10日 (土)	ホテル UCLA ホテル	9:30-	Lab tours
3月11日 (日)	ホテル ロサンゼルス空港 デトロイト空港 ホテル	11:35 19:00	専用車にて空港へ 空路デトロイト国際空港へ 専用車にてホテルへ
3月12日 (月)	ホテル Univ. Michigan  ホテル	9:00- -17:30 18:00-20:00	Poster presentations Lab tours Banquet
3月13日 (火)	ホテル Univ. Michigan Toyota Tech Center ホテル	9:00-14:00 15:00-17:00	Lab tours Technical tours
3月14日 (水)			
3月15日 (木)			
3月16日 (金)	ホテル デトロイト空港	12:00 15:30	専用車にて空港へ 空路中部国際空港へ
3月17日 (土)	中部国際空港 名古屋大学豊田講堂	19:05 21:00頃	到着.入国手続き 大型バスにて名古屋大学へ 豊田講堂前到着後解散

UCLA





# University of Michigan

